

103

Comparison and Validation  
of Two Shallow Water  
Spectral Wave Models

The Environmental Studies Research Funds are financed from special levies on the oil and gas industry and administered by the Canada Oil and Gas Lands Administration for the Minister of Energy, Mines and Resources, and by the Northern Affairs Program for the Minister of Indian Affairs and Northern Development.

The Environmental Studies Research Funds and any person acting on their behalf assume no liability arising from the use of the information contained in this document. The opinions expressed are those of the authors and do not necessarily reflect those of the Environmental Studies Research Funds agencies. The use of trade names or identification of specific products does not constitute an endorsement or recommendation for use.

**Environmental Studies Research Funds**

**Report No. 103**

**June 1989**

**Comparison and Validation of Two  
Shallow Water Spectral Wave Models**

**Donald O. Hodgins  
Chris T. Niwinski  
Donald T. Resio**

**Seaconsult Marine Research Ltd.  
820 - 1200 West 73rd Avenue  
Vancouver, Canada**

**Scientific Advisor: Volker Barthel**

The correct citation for this report is:

Hodgins, D.O., C.T. Niwinski and D.T. Resio. 1989. Comparison and validation of two shallow water spectral wave models. Environmental Studies Research Funds Report No. 103. Ottawa. 143 p. plus 6 appendices.

Published under the auspices of the  
Environmental Studies Research Funds.  
ISBN 0-921652-06-2  
©Seaconsult Marine Research Ltd.

TABLE OF CONTENTS

	<u>Page</u>
List of Tables	iv
List of Figures	v
Acknowledgements	x
Summary	xi
Résumé	xv
<b>1.0 INTRODUCTION</b>	<b>1</b>
1.1 Shallow Water Wave Calculations	1
1.2 Spectral Wave Models	3
1.3 WAVAD: A Coupled Discrete Spectral Model	15
1.4 SPECREF: A Decoupled Propagation Model	19
<b>2.0 SHALLOW WATER WAVE DATA</b>	<b>23</b>
2.1 The 1984-85 Field Program	23
(a) Instrumentation	28
(b) Data Processing	33
2.2 Basic Results	36
<b>3.0 WAVE PREDICTION INTERCOMPARISON</b>	<b>49</b>
3.1 Methods	49
3.2 Storm Selection	55
3.3 Idealized Test Cases	58
3.4 Application to Sable Island Bank	60
<b>4.0 INTERCOMPARISON RESULTS</b>	<b>65</b>
4.1 Prediction of Characteristic Wave Parameters	67
4.2 Prediction of Spectral Shape	88
4.3 Sensitivity to Wind Input and Bottom Friction	95
4.4 Sensitivity to Bathymetric Resolution	101
4.5 Idealized Test Case Results	105
<b>5.0 CONCLUSIONS AND RECOMMENDATIONS</b>	<b>133</b>
5.1 Spectral Model Performance	133
(a) Expected Accuracies	133
(b) Strengths and Weaknesses of WAVAD and SPECREF	135
5.2 Areas of Model Improvement	136
5.3 Implications for Oil and Gas Developments	137
5.4 Recommendations	138
<b>References</b>	<b>141</b>
<b>Appendices (microfiche)</b>	

**LIST OF TABLES**

	<u>Page</u>
Table 2.1 Instrument Disposition and Data Recovery 1984-85 Field Program	25
Table 2.2 Directional Wave Data Instrument and Sampling Specification	32
Table 3.1 Idealized Test Case Parameters	59
Table 3.2 Summary of WAVAD Parameters	61
Table 3.3 Summary of SPECREF Parameters	64
Table 4.1 Wave Model Statistical Analysis Results	85
Table 4.2 Comparison of Measured and Predicted $H_s$ for Various Wind and Bottom Friction Conditions	99
Table 4.3 Comparison of Significant Wave Heights for the Idealized Test Cases	107

LIST OF FIGURES

	<u>Page</u>
Fig. 1.1a Computed and observed spectra using parallel bottom topography (top) and irregular bottom topography (bottom) from Collins (1972).	5
Fig. 1.1b Comparison of computed and measured deep-water spectra. Upper panel: data from 76-05-05-16:15. Lower panel: data from 76-05-11-10:15. (Source: Wang and Yang, 1981).	6
Fig. 1.2 Schematic diagram of the wind-wave energy spectrum during active growth and the wave-wave interaction source/sink function. (Source: Resio, 1982).	8
Fig. 1.3 Computed and measured wave transformation at the Marineland site. The spectrum at 10 m depth is computed from the measured spectrum at 29 m depth as initial value. The source and sink scale refers to the total contribution from 29 to 10 m depth. (Source: Shemdin et al., 1977).	12
Fig. 1.4 Wave transformation in finite depth water: the solid curve is the measured spectrum, the dashed curve denotes the measured spectrum inshore and the dot-dashed curve is the computed spectrum inshore using the solid curve as input. The energy changes computed in the lower panel include frictional dissipation (--), refraction and shoaling (-.-), nonlinear wave transfer (-..-), all adding up to the solid curve. (Source: Shemdin et al., 1980).	13
Fig. 2.1 Disposition of wave and wind instrumentation providing data for the wave model intercomparison.	24
Fig. 2.2 Oblique photograph of the southern flank of Sable Island as viewed from the east, looking west.	26
Fig. 2.3 Aerial photograph of East Spit and the shallow bar extension that produces a linear zone of breaking waves extending approximately 10 km northeast of the island.	27
Fig. 2.4 Detailed bathymetry in the region of shallow water wave measurements.	29

**LIST OF FIGURES**  
**(Continued)**

	<u>Page</u>
Fig. 2.5 Representative grain size distribution for fine sands on the southeast flank of Sable Island in 30 m depth. (Source: Hodgins et al., 1986)	30
Fig. 2.6 Schematic diagram of the Wavec buoy (a) and a photograph of the buoy during deployment (b).	31
Fig. 2.7a Time-series of wind speed, wind and wave directions (given as direction towards which winds are blowing and waves are propagating), significant wave height and peak period for the 1984-85 directional wave measurement program at station 252.	37
Fig. 2.7b Time-series of wind speed, wind and wave directions (given as direction towards which winds are blowing and waves are propagating), significant wave height and peak period for the 1984-85 directional wave measurement program at station 253.	38
Fig. 2.8 Time-series of significant wave height measured at stations 133 and 251 in conjunction with the 1984-85 field program. A portion of the station 252 record in the December 26-28 storm is shown for comparison of deep and shallow water wave conditions.	39
Fig. 2.9a Directional wave spectra from station 252 (22 m water depth) in 20 frequency bands plotted against the Sable Island measured wind and significant wave height, December 23-28, 1984.	41
Fig. 2.9b Directional wave spectra from station 253 (12 m water depth) in 20 frequency bands plotted against the Sable Island measured wind and significant wave height, December 23-28, 1984.	42
Fig. 2.9c Directional wave spectra from station 253 (12 m water depth) in 20 frequency bands plotted against the Sable Island measured wind and significant wave height, January 2-7, 1985.	43
Fig. 2.9d Directional wave spectra from station 253 (12 m water depth) in 20 frequency bands plotted against the Sable Island measured wind and significant wave height, January 13-18, 1985.	44



**LIST OF FIGURES**  
**(Continued)**

	<u>Page</u>
Fig. 2.9e Directional wave spectra from station 253 (12 m water depth) in 20 frequency bands plotted against the Sable Island measured wind and significant wave height, January 20-25, 1985.	45
Fig. 2.10 Sample spectra from sites 252 and 253 at 84-12-26-21Z and 84-12-27-00Z.	47
Fig. 3.1 Shallow water modelling domain on Sable Island Bank.	50
Fig. 3.2 Deep water wave modelling grids used with WAVAD.	51
Fig. 3.3a Wind field and deep water coarse grid wave height and direction fields at 06 GMT on December 26, 1984 calculated with WAVAD.	52
Fig. 3.3b Typical solution for wave height and direction on the intermediate grid (shown here for 06 GMT on December 26, 1984).	53
Fig. 3.4 Location of the four storm events in the wave theory graph. The SWIM point is based on data from Bouws et al. (1985).	57
Fig. 3.5 Contoured bathymetry as resolved on the one n.m. grid used in SPECREF.	62
Fig. 4.1 Comparison of predicted and measured wave properties in storm 1 (station 165).	68
Fig. 4.2 Comparison of predicted and measured wave properties in storm 1 (station 170).	69
Fig. 4.3 Comparison of predicted and measured wave properties in storm 1 (station 167).	71
Fig. 4.4 Comparison of predicted and measured wave properties in storm 2 (station 133).	72
Fig. 4.5 Comparison of predicted and measured wave properties in storm 2 (station 252).	74
Fig. 4.6 Comparison of predicted and measured wave properties in storm 2 (station 253).	75

**LIST OF FIGURES**  
**(Continued)**

	<u>Page</u>
Fig. 4.7 Comparison of predicted and measured wave properties in storm 3 (station 133).	76
Fig. 4.8 Comparison of predicted and measured wave properties in storm 3 (station 253).	78
Fig. 4.9 Comparison of predicted and measured wave properties in storm 4 (station 133).	79
Fig. 4.10 Comparison of predicted and measured wave properties in storm 4 (station 253).	80
Fig. 4.11 Regressions of $H_S$ -predicted onto $H_S$ -measured for deep ( $h > 25$ m) and shallow ( $h < 25$ m) water on Sable Island Bank for the four hindcast storms.	82
Fig. 4.12 Frequency histograms for $E_{Tp}$ .	83
Fig. 4.13 Frequency histograms for $E_\theta$ .	84
Fig. 4.14 Comparison of measured and predicted spectra in storm 2 (Station 252). The arrowhead indicates wind direction.	89
Fig. 4.15 Comparison of measured and predicted spectra in storm 2 (Station 253). The arrowhead indicates wind direction.	90
Fig. 4.16 Comparison of measured and predicted spectra in storm 3 (Station 253). The arrowhead indicates wind direction.	92
Fig. 4.17 Comparison of measured and predicted spectra in storm 4 (Station 253). The arrowhead indicates wind direction.	93
Fig. 4.18a Comparison of predicted and measured wave parameters with wind input (right) and without wind input (left) at station 133.	96
Fig. 4.18b Comparison of predicted and measured wave parameters with wind input (right) and without wind input (left) at station 252.	97

**LIST OF FIGURES**  
**(Continued)**

	<u>Page</u>
Fig. 4.18c Comparison of predicted and measured wave parameters with wind input (right) and without wind input (left) at station 253.	98
Fig. 4.19 Comparison of WAVAD results for storm 2 modelled on the 1 n.m. and the 5 n.m. grids.	102
Fig. 4.20 Comparison of 1-dimensional spectra from WAVAD modelled on the 1 n.m. and the 5 n.m. grid.	103
Fig. 4.21 Comparison of spectra at different water depths for idealized test A1.	106
Fig. 4.22 Spectra computed by SPECREF for various water depths with and without wind (A1 versus A2).	108
Fig. 4.23 Spectra computed by WAVAD for various water depths with and without wind (A1 versus A2).	116
Fig. 4.24 Spectra computed by SPECREF for various water depths with and without wind (B1 versus B2).	123
Fig. 4.25 Spectra computed by WAVAD for various water depths with and without wind (B1 versus B2).	127

**ACKNOWLEDGEMENTS**

The following organizations and personnel have contributed to this study.

Seaconsult Marine Research Ltd.

Donald O. Hodgins, Ph.D., P.Eng. (Project Manager)

Christopher T. Niwinski, M.A.Sc., P.Eng.

Donald S. Dunbar, Ph.D.

Offshore and Coastal Technologies Inc.

Donald T. Resio, Ph.D.

We also wish to acknowledge the cooperation and assistance provided by the Canadian Coast Guard who provided access to their facilities on Sable Island that were essential to the wave measurement program, and the support provide by McElhanney Services Ltd. of Dartmouth, and in particular Mr. Tom Windeyer of that group, for deployment and recovery of the wave buoys during December and January in particularly inclement weather. We also wish to acknowledge the equipment and personnel provided by the Marine Environmental Data Service as part of the wave measurement program, and the support of ESRF during this project.

## SUMMARY

Design wave criteria are required in several offshore areas that feature water depths sufficiently shallow to modify wave conditions incident onto them from deep water. These areas include, for example, Sable Island Bank, the Beaufort Sea and parts of Queen Charlotte Strait in British Columbia. Shallow water wave criteria are frequently derived using spectral hindcast models which vary considerably in their treatment of the complex physical processes that govern wave transformation. The purpose of this study was to compare the performance of two shallow water models with a view to determining their suitability for application in Canadian waters.

The two models were (1) a first-generation model named SPECREF developed and tested by Seaconsult Marine Research Ltd., and (2) a second-generation model developed by Offshore and Coastal Technologies Inc. called WAVAD. The two models are similar in terms of the procedures for evaluating refraction and shoaling, and in the fact that each uses a saturation spectrum to limit energies at frequencies above  $f_p$ , although the form of the saturation spectrum differs in each code. However, the models are fundamentally different in the specification of the wind source term and the partitioning of energy between the dissipation region above  $f_p$  and to lower frequencies below  $f_p$ . SPECREF treats the change in energy at each frequency, produced by refraction, shoaling, wind input and bottom friction, independently of all other frequencies without explicitly evaluating energy fluxes produced by the nonlinear wave-wave interaction process. WAVAD, on the other hand, evaluates the energy balance in a manner consistent with theory based on energy transfers resulting from wave-wave interactions. The nonlinear interaction source term  $S_{n1}$  is not evaluated explicitly; rather, the energy fluxes are estimated in a parametric form and the spectrum is modified accordingly. For this reason, the models may be expected to perform differently under various incident wave conditions over complex bathymetry.

In order to assess the model performance new directional wave data were collected on Sable Island Bank in 22 m and 12 m of water to the south of

Sable Island, concurrently with non-directional deep water measurements. The directional data were collected with WAVEC heave-pitch-roll buoys and processed using conventional procedures to yield estimates of significant wave height, peak period, peak direction, the energy spectrum, and the wave direction and spreading exponent as functions of frequency. The data collection period spanned 36 days in December 1984-January 1985, yielding data for four winter storms with winds and waves incident from the south and southwest onto the south side of Sable Island.

The models were used to hindcast three of the four directional storms, and a fourth storm monitored for non-directional wave data incident from the east onto the eastern flank of Sable Island Bank. Two idealized tests for wind-sea and swell incident onto the bank from the south, with and without a westerly wind, were also compared. Model performance was gauged by the accuracy of prediction of wave height, period and direction in shallow water, and by a qualitative assessment of predicted directional spectral properties.

It was found that both models capture the essential shallow water features in measured spectra, including energy losses as waves propagate into shore, and the changes in direction produced by refraction. In statistical terms SPECREF exhibited an R.M.S. wave height error of 1.1 m compared with 1.2 m for WAVAD, with respective scatter indices of 17% and 18%. SPECREF was unbiased for period whereas WAVAD tended to be biased low by 0.016 Hz. Errors in wave direction ranged from 5° to 10°. These error statistics, while based on a limited data set, are similar to statistics published for other deep water spectral wave models (GSOWM), indicating that there is not a significant loss of accuracy for shallow water calculations over complex bathymetry.

The spectral comparisons showed that both models provide reasonable agreement with the measured spectra, although there is considerable variability and each model has some undesirable characteristics. The decoupled formulation of SPECREF leads to nearly-discontinuous

directional shifts between energy at frequencies near  $f_p$  and at higher frequencies for the 0.010 Hz resolution used in this study, and the spread of energy appears too narrow. WAVAD models the directional distribution of energy in better agreement with measurements; however, the tendency to underpredict  $T_p$  leads to a systematic departure of modelled energy from measured energy distributions on the forward face of the spectrum.

The idealized tests revealed further differences between the models, particularly with respect to the sensitivity of each to wind wave growth and the energy balance for incident conditions normal to nearly-parallel bottom contours. For winds at large angle to the dominant wave direction, SPECREF predicts stronger growth than WAVAD in both wind-sea and swell conditions. SPECREF exhibits down-wind wave growth in deep water, as expected, and shows intuitively reasonable directional shifts in shallow water where refraction plays an important role. WAVAD exhibits much less down-wind wave growth, with energies distributed over all frequencies greater than  $f_p$  and more closely aligned with the dominant wave direction of the incident spectrum. WAVAD also exhibits greater dissipation of energy, compared with SPECREF, as waves characteristic of well developed storm seas propagate into shallow water. On the other hand, for characteristic swell spectra SPECREF predicted slightly greater dissipation. On the basis of the hindcast results for one of the monitored storms (storm 4), SPECREF appears to be more realistic in these situations.

One of the principal conclusions of this study is that either model tested here is suitable for shallow water hindcasting, noting however, that differences in model formulations lead to variations in model performance. Consequently, use of the models for hindcasting design wave data will require careful validation with measurements made in the area of interest. It is also apparent that further development of modelling techniques is warranted. The objective of such development

would be to reduce prediction errors in certain wind and wave conditions, and to confirm the parameterization of the physics contained in each model.



## RÉSUMÉ

Les critères de la vague nominale sont nécessaires dans plusieurs régions au large où l'eau est assez peu profonde pour que soient modifiées les vagues incidentes en provenance de zones aux eaux plus profondes. Mentionnons par exemple, le banc de l'île de Sable, la mer de Beaufort et des parties du détroit de la Reine-Charlotte en Colombie-Britannique. Les critères des vagues en eau peu profonde sont fréquemment dérivés à l'aide de modèles spectraux de prévisions à posteriori traitant de manière très variable les processus physiques complexes régissant la transformation des vagues. L'objet de la présente étude était la comparaison du rendement de deux modèles applicables aux eaux peu profondes dans le but de déterminer leur applicabilité aux eaux canadiennes.

Les deux modèles en cause étaient 1) le SPECREF, un modèle de première génération mis au point et éprouvé par la Seaconsult Marine Research Ltd. et 2) le WAVAD, un modèle de deuxième génération mis au point par l'Offshore and Coastal Technologies Inc. Les deux modèles sont similaires quant aux procédures d'évaluation de la réfraction et des effets de la diminution de la profondeur, ainsi que par le fait que chacun fait intervenir un spectre de saturation pour limiter les énergies et les fréquences au-delà de  $f_p$ , bien que la forme de ce spectre de saturation diffère dans chacun des programmes. Les deux modèles diffèrent toutefois fondamentalement par la spécification du terme pour la source du vent et par le partage de l'énergie entre la région de dissipation au-delà de  $f_p$  et les fréquences moindres en deçà de  $f_p$ . Le SPECREF traite pour chaque fréquence la variation de l'énergie produite par la réfraction, la diminution de la profondeur, les données d'entrée sur le vent et le frottement sur le fond, indépendamment de toutes les autres fréquences sans évaluer explicitement les flux d'énergie engendrés par le processus non linéaire de l'interaction vagues-vagues. D'autre part, le WAVAD évalue l'équilibre énergétique de manière conforme à la théorie, d'après les transferts d'énergie résultant des interactions vagues-vagues. Le terme source pour l'interaction non linéaire,  $S_{nl}$ , n'est pas évalué explicitement; les flux d'énergie sont plutôt estimés sous forme paramétrique et le spectre est modifié en conséquence. L'on peut, pour cette raison, s'attendre à ce que les modèles donnent différents résultats dans différentes conditions de vagues incidentes lorsque la bathymétrie est complexe.

Afin d'évaluer le rendement des modèles, de nouvelles données sur la direction des vagues ont été recueillies sur le banc de l'île de Sable par des profondeurs de 22 m et de 12 m au sud de l'île de Sable simultanément à des mesures non directionnelles en eau profonde. Les données directionnelles ont été recueillies à l'aide de bouées WAVEC de mesure du soulèvement-tangage-roulis et traitées au moyen des procédures classiques afin d'obtenir des estimations de la hauteur significative des vagues, de la période de pointe, de la direction de pointe, du spectre d'énergie et de la direction des vagues ainsi que de l'exposant de l'étalement sous formes de fonctions de la fréquence. Les données recueillies couvrent un intervalle de 36 jours en décembre 1984 et en janvier 1985 pendant lequel il y a eu quatre tempêtes hivernales avec des vents et des vagues incidentes du sud et du sud-ouest sur le côté sud de l'île de Sable.

Les modèles ont été utilisés pour la prévision à posteriori de trois des tempêtes directionnelles et une quatrième tempête a été surveillée en vue de l'obtention de données non directionnelles sur les vagues incidentes de l'est sur le flanc est du banc de l'île de Sable. Deux essais idéalisés pour une mer et une houle du vent incidentes sur le banc depuis le sud avec et sans vent de l'ouest ont également été comparés. Le rendement des modèles a été évalué par la précision de la prévision de la hauteur, de la période et de la direction des vagues en eau peu profonde ainsi que par une évaluation qualitative des propriétés directionnelles spectrales prévues.

Il a été constaté que les deux modèles reconstituent les entités essentielles des spectres mesurés en eau peu profonde dont les pertes d'énergie attribuables à la propagation des vagues en direction du rivage et les changements de direction produits par la réfraction. En termes statistiques le SPECREF fournissait une erreur-type de 1,1 m sur la hauteur des vagues comparativement à une erreur type de 1,2 m pour le WAVAD, les indices de dispersion respectifs étant de 17 % et de 18 %. Le SPECREF ne présentait aucune erreur sur la période alors que le WAVAD sous-estimait la période par 0,016 Hz. Les erreurs sur la direction des vagues variaient de 5 à 10 degrés. Ces statistiques sur les erreurs, bien que basées sur un ensemble restreint de données se comparent à des statistiques publiées pour d'autres modèles spectraux des vagues en eau profonde (GSOWM), ce qui indique qu'il n'y a pas perte significative de précision lors de calculs dans des eaux peu profondes lorsque la bathymétrie est complexe.

Les comparaisons spectrales indiquent que les résultats fournis par les deux modèles concordent raisonnablement bien avec les spectres mesurés, bien que la variabilité soit considérable et que chacun des modèles présente des caractéristiques indésirables. La formulation découplée du SPECREF mène à des écarts directionnels presque discontinus entre les énergies à des fréquences voisines de  $f_p$  et à des fréquences plus élevées avec la résolution de 0,010 Hz utilisée dans le cadre de la présente étude et la plage pour l'énergie semble trop étroite. Le WAVAD permet une modélisation de la distribution de l'énergie plus conforme aux mesures; toutefois, la tendance à sous-estimer  $T_p$  entraîne un écart systématique entre les distributions de l'énergie obtenue du modèle et mesurée pour la face avant du spectre.

Les essais idéalisés ont révélé d'autres différences entre les modèles, en particulier au niveau de la sensibilité de chacun quant à la croissance des vagues de vent et à l'équilibre énergétique dans des conditions de vagues incidentes normales à des courbes bathymétriques presque parallèles. Pour les vents soufflant à un angle important par rapport à la direction dominante des vagues, le SPECREF prévoit une croissance des vagues plus importante que le WAVAD dans des conditions de mer et de houle du vent. Le SPECREF indique, comme on peut s'y attendre, une croissance des vagues sous le vent en eau profonde et des écarts directionnels intuitivement raisonnables en eau peu profonde où la réfraction joue un rôle important. Le WAVAD indique une croissance des vagues sous le vent de beaucoup inférieure ainsi que des énergies distribuées sur toutes les fréquences supérieures à  $f_p$  et plus étroitement alignées avec la direction dominante des vagues du spectre incident. Le WAVAD indique également une dissipation de l'énergie plus importante que celle indiquée par le SPECREF, lorsque les vagues

caractérisant des mers de tempête bien formées se propagent en eau peu profonde. D'autre part, pour le spectre caractéristique de la houle, le SPECREF prévoit une dissipation légèrement supérieure. D'après les résultats de la prévision à postériori pour l'une des tempêtes surveillées (la tempête 4), le SPECREF semble fournir des résultats plus réalistes dans ces situations.

L'une des principales conclusions de la présente étude est que ni l'un ni l'autre des modèles éprouvés convient pour la prévision à postériori en eau peu profonde; il faut toutefois signaler que différentes formulations des modèles entraînent des variations de leur rendement. En conséquence, l'utilisation de ces modèles pour la prévision à postériori de données sur les vagues nominales exigera des travaux soignés de validation et des mesures effectuées dans la zone d'intérêt. Il appert également que des travaux plus poussés de mise au point des méthodes de modélisation sont justifiés. Les objectifs de tels travaux devraient être la réduction des erreurs de prévision dans certaines conditions de vent et de vagues ainsi que la confirmation du paramétrage des phénomènes physiques dans chacun des modèles.

## 1.0 INTRODUCTION

### 1.1 Shallow-Water Wave Calculations

The problem addressed in this study is the calculation of wave conditions in shallow water. By waves we refer to surface gravity waves generated by wind; this includes wind-sea and swell with periods between 2 and 40 s. Many of the methods discussed in this report are applicable also to "long waves", particularly tsunamis, but such waves are not of interest here. A number of depth-dependent transformation processes are central to the problem. These include refraction and shoaling, wave breaking, and dissipation through surface wave interaction with the sea bed. Diffraction may also be present. Two other processes, common to deep water wave computations, must in general be considered: energy input from the local overwater wind, and nonlinear energy fluxes between waves at different frequencies (wave-wave interactions).

Modelling of shallow water wave conditions has followed two general approaches. The first is concerned with conditions where diffraction is expected to play an important role, and the distance travelled by individual waves is short enough that wave growth due to wind may be ignored. Boundary conditions are usually formulated in terms of a single wave frequency and solutions are sought for the spatial distribution of wave amplitude and phase. These models, which may be classed as "individual wave" models are deterministic in nature, and are not considered in this study.

The second modelling approach is based on treating the wave energy spectrum as the dependent variable. These "spectral models" generally ignore diffractive effects but include energy sources and sinks, and attempt to incorporate the nonlinear exchanges of energy between different frequencies. Spectral models are statistical predictors in the sense that they do not provide the heights and phases of individual large waves in the solution domain. This type of information must be obtained probabilistically and through the separate application of wave kinematics theory.

This study is concerned with the performance of two shallow-water

spectral wave models under storm conditions. The study objectives were:

- (1) to compare model predictions with measurements of wave height, peak period, direction and spectral shape with a view to determining model accuracy, and
- (2) to compare the relative performance of the two models, which differ in their formulation of the governing physical processes.

Specifically, a first-generation spectral model developed by Seaconsult (called SPECREF--Hodgins and Niwinski, 1987) has been compared with a second-generation model (WAVAD), described by Resio (1982, 1987) for the complex bottom topography of Sable Island Bank. The emphasis in these comparisons was placed on their shallow water performance in water depths outside the surf zone but less than 30 m.

The two models incorporate different algorithms for the sources and sinks of wave energy in the governing radiation balance equation, and accordingly are expected to differ in their ability to predict spectral characteristics in shallow water, especially under conditions of strong wave generation. In order to provide an understanding of the distinctions in the formulation of wave physics embodied in each model, a brief review of the important processes is given next. This review isolates the critical issues to be examined here. It is followed by a mathematical description of the two models. Subsequent chapters describe the new directional wave measurements made in this study, how the models have been applied to Sable Island Bank and the model results from four hindcasted storms and two hypothetical tests.

### 1.2 Spectral Wave Models

The equation governing the transformation of wavenumber spectra  $S(k, \theta)$  is (Phillips, 1977)

$$\left\{ \frac{\partial}{\partial t} + (\mathbf{c}_g + \mathbf{U}) \cdot \nabla \right\} S + \tilde{\mathbf{R}} \cdot \nabla \mathbf{U} = Q \quad (1.1)$$

where  $k$  = wavenumber ( $2\pi/L$ )

$\theta$  = direction

$\mathbf{c}_g$  = group velocity vector

$\mathbf{U}$  = mean current vector

$\tilde{\mathbf{R}}$  = radiation stress tensor

(Longuet-Higgins and Stewart, 1960)

$Q$  = represents the net source term combining energy losses, energy gains from the wind and nonlinear energy fluxes between waves of different length and frequency.

For the case where  $\mathbf{U} \equiv 0$  (no currents) and  $Q \equiv 0$ , (1.1) reduces to the form

$$S(f, \theta) = \left\{ \frac{c_{g_o} \cdot k}{k_o \cdot c_g} \right\} \cdot S_o(f, \theta) \quad (1.2)$$

governing spectral refraction. This equation is equivalent to

$$S(f, \theta) = K_s^2 K_r^2 \left\{ \frac{\partial \theta}{\partial \theta_o} \right\} \cdot S_o(f, \theta) \quad (1.3)$$

where  $K_s$  = shoaling coefficient

$K_r$  = refraction coefficient

$\frac{\partial \theta}{\partial \theta_o}$  = Jacobian allowing for the change of angle from deep to shallow water.

and the subscript "o" denotes deep water (Dorrestein, 1960; L  m  haut   and Wang, 1982). Karlsson (1969) showed that (1.2), where the spectrum is expressed in  $(f, \theta)$  space rather than wavenumber space, is equivalent to Longuet-Higgins (1956; 1957) requirement that energy density defined per unit area of wave number space remains constant along a wave ray (in the absence of source terms).

Equation (1.2) has been the starting point for several spectral refraction models. Collins (1972) described a shallow-water wave model

where he first constructs wave rays in the conventional way (Munk and Arthur, 1951) and then applies (1.2) along each ray. Collins accounts for frictional losses and wave generation, and introduces an equilibrium spectrum to model wave breaking. By solving over all frequencies and directions, Collins constructs a shallow-water spectrum  $S(f, \theta)$ . Very similar approaches have been followed by Abernethy and Gilbert (1975), Cavaleri and Rizzoli (1981), and Seaconsult in their model SPECREF; these models approach the problem formulation the same way but differ in the treatment of wind input, bottom interactions, and wave breaking.

Shiau and Wang (1977) on the other hand solve the ray equation and (1.2) on a uniform Cartesian grid. One limitation of this method is that many points are required to model the area of interest. To keep mesh sizes reasonably small, Shiau and Wang use Krasitskii's (1974) analytical solutions for straight, parallel isobaths to bring deep water spectra into the edge of the numerical solution domain.

Wang and Yang (1981) applied an extended version of the Shiau-Wang model, including bottom friction and a breaking criterion, to measurements at Sylt in the North Sea. Results are limited, and quite variable: predicted versus measured wave spectra from Collins (1972) and Wang and Yang (1981) are shown in Fig. 1.1.

The central problem in this type of approach is that each frequency is considered independently of every other frequency in the spectrum. Consequently no attempt is made to model the effects of nonlinear energy transfers between different wave components. This sets aside a central tenant advanced recently that the nonlinear processes can, in general, account for most of the dissipation as irregular waves progress into shallow water (Resio, 1982; 1987). In these frequency-independent spectral models, one must include a mechanism to model wave breaking, or otherwise limit wave height. Bottom friction alone cannot be consistently modelled so as to produce self-similar spectra over all seabed materials. One approach has been to impose a depth-dependent equilibrium range spectrum to limit the shoaled and refracted energy (see e.g. Grosskopf and Vincent, 1982). One such saturation range

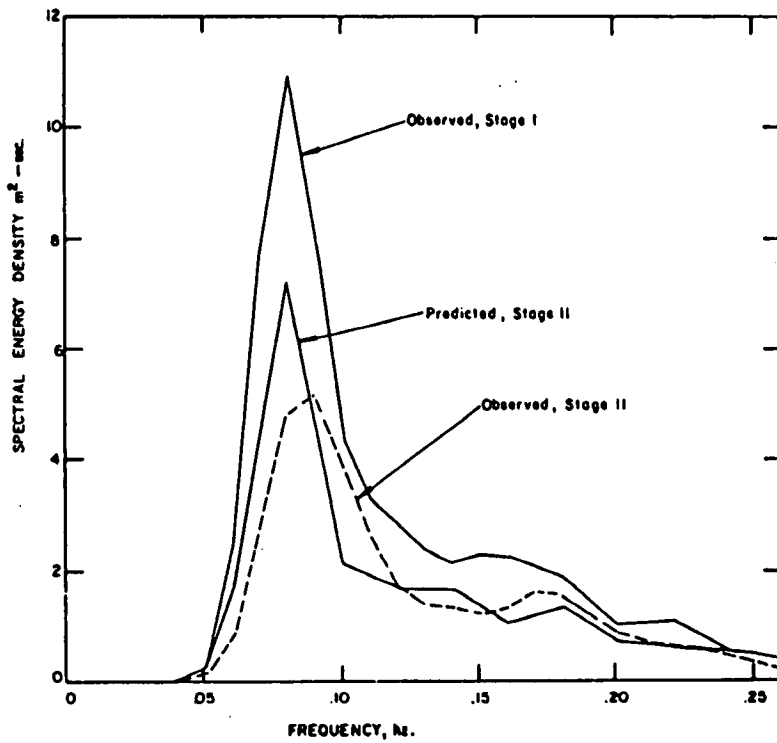
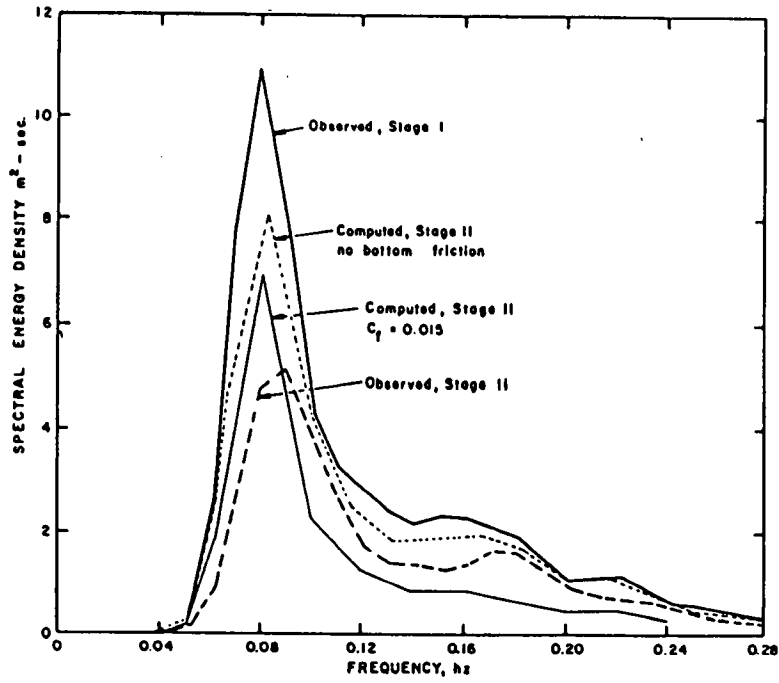


Fig. 1.1a Computed and observed spectra using parallel bottom topography (top) and irregular bottom topography (bottom) from Collins (1972).



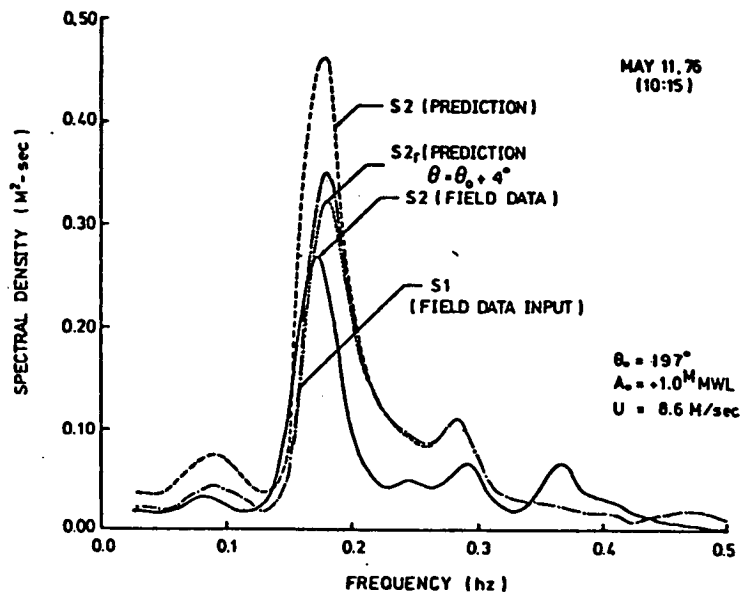
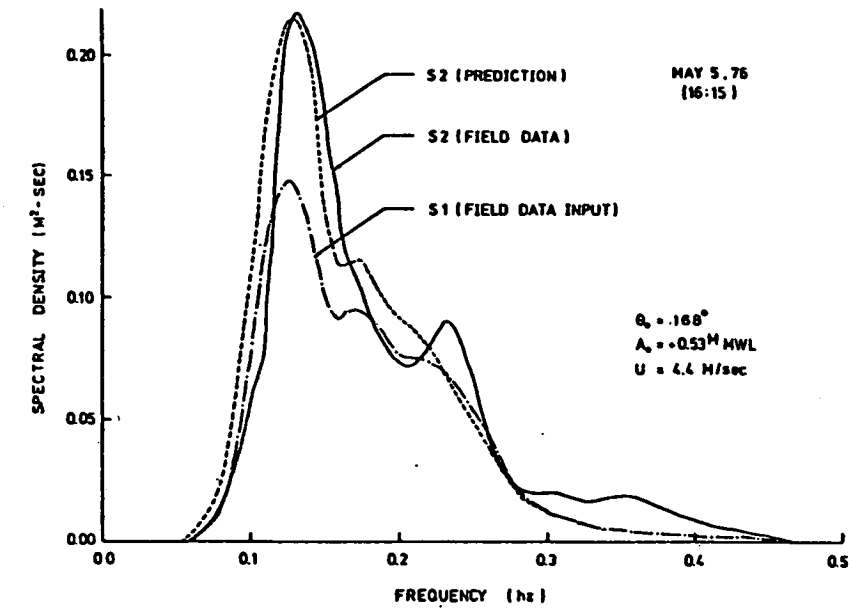


Fig. 1.1b Comparison of computed and measured deep-water spectra. Upper panel: data from 76-05-05-16:15. Lower panel: data from 76-05-11-10:15. (Source: Wang and Yang, 1981).

spectrum, proposed by Kitaigorodskii et al. (1975), is

$$E_k(f) = \alpha g^2 (2\pi)^{-4} f^{-5} \phi(kh) \quad (1.4)$$

where  $\alpha$  = scaling coefficient (0.0081), and

$$\phi(kh) = \frac{\sinh^3(kh)}{[\cosh(kh)(kh + \sinh(kh)\cosh(kh))]} \quad (1.5)$$

The function  $\phi(kh)$  varies from 1.0 in deep water to  $(kh)^2$  in shallow water; consequently, spectra in deep water exhibit an  $f^{-5}$  dependence in the equilibrium range, changing to an  $f^{-3}$  dependence in shallow water. As formulated by Kitaigorodskii et al., (1.4) is independent of the wind speed  $U_{10}$  and is a strong function of water depth. Thornton (1977) independently argued on dimensional grounds that if the wave phase speed  $c$  were taken as the variable responsible for breaking, the equilibrium range should obey an  $f^{-3}$  dependence in shallow water ( $c^2=gh$ ). In deep water,  $c^2=(2\pi)^2g^2/f^2$  and one recovers an  $f^{-5}$  dependence as shown in (1.4). The  $f^{-3}$  variation is in agreement with Dreyer's (1973) measurements.

For models formulated in this manner, refraction, shoaling, and wind input of energy are balanced by whatever frictional mechanisms are included as the dominant processes governing spectral transformation until the equilibrium range function dominates the modelled range of frequencies. The role of wave-wave interactions in producing self-similar spectral forms is ignored in the energy exchange balance contained in (1.1).

Recently a new theory has emerged that leads to a consistent model for wave spectra in water of any depth; here the nonlinear wave-wave interactions and wind input play dominant roles under conditions of active wave generation compared with refraction and sea bed frictional losses. This theory may be understood with reference to Fig. 1.2. Kitaigorodskii (1983) has postulated the existence of an equilibrium range where the input of energy from the atmosphere is balanced by the nonlinear wave-wave interaction processes. The nonlinear energy fluxes transfer energy from the central region just to the right of the

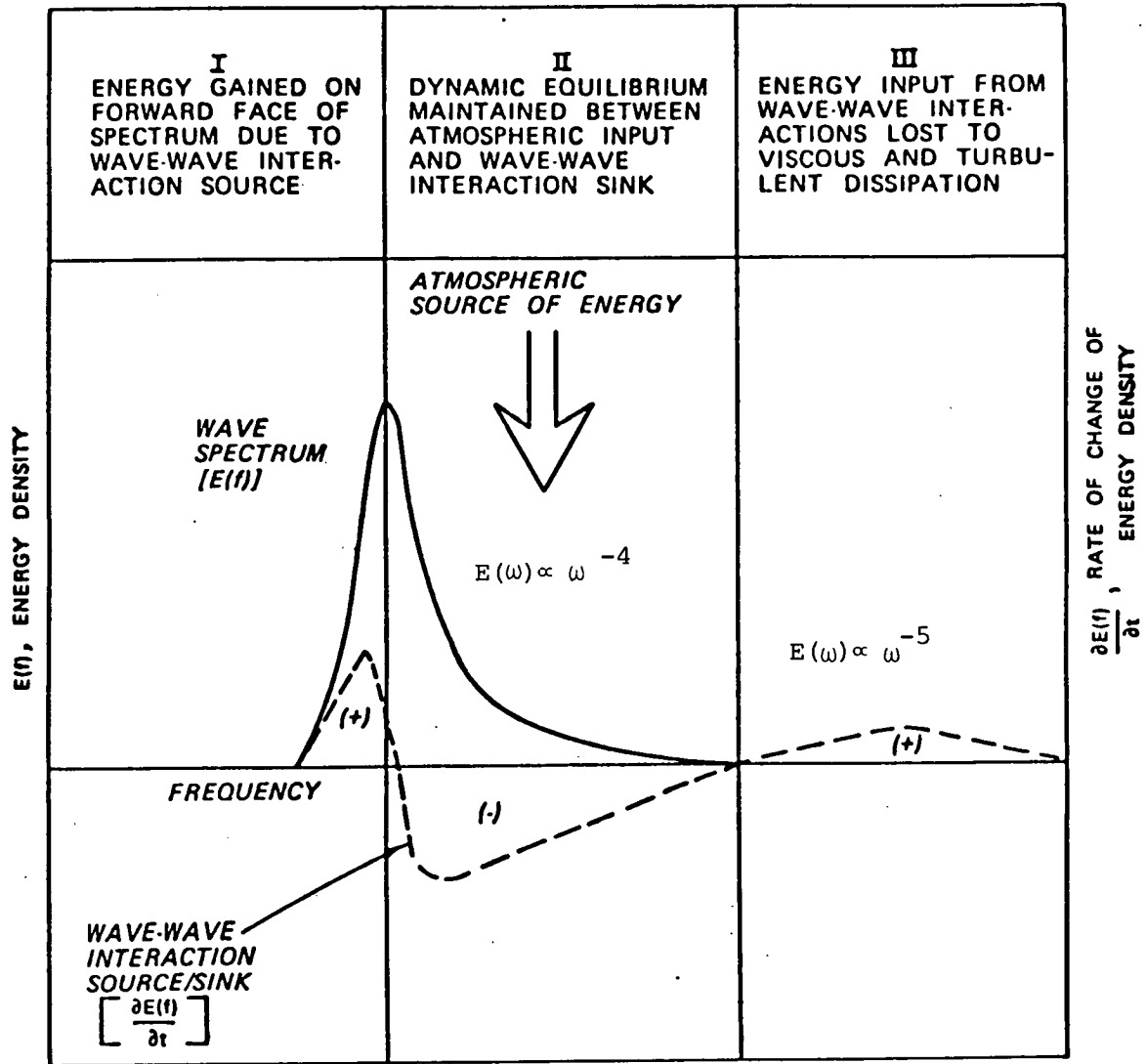


Fig. 1.2 Schematic diagram of the wind-wave energy spectrum during active growth and the wave-wave interaction source/sink function. (Source: Resio, 1982).

spectral peak  $\omega_m$  both to higher frequencies, where energy is ultimately lost to breaking, and to lower frequencies where it shows up as growth on the forward face. Kitaigorodskii draws an analogy to Kolmogoroff's equilibrium range in turbulence to postulate that in the frequency spectrum of wind-generated waves there exist separate regions of wave generation and wave dissipation, and that in the generation region the energy flux  $\epsilon(k)$  is constant ( $= \epsilon_0$ ) over a range of wave numbers  $k$ . For an isotropic dispersion relation for waves this leads to an expression for the wave spectrum of the form

$$E(\omega) = \alpha \epsilon_0^{1/3} g \omega^{-4} \quad (1.6)$$

The  $\omega^{-4}$  dependence is in agreement with recent observations (Forristall, 1981; Kahma, 1981; Donelan et al., 1985).

To determine a universal form for (1.6) the energy flux  $\epsilon_0$  was equated to the wind input energy flux. This latter flux is proportional to  $\rho_a U_{10}^3$  and provides a wind-dependent saturation form

$$E(\omega) = \alpha_u g U_{10} \omega^{-4} \quad (1.7)$$

where  $\alpha_u$  is a universal, nondimensional constant ( $\alpha_u \cong 0.0045$ ; Kitaigorodskii, 1983).

Resio (1982; 1987) has invoked the same assumption as Kitaigorodskii regarding the separation of generation and dissipation ranges, and has shown that in general the nonlinear fluxes play a dominant role in preserving spectral similarity in water of any depth under conditions of active generation. Resio's results, based on geometric similitude in the Boltzmann collision integral representing the nonlinear wave-wave interactions, give two limits for equilibrium spectra: (a) in deep water

$$E(\omega) = 2B'g^2(2\pi)^2\omega^{-4} \quad (1.8)$$

which differs from (1.18) only in terms of the constant, and  $B'$  which is a dimensional variable with units of time, and (b) in shallow water

$$E(\omega) = B'gh(2\pi)^2\omega^{-2} \quad (1.9)$$

Resio (1987) in formulating a solution to (1.1) for water of arbitrary depth evaluates  $Q$  mainly in terms of this flux of energy into the central frequencies from the wind, and the nonlinear fluxes of energy out of the generation range of frequencies to higher and lower frequencies due to wave-wave interactions. The balance of these fluxes provides the primary changes in energy at each frequency from one time level to the next. Additional sinks due to bottom friction, and to exchanges of energy between swell and opposing winds may be added, but these are generally small.

To confirm the hypothesis that nonlinear fluxes are critical to the energy balance under periods of strong wind forcing, and serve as an importance sink term under low wind conditions as well, Resio (1988) has evaluated the relative importance of four source-sink terms: nonlinear fluxes, shoaling, wind input and refraction for six cases where simultaneous deep and shallow water data exist together with overwater winds. Bottom friction was neglected. These comparisons tended to demonstrate that nonlinear energy fluxes could approximate observed losses, under a variety of wave conditions (active generation to swell transformation), without recourse to a variable bottom friction source term.

Applications of the same theory of wave transformation at laboratory scales are also reported by Resio (1988) and support the hypothesis. These results suggest that bottom friction may be a relatively small term in the balance equation for shallow water under most storm conditions. One consequence of this result is that the processes governing wave transformation would not tend to be highly site-specific, except perhaps for conditions of energetic swell propagating over very soft bottom materials.

This conclusion is almost exactly the opposite to that evolving out of Shemdin's work published between 1977 and 1982 (Shemdin et al., 1977; Hsiao and Shemdin; 1978; Shemdin et al., 1980). Shemdin et al. (1977), for example, evaluated the relative importance of bottom friction, shoaling and refraction, and nonlinear energy fluxes during the

transformation of spectra over fine sands ( $D_{50} \cong 0.20$  mm) off Marineland, Florida (Fig. 1.3). Friction and refraction-shoaling were found to dominate near the spectral peak, with nonlinear fluxes becoming important only at high frequencies (wave periods  $< 5$  s). A second example from Shemdin et al. (1980) (Fig. 1.4) gives a similar result for spectral transformation from 17 m to 13 m water depth over a propagation distance of 18 km.

By examining these and other sites with widely varying bottom conditions they concluded that wave transformation would be dominated by different processes at different sites, and that wave modelling would require data on bottom materials along the transformation path. (We note that for Shemdin et al.'s example in Fig. 1.3,  $h/gTp^2 \sim 0.0144$  and  $H_s/gTp^2 \sim 0.0022$  and the waves as characterized by significant height and peak period are not particularly nonlinear. Shemdin et al. (1980) have shown that the importance of the nonlinear fluxes, evaluated by an approximation due to Herterich and Hasselmann (1980), is highly dependent on wave steepness ( $k_p h$ ). For  $H_s = 1.5$  m in  $h = 10$  m,  $k_p h \cong 0.85$  which places their estimate of nonlinear fluxes in a range from nearly equal to bottom friction to about one order of magnitude below bottom friction in terms of controlling the spectral transformation, depending on the choice of coefficients.)

The spectral models thus fall into two groups (SWAMP, 1985):

- (1) Decoupled propagation models wherein nonlinear fluxes due to resonant wave interactions are totally ignored, and transformed spectra  $S(f, \theta)$  are governed by refraction-shoaling, dissipation due to bottom interactions and some form of equilibrium spectrum to incorporate the effects of wave breaking; and
- (2) Coupled-discrete models wherein the evolution of the discrete energy spectrum  $S(f, \theta)$  is governed mainly by a balance between nonlinear fluxes calculated from wave-wave interactions (frequency coupled) and other source-sink terms describing wind input and losses due to bottom interactions, refraction, shoaling and wave

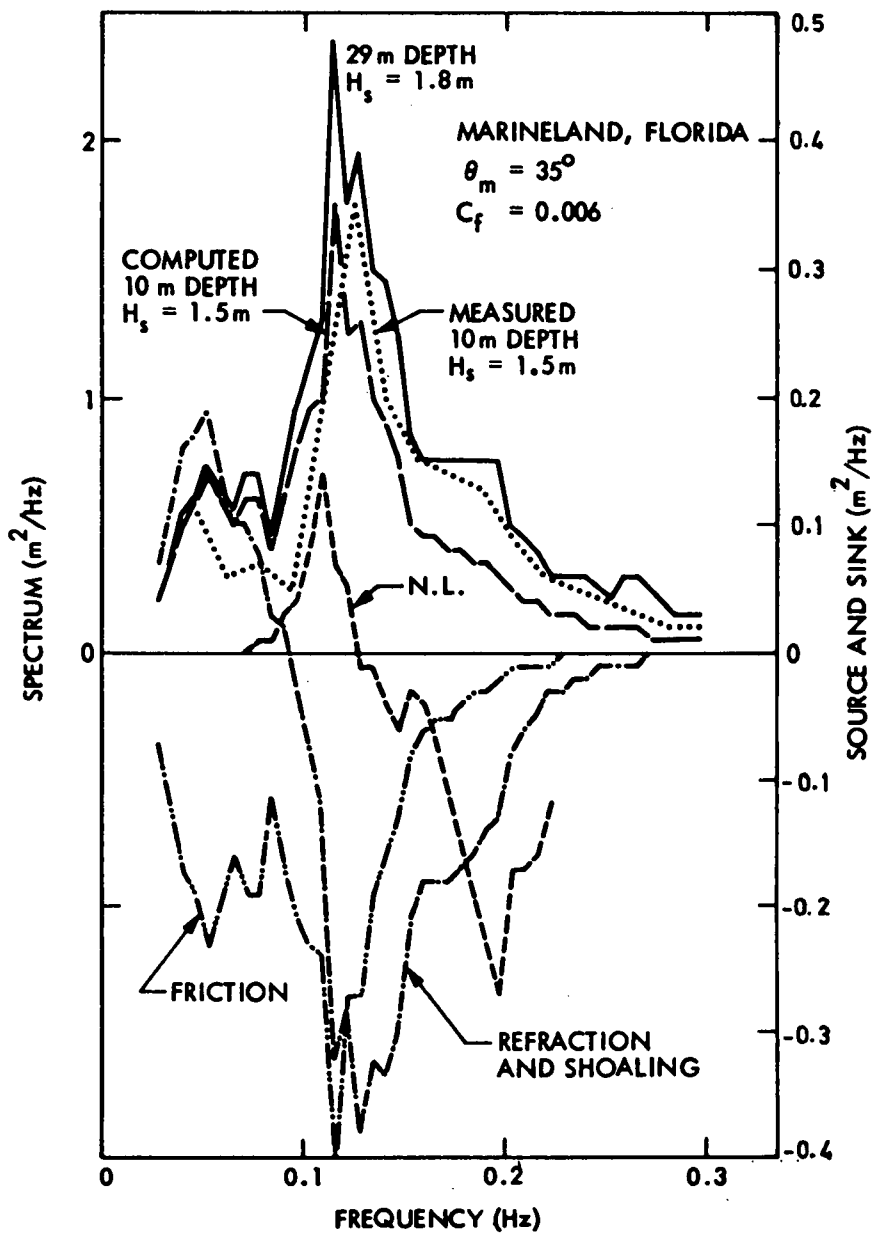


Fig. 1.3 Computed and measured wave transformation at the Marineland site. The spectrum at 10 m depth is computed from the measured spectrum at 29 m depth as initial value. The source and sink scale refers to the total contribution from 29 to 10 m depth. (Source: Shemdin et al., 1977).

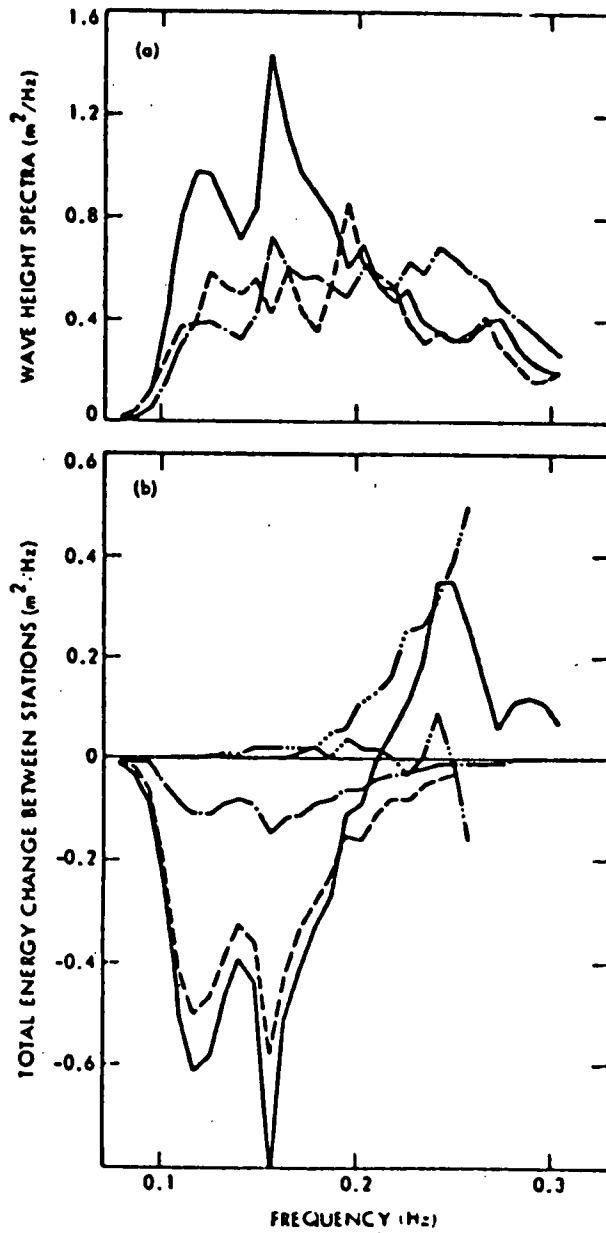


Fig. 1.4 Wave transformation in finite depth water: the solid curve is the measured spectrum, the dashed curve denotes the measured spectrum inshore and the dot-dashed curve is the computed spectrum inshore using the solid curve as input. The energy changes computed in the lower panel include frictional dissipation (--), refraction and shoaling (-.-), nonlinear wave transfer (-.-.-), all adding up to the solid curve. (Source: Shemdin et al., 1980).



breaking.

The open question concerns the relative importance of the nonlinear fluxes versus bottom losses and wind input. Resio's work indicates the nonlinear processes are essential and generalize to different sea bed conditions. On the other hand Shemdin's results suggest that the balance is highly variable and strongly linked to the particular bottom materials in each location. If the first premise is true the decoupled propagation models should fail to give realistic spectra in shallow water except where the spectral shape is largely governed by the equilibrium range function.

Two models were selected, one from each of the two groups described above, to reveal differences in predicted wave properties that could be attributed to fundamental differences in their formulation. Specifically, the issue to be addressed was the practical importance of including nonlinear fluxes due to wave-wave interactions versus more primitive, but somewhat simpler models, gauged against wave heights, periods, directions, and spectral shapes in storm-generated seas in shallow water.

Directional wave data for this purpose were not available in Canadian waters, and other data sets (MARSEN, ARSLOE, TEXEL--see Bouws et al., 1985) had limitations in terms of lack of directional data, water depth, wave heights, and availability. For these reasons new, directional data were collected on the exposed seaward side of Sable Island in water depths ranging from 200 m to 12 m. These data, together with one storm monitored previously, were used to evaluate the models.

### 1.3 WAVAD: A Coupled Discrete Spectral Model

Theoretical aspects of this model are given in a series of papers published by D. Resio (Resio, 1981; 1982; 1987; 1988) and so only a summary of key points is presented here, together with the application to Sable Island Bank. Solutions to (1.1) are obtained under the following assumptions:

- (1) The dominant source-sink terms are wind input, wave breaking and frictional dissipation.
- (2) Under active generation conditions the nonlinear fluxes play a central role in preserving self-similar spectral shapes.
- (3) Wave-current interactions are ignored ( $U=0$ ).
- (4) Wave diffraction and reflection are negligible.
- (5) Energy is limited by a depth-dependent saturation law having an  $\omega k^{-3}$  dependence.

In WAVAD solutions to (1.1) are obtained for  $U=0$  using a fractioned step procedure (Yanenko, 1971) by recasting the governing equation as

$$\left\{ \frac{\partial}{\partial t} + C_g \cdot \nabla \right\} S = 0 \quad (1.10)$$

$$\frac{\partial S}{\partial t} = Q_{in} + Q_{nl} + Q_b \quad (1.11)$$

Equation (1.10) is solved using characteristic rays, reverse propagated from each grid point at the new time level to intersect the solution for  $S$  at the previous time level. The equation for energy conservation

$$\frac{c \cdot c_g}{4\pi^2 f} S(f, \theta) = \text{constant} \quad (1.12)$$

is then solved along each ray for given  $(f, \theta)$ , taking the old-time level value for  $S$  as the initial value.

In the second step the propagated spectrum at the new time level is modified to account for energy input, changes in spectral shape due to nonlinear fluxes and bottom friction losses. Wave growth is formulated

as

$$\frac{\partial S}{\partial t} = B(f, \theta) \cdot S(f, \theta) \quad (1.13)$$

$$\text{where } B = z f_m^*{}^2 f \cos(\theta - \beta) \quad (1.14)$$

$$f_m^* = f_m B/g$$

$\beta$  = wind direction

$z$  = dimensionless constant

From Kitaigorodskii (1983),

$$E(f) = \frac{\alpha_u U g f^{-4}}{(2\pi)^3} \quad (1.15)$$

for the equilibrium range of the wave spectrum, where  $E(f)$  is the one-dimensional spectrum obtained by integrating  $S(f, \theta)$  over all directions, and  $\alpha_u$  is a universal constant (0.0042). Integration of (1.13) with respect to  $f$  and  $\theta$  with (1.14) and (1.15) substituted into it gives

$$\frac{\partial E_o}{\partial t} = \frac{RU^3}{g} \quad (1.16)$$

where  $R$  is a dimensionless constant of  $O(3 \times 10^{-7})$  and  $E_o$  is total energy. Equation (1.16) provides the change in energy due to the local wind.

Resio (1987) has shown that at frequencies above  $f_m$  the energy balance between nonlinear fluxes and wind inputs leads to an equilibrium range of the form given in (1.15). The consistent wave-wave interaction flux term can be written

$$\frac{\partial E'_o}{\partial t} = \frac{\varepsilon E_o'^3 k_m^{9/2}}{\tanh^{3/4}(k_m h)} \quad (1.17)$$

$$\text{where } E'_o = \int_{f_m}^{\infty} E(f) df \quad (1.18)$$

$\varepsilon$  is a constant of  $O(10^2)$  and  $k_m$  is the wave number at  $f_m$ . This flux represents a loss to the equilibrium range.

On the forward face of the spectrum the energy gain due to wave-wave interactions can be written in terms of a fixed proportion of the total wave-wave interaction momentum flux. With the equilibrium range in (1.15), this leads to a net gain of wave energy through time of the form

$$\frac{\partial E_O}{\partial t} = q r^3 \frac{u_*^2 c_m}{g} \quad (1.19)$$

where  $r$  is the ratio of the actual equilibrium range coefficient to the "universal" value and  $q$  is a dimensionless constant.

Bottom friction is specified as:

$$Q_b = \frac{-C_f g k c_g}{2\pi\omega^2 \cosh^2(kh)} \cdot S(f, \theta) \langle u \rangle \quad (1.20)$$

where  $C_f$  is a nondimensional drag coefficient, and

$$\langle u \rangle = \left[ \sum E(f) \frac{g^2 k^2}{\omega^2 \cosh^2(kh)} \Delta f \right]^{1/2} \quad (1.21)$$

$$\text{and } E(f) = \frac{S(f_i, \theta_j)}{S_o(f_i, \theta_j)} \cdot E_o(f) \quad (1.22)$$

with the subscript  $o$  denoting deep water, and

$$c_g = \frac{1}{2} \left\{ 1 + \frac{2kh}{\sinh 2kh} \right\} c \quad (1.23)$$

The saturation spectrum used in WAVAD has a wavenumber dependence

$$E(k) = B' \omega k^{-3} \quad (1.24)$$

where  $B'$  is a dimensional constant with units of  $\text{time}^{-1}$ .

In applications over a large geographical area  $f_m$  is scaled in the model in terms of a propagation operator that accounts for existing wave energy over the grid, and a change in the local spectrum produced by wind growth balanced by energy fluxes to the dissipation range and to the forward face. Over smaller geographical areas such as the shallow water domain on Sable Island Bank it may be assumed that the peak

frequency does not change significantly in the time required for waves to propagate across the area. Under these conditions  $f_m$  may be treated as approximately constant.

This assumption has been made for the Sable Island applications where  $f_m$  has been derived at each grid point  $(x,y)$  using bilinear interpolation of values calculated on the deep water boundaries. In fact, inspection of  $f_m$  over the intermediate grid showed it to be a slowly varying function of space. Consequently this approximation is reasonable provided that purely shallow water effects produce little change in  $f_m$ . (Note that constant frequency  $f$  is the basis of conventional wave transformation theory in shallow water.)

#### 1.4 SPECREF: A Decoupled Propagation Model

Equation (1.1) is solved to give the directional wave frequency spectrum  $S(\mathbf{x}, f, \theta)$  at a specified location  $\mathbf{x}$  for an arbitrary depth field resolved on a regular Cartesian grid with spacing  $\Delta x$ . The following assumptions are invoked:

- (i) The dominant source-sink mechanisms are wind input, and bottom friction; nonlinear energy fluxes between different frequencies are adequately parameterized by the saturation spectrum.
- (ii) Wave-current interactions are ignored ( $U=0$ ).
- (iii) Wave diffraction and wave reflection are negligible.
- (iv) Energy losses due to opposing winds are negligible.
- (v) Energy is limited by the depth-dependent saturation law (Kitaigorodskii et al., 1975), given by (1.4).

Under these assumptions (1.1) may be restated in frequency space as

$$\left\{ \frac{\partial}{\partial t} + \mathbf{c}_g \cdot \nabla \right\} S = Q_{in} + Q_b \quad (1.25)$$

where  $Q_{in} = B \cdot S(f, \theta)$  (wind source term),

$$B = \begin{cases} 5f \left\{ \frac{\rho_a}{\rho_w} \right\} \left\{ \frac{U \cos \beta}{c} - 0.90 \right\}, & \frac{U \cos \beta}{c} > 0.90 \\ 0 & \frac{U \cos \beta}{c} \leq 0.90 \end{cases} \quad (1.26)$$

$U$  = wind speed at 10 m (m/s)

$\beta$  = angle between the wind and wave directions

$c$  = wave phase speed

$$= \frac{g}{k} \tanh(kh) \quad (1.27)$$

$\rho_a, \rho_w$  = air and water densities respectively ( $\text{kg/m}^3$ )

$$Q_b = - \frac{C_f g k c_g}{2\pi \omega^2 \cosh^2(kh)} \cdot S(f, \theta) \langle u \rangle \quad (1.28)$$

(bottom friction sink term)

$C_f$  = nondimensional drag coefficient

$$\langle u \rangle = \left[ \sum_f E(f) \frac{g^2 k^2}{\omega^2 \cosh^2(kh)} \cdot \Delta f \right]^{1/2} \quad (1.29)$$

$$E(f) = \frac{S(f_i, \theta_j)}{S_o(f_i, \theta_j)} \cdot E_o(f) \quad (1.30)$$

(subscript o denotes deep water)

$$c_g = \frac{1}{2} \left\{ 1 + \frac{2kh}{\sinh(2kh)} \right\} c \quad (1.31)$$

and may be solved subject to the boundary conditions  $S(\mathbf{x}_b, f, \theta)$  on all open water boundaries and the fields of 10-m wind  $U(\mathbf{x})$  and depth  $h(\mathbf{x})$ . The initial condition is  $S(\mathbf{x}, f, \theta) \equiv 0$ .

The formulation for  $Q_{in}$  follows that used by Cavaleri and Rizzoli (1981) and  $Q_b$  is equivalent to the method published by Collins (1972).

With  $Q=0$ , (1.25) can be written as a homogeneous transport equation in wave energy with characteristics given by the set of wave rays radiating outward from the location  $\mathbf{x}$  for all  $(f, \theta)$ . If these characteristic curves are known, then the energy conservation equation may be written as

$$\frac{dS}{dt} = Q \quad (1.32)$$

where the time integration is along each characteristics for  $(f, \theta)$ . Adopting the general form for (1.2) (Longuet-Higgins, 1957)

$$\frac{c \cdot c_g}{4\pi^2 f} S(f, \theta) = \text{constant} \quad (1.33)$$

as the quantity conserved along each characteristic in the absence of source-sink terms, and noting the equivalence of time-space integration given by  $ds = c_g dt$  we have for (1.32)

$$\frac{d}{ds} \left\{ \frac{c \cdot c_g S}{4\pi^2 f} \right\} = \frac{1}{c_g} \left\{ Q_{in} + Q_b \right\} \quad (1.34)$$

The numerical solution is computed in two steps. First the characteristic wave rays are calculated using linear refraction theory over the specified  $h(\mathbf{x})$  for a discrete set of frequencies and directions  $(f_i, \theta_j, i=1,2,\dots,I; j=1,2,\dots,J)$ . The rays are reverse-traced until they intersect an open sea boundary or land. Second, (1.34) is integrated along each ray for given  $f_i$  and  $\theta_j$  at the point of interest in shallow water using a forward stepping procedure.

The boundary conditions are supplied at the end of each characteristic ray, either from measured, hindcast or parametric directional spectra in deep water, or  $S(\mathbf{x},f,\theta) = 0$  for land points.

The accuracy of the numerical solution depends among other factors on the method of solving for the position of the characteristic rays. Procedures in SPECREF are fairly conventional: by definition

$$\frac{dx}{ds} = \cos A, \quad \frac{dy}{ds} = \sin A \quad (1.35)$$

where  $A$  is the angle between the ray and the  $x$ -axis,  $dx$  is a small incremental distance in  $x$ , and  $ds$  is an incremental distance along the ray. Given the initial position of the ray  $(x_0, y_0)$  the position  $(x, y)$  of the end of the ray at distance  $ds$  is found from

$$(x = x_0 + ds \cos \bar{A}, y = y_0 + ds \sin \bar{A}) \quad (1.36)$$

The new position is improved by successive approximations of the angle  $\bar{A}$  which is formed as an average of the angles at  $(x_0, y_0)$  and  $(x, y)$ .  $A(x, y)$  is calculated at each iteration from

$$A_{k+1} = A_k + ds \left\{ \sin A_k \frac{dc}{dx} - \cos A_k \frac{dc}{dy} \right\} \quad (1.37)$$

The free parameter specified to the program is  $ds$ ; in principle the smaller the value for  $ds$  the more rapid is the convergence to the true characteristic path, within the limits of the resolution afforded by the Cartesian grid spacing  $\Delta x$ . The two derivatives  $dc/dx$  and  $dc/dy$  are specified on the Cartesian grid and so are resolved only as well as is



$h(\mathbf{x})$ . Thus  $\Delta x$  is the other free parameter whose magnitude is related to the seabed slopes in the area of interest. In practice  $ds/\Delta x = O(1)$  is used.

Finally, equation (1.4) is used as an upper bound on wave energy to the right of  $f_p$ . It is applied by computing  $S_u(f, \theta)$  at the location of interest as above, evaluating

$$E_u(f_i) = \sum_{j=1}^J S_u(f_i, \theta_j) \Delta\theta \quad (1.38)$$

where  $u$  denotes "unscaled" quantities, and computing

$$S(f_i, \theta_j) = S_u(f_i, \theta_j) \cdot E_{KKZ}(f_i) / E_u(f_i) \quad (1.39)$$

with  $E_{KKZ}$  designating (1.4). This saturation law introduces into the model another free parameter,  $\alpha$ --the "Phillips parameter". It is noted that (1.4) provides for an  $f^{-5}$  deep water dependence of the rear face of the spectrum. This is not in agreement with the  $f^{-4}$  dependence and hence leads potentially to some mismatch in spectral shape. It may be noted also that this type of saturation procedure may lead to a lowering of  $f_p$  in shallow water. This can occur if energies near  $f_p$  are well above saturation before imposition of (1.39). This tendency must also be examined in evaluating the performance of SPECREF.

The formulation of SPECREF outlined above yields a model with seven independent parameters to be specified in each application:

- $\Delta x$  (equal in both  $x$  and  $y$ )
- $\Delta f$  (frequency resolution)
- $\Delta\theta$  (directional resolution)
- $ds$  (ray step size)
- $\alpha$  (Phillips' parameter in (1.4))
- $B$ -growth coefficient in (1.25)
- $C_f$  - bottom friction coefficient.

Specification of these parameters for the Sable Island Bank application is discussed below.

## 2.0 SHALLOW WATER WAVE DATA

### 2.1 The 1984-85 Field Program

Wave data were collected at four locations to the south of Sable Island to provide concurrent deep and shallow water measurements for validation of the two spectral models. These locations are shown in Fig. 2.1 together with the position of other buoys deployed at the same time near operating drilling platforms. The 1984-85 field program lasted from December 19, 1984 to February 21, 1985. Instrument disposition and data recovery are shown in Table 2.1.

The main focus of the 1984-85 program was a line of measurements from deep water ( $h > 200$  m) where the WRIPS buoy was placed, into 12 m of water at station 253. Directional data in shallow water were given a priority for examining the effects of refraction on inshore spectra; consequently WAVEC buoys were placed at both stations 252 and 253. This choice reflects a compromise made between available instrumentation and transmission range to receiving platforms, and the desirability of directional deep-water measurements to confirm and/or provide boundary data to the shallow water transformation models.

A line to the south of the island was chosen to give good exposure to open ocean storm generated seas propagating into shallow water over a relatively uncomplicated bathymetry. Transects chosen over East Bar or West Bar would give more complex nearshore spectra due to the complicated bathymetry toward deep water, and especially due to the effects of partial sheltering by the island itself and the bars extending several kilometres outward from the island. Fig. 2.2 shows the southern flank of the island looking toward the 1984-85 transect. East Spit and the shallow bar extension over East Bar are shown in Fig. 2.3; this is a fairly linear zone of intense wave breaking extending some 10 km northeastward from the island. This feature is difficult to resolve in shallow water transformation models as is the degree of energy loss, reflection, and transmission over the bar. Much the same situation is found over West Bar. For these reasons a southern exposure was deemed to be the most desirable for this experiment.

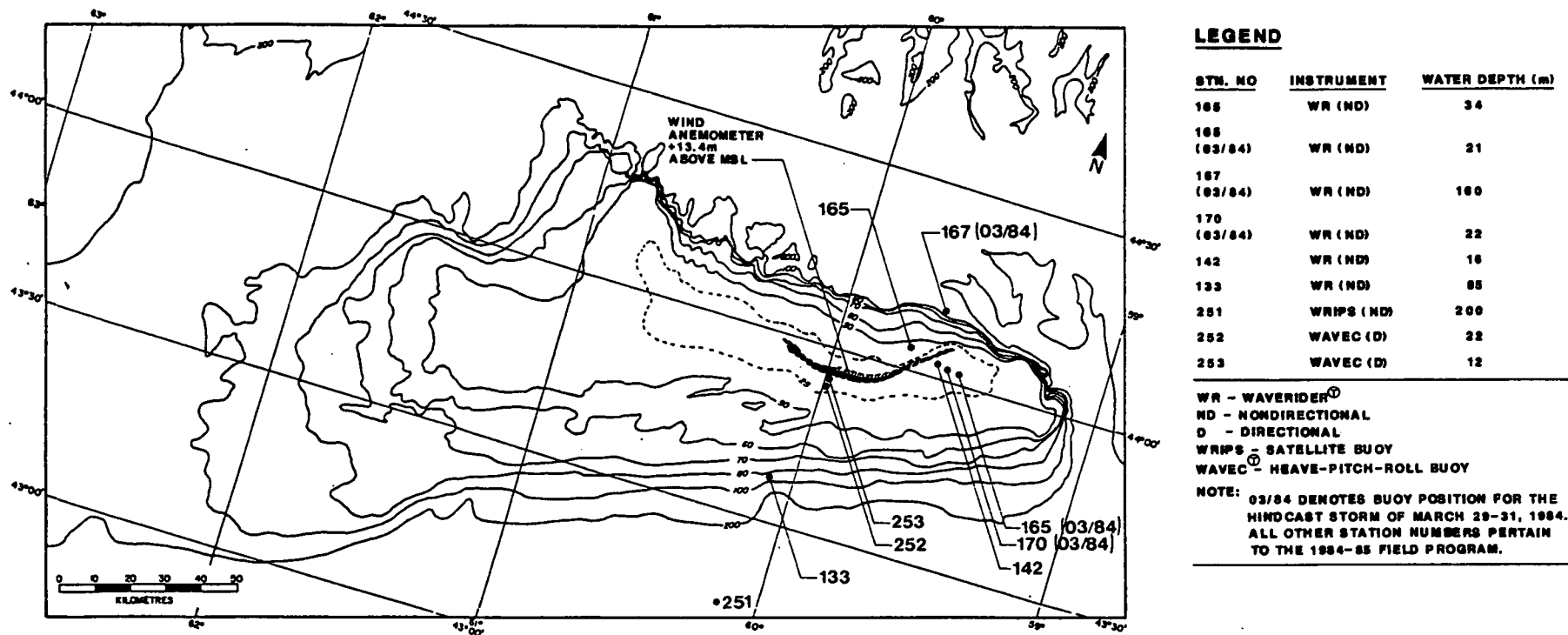


Fig. 2.1 Disposition of wave and wind instrumentation providing data for the wave model intercomparison.





Fig. 2.2 Oblique photograph of the southern flank of Sable Island as viewed from the east, looking west.

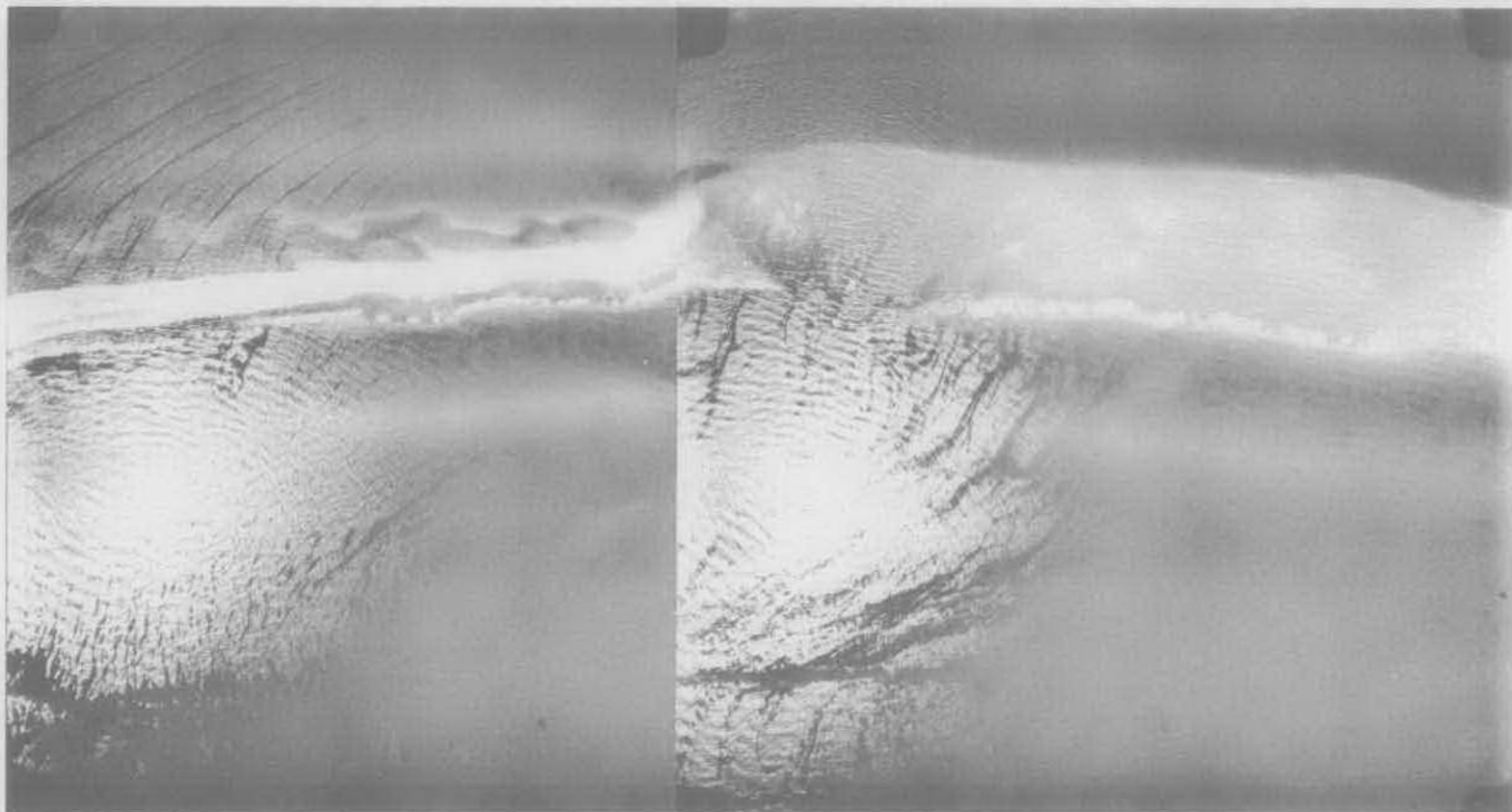


Fig. 2.3 Aerial photograph of East Spit and the shallow bar extension that produces a linear zone of breaking waves extending approximately 10 km northeast of the island.

A detailed map of the shallow water bathymetry is shown in Fig. 2.4. Inshore of the 50 m isobath the topography is characterized by a series of SW-NE shoreface connected ridges (Amos and King, 1984) of low relief. Normal to these ridges depth changes are of the order of 3 to 5 m in a run of 400 to 1000 m. Bottom materials were not sampled along the transect but are expected to be consistent with fine sands overlying medium to coarse sand lag layers found in this area. A detailed sampling program has been reported by Hodgins et al. (1986) for a site further east ( $43^{\circ}56.4'N$   $59^{\circ}39.6'W$ ) located on one of the shoreface connected ridges; a representative grain size distribution is shown in Fig. 2.5 for the fine sand layer. In the lag sands with  $D_{50} = 1.0$  mm are typical.

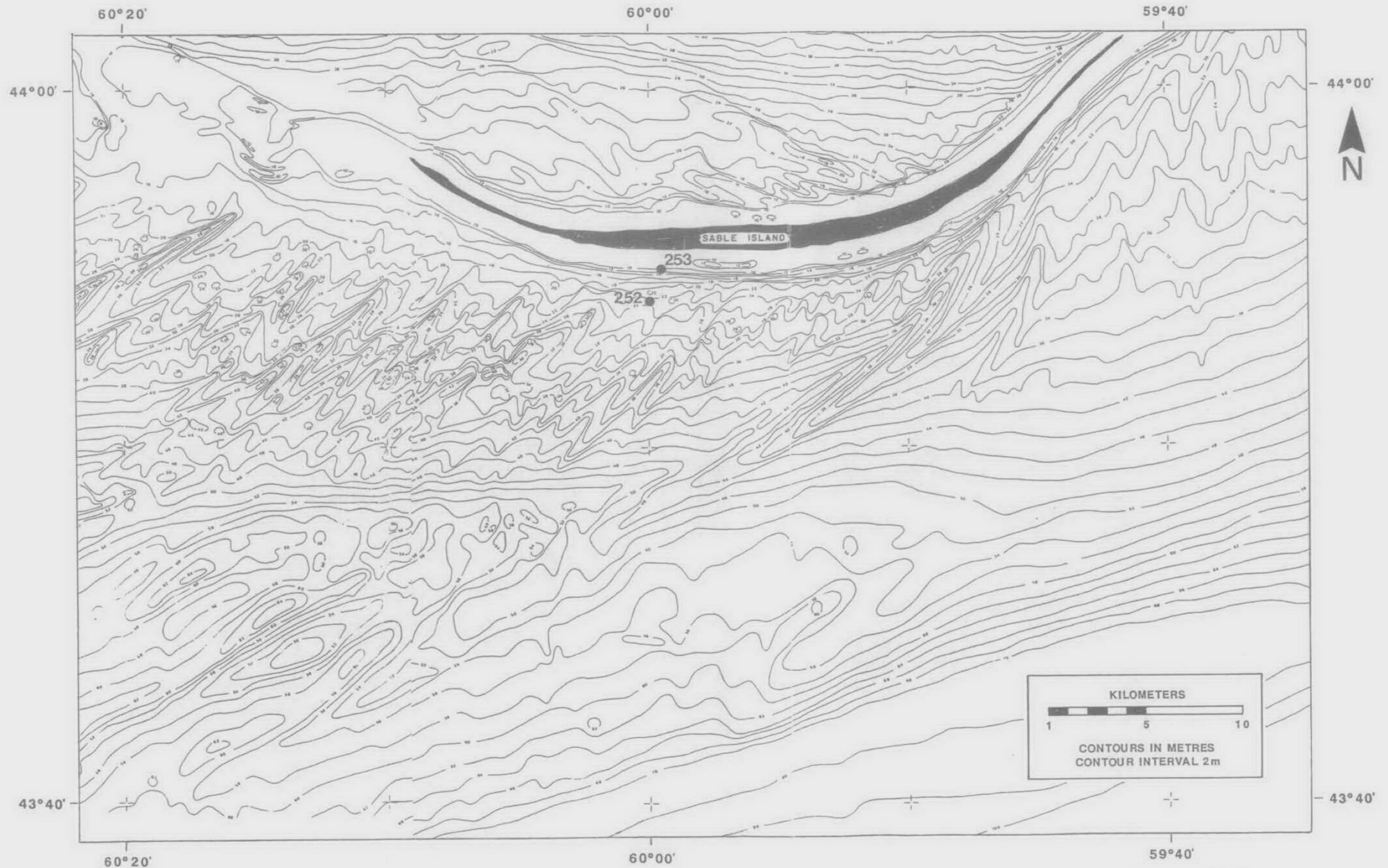
(a) Instrumentation

The two nondirectional wave buoys at Station 251 and 133 were standard 0.7 m diameter Datawell Waveriders. The WRIPS buoy was modified by L. Admo for satellite transmission and data were acquired from it for approximately nine days. This buoy was lost on December 28, 1984 when it was struck by a seismic streamer towed behind the M.V. Western Arctic, and the buoy was presumably sunk.

The directional data were collected with identical WAVEC heave-pitch-roll buoys manufactured by Datawell b.v. of the Netherlands. A schematic of the buoy is shown in Fig. 2.6 together with one of the buoys during deployment. A conventional mooring as specified by Datawell was used. Instrument specifications are given in Table 2.2.

For this experiment a receiving antenna was mounted on the West Light on Sable Island, and wired to the Direc receivers located in a weatherproof hut near the light tower. Data were recorded on cartridge tapes using a Columbia 300-D data recorder. Each cartridge had a capacity of about 8 days but servicing was carried out every 6 or 7 days. No continuous data were recorded during storms (except at station 133).

Wind data were obtained during the measurement period from the U2A anemometer maintained by the Atmospheric Environment Service at the Sable Island Weather Station. The anemometer was mounted on a mast



Data Source: C.H.S. Field Sheets  
4992 and 4993. Survey year: 1982

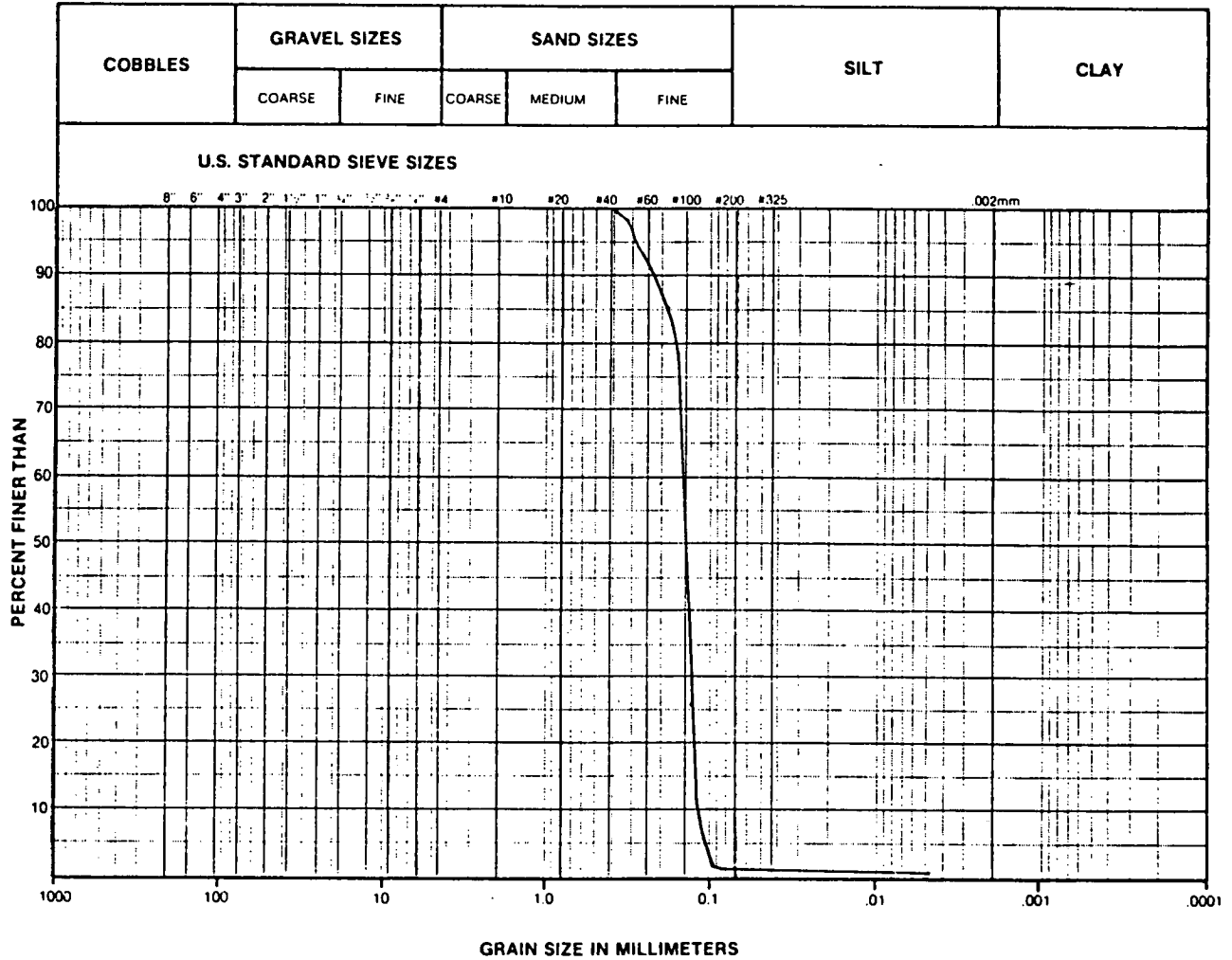
Fig. 2.4 Detailed bathymetry in the region of shallow water wave measurements.



*Seaconsult* Marine Research Ltd.

**GRAIN SIZE CURVE**

CLIENT:	
PROJECT NUMBER:	
LAB. NUMBER:	
LOCATION: Grab #12 Venture	
HOLE:	SAMPLE:
DEPTH:	
TECHNICIAN:	DATE:



REMARKS:  $D_{50} = 0.15 \text{ mm}$  ,  $D_{90} = 0.23 \text{ mm}$

---



---



---



---

NOTE UNIFIED SOIL CLASSIFICATION SYSTEM

SUMMARY	
$D_{10} =$ _____ mm	GRAVEL <u>0.20</u> %
$D_{30} =$ _____ mm	SAND <u>98.70</u> %
$D_{60} =$ _____ mm	SILT <u>0.55</u> %
$C_u =$ _____ mm	CLAY <u>0.55</u> %
$C_c =$ _____ mm	

Fig. 2.5 Representative grain size distribution for fine sands on the southeast flank of Sable Island in 30 m depth. (Source: Hodgins et al., 1986).



Fig. 2.6 Schematic diagram of the WAVEC buoy (a) and a photograph of the buoy during deployment (b).

**Table 2.2**  
**Directional Wave Data Instrument**  
**and Sampling Specification**

---

Instrument Type:	Datawell WAVEC buoy (heave-pitch-roll)
Overall Diameter:	2.5 m
Overall Height:	1.7 m
Gross Weight:	704 kg
Heave/Pitch/Roll Sensor:	Hippy 120
Frequency Range:	0.0333 to 1.0 Hz
Accuracy:	<2% of measured value
Sampling Rate:	1 Hz
No. of Samples/Burst	2048
Burst Interval:	3 hr

Buoys were not calibrated prior to or after deployment for this study.

13.4 m above MSL. The wind speed and direction represent one-minute average values recorded on the hour.

(b) Data Processing

The directional data have been processed using the conventional analysis (Long, 1980; Hasselmann et al., 1980). In this method, the directional spectrum  $S(f, \theta)$  is defined by the one-dimension energy spectrum  $E(f)$  multiplied by an angular spreading function; i.e.

$$S(f, \theta) = E(f) \cdot G(f, \theta) \quad (2.1)$$

where

$$G(f, \theta) = K(f) \cos^{2s(f)} \frac{1}{2} \left\{ \theta - \theta_0(f) \right\} \quad (2.2)$$

and  $K(f)$  is chosen such that

$$\int_0^{2\pi} G(f, \theta) d\theta = 1 \quad (2.3)$$

is satisfied. The parameters defining this spreading model are  $\theta_0$ , the mean wave direction, and  $s$ , the spreading exponent, each a function of frequency,  $f$ .

To evaluate  $(\theta_0, s)$  four data equations are defined as follows

$$\underline{d} = \int_0^{2\pi} G(\theta) \underline{b}(\theta) d\theta \quad (2.4)$$

where  $\underline{x} = [C_{11}, C_{22}, C_{33}, Q_{12}, Q_{13}, C_{23}]^T$  (2.5)

$$\underline{d}(\underline{x}) = \begin{bmatrix} Q_{12}/[C_{11}(C_{22} + C_{33})]^{1/2} \\ Q_{13}/[C_{11}(C_{22} + C_{33})]^{1/2} \\ (C_{22} - C_{33})/(C_{22} + C_{33}) \\ 2C_{23}/(C_{22} + C_{33}) \end{bmatrix} \quad (2.6)$$

$$\underline{b}(\theta) = [\cos \theta, \sin \theta, \cos 2\theta, \sin 2\theta]^T \quad (2.7)$$

and the subscripts 1, 2, 3 denote heave, NS slope, and EW slope respectively.  $C_{ij}$  and  $Q_{ij}$  specify the cospectrum and quadrature spectrum

respectively.

These cross-spectral estimates are subject to statistical variability; hence, in general

$$\begin{aligned} \underline{x} &= \hat{\underline{x}} - \delta\hat{\underline{x}} \\ \underline{d} &= \hat{\underline{d}} - \delta\hat{\underline{d}} \end{aligned}$$

where the carat indicates a particular realization of a random variable. Substituting (2.2) for G in (2.4) and integrating over  $\theta$  yields

$$\begin{aligned} \begin{bmatrix} \hat{d}_1 - \delta\hat{d}_1 \\ \hat{d}_2 - \delta\hat{d}_2 \end{bmatrix} &= \frac{s}{s+1} \begin{bmatrix} \cos \theta_0 \\ \sin \theta_0 \end{bmatrix} \\ \begin{bmatrix} \hat{d}_3 - \delta\hat{d}_3 \\ \hat{d}_4 - \delta\hat{d}_4 \end{bmatrix} &= \frac{s(s-1)}{(s+1)(s+2)} \begin{bmatrix} \cos 2\theta_0 \\ \sin 2\theta_0 \end{bmatrix} \end{aligned} \quad (2.8)$$

Invoking the assumption that  $\delta\hat{d}_1 = \delta\hat{d}_2 = 0$  (Long, 1980), yields one estimate of  $\theta_0$  and s, i.e.

$$\begin{aligned} \theta_0 &= \arctan (d_2/d_1) - 21.5^\circ \\ s &= D_1/[1-D_1] \end{aligned} \quad (2.9)$$

where  $D_1 = [\hat{d}_1^2 + \hat{d}_2^2]^{1/2}$ . We note that an alternative pair of estimates for  $(\theta_0, s)$  may be obtained by setting  $\delta\hat{d}_3 = \delta\hat{d}_4 = 0$  and solving the second pair of (2.8). There is no a priori basis to choose between the two estimates of  $(\theta_0, s)$  and we retain only the first given by (2.9).

The above method is incorporated into the program SEAWAV-A<sup>m</sup> implemented by Seaconsult for directional wave data analysis. The cross-spectra were computed using the following procedures for each time-series  $X_{ik}$ , with  $i = 1, 2, 3$  corresponding to the measurements denoted above, and  $k = 1, 2, \dots, N$  where N is the number of sample points:

- (1) the series means were calculated and a zero-mean series was formed as

$$X_{ik} = X_{ik} - \bar{X}_i$$

with variances  $\sigma_i^2$  evaluated from

$$\sigma_i^2 = \left\{ \sum_{k=1}^N x_{ik}^2 - N\bar{x}_i^2 \right\} / (N-1);$$

- (2) each series was zero-padded to length  $2N$ , and the FFT  $\hat{X}_i$  calculated for  $i=1,2,3$ ;
- (3) the convolution series  $\hat{C}_{ijk}$ ;  $i, j = 1,2,3, k = 1,2,\dots,N+1$  was formed

$$\hat{C}_{ijk} \leftarrow \hat{X}_{ik}^* \hat{X}_{jk}$$

where the \* denotes the complex conjugate, and an inverse FFT of  $\hat{C}_{ijk}$  was taken to yield the covariance estimates  $C_{ij}$ , i.e.

$$C_{ijk} \leftarrow \text{FFT}^{-1}(\hat{C}_{ijk})/N;$$

- 4) estimates of  $C_{ijk}$  were then passed through a Bartlett window of width  $M$  to give the smoothed covariance estimates  $C_{ijk}$ , i.e.

$$C_{ijk} = \begin{cases} (1 - (k - 1)/M) C_{ijk}, & k = 1, \dots, M \\ 0 & k = M+1, \dots, 2N-M+1 \\ (1 - (2N + 1 - k)/M) C_{ijk}, & k = 2N-M+2, \dots, 2N \end{cases}$$

For this filtering procedure the number of degrees of freedom  $\nu$  is given by

$$\nu = 2N\Delta b \tag{2.10}$$

where  $b$  is the desired bandwidth, and  $\Delta$  is the sampling interval. In the Bartlett window  $M$  is related to the bandwidth by

$$M = b_0/b\Delta$$

where  $b_0 = 1.5$ . For the Sable Island spectra  $N = 2048, \Delta = 1$  s and  $b$  was chosen to be 0.0150 Hz, giving  $\nu = 61$  degrees of freedom. The variance spectrum  $E(f)$  was found from the autospectrum of the heave, i.e.

$$E(f) = C_{11} / (2\pi f)^4 \tag{2.11}$$

Finally,  $E(f)$  was corrected using the buoy transfer coefficient published by Datawell. This completes the specification of  $S(f, \theta)$  given by (2.1).

## 2.2 Basic Results

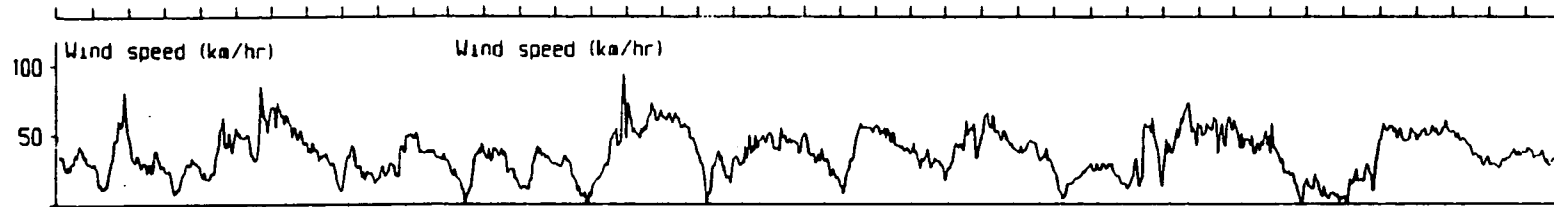
Time-series of wind speed, wind and wave direction, significant wave height, and spectral peak period are shown for the 1984-85 field program in Fig. 2.7 for the two shallow water sites. Throughout this report significant wave height is defined as

$$H_S = H_{m_0} = 4 \left\{ \int_0^\infty \int_0^{2\pi} S(f, \theta) d\theta df \right\}^{1/2} \quad (2.12)$$

The deep water time-series for stations 133 and 251 are shown in Fig. 2.8. For reference to shallow water the station 252 measurements are also plotted in this graph for the December 25-28th storm.

Four reasonably distinct storms were well-monitored in both deep and shallow water; they are, together with the wind character:

Storm Dates	Winds
December 25-28, 1984 ... (Stns. 133, 251, 252 253)	Initially 15-18 m/s onshore, shifting rapidly to westnorthwesterly winds peaking at 24 m/s and holding fairly steady in direction at 15 to 20 m/s for the following 12 hours.
January 5-8, 1985 ..... (Stns. 133, 253)	Steadily turning winds from east through south to westerly directions over 18 hours with winds building to 25 m/s, then holding steady from the west at speeds averaging 18 m/s for a further 36 to 40 hours.
January 15-18, 1985 .... (Stns. 133, 253)	Initially from south to southeast building over 18 hours to 15 m/s, shifting rapidly to the west and rebuilding to 18 m/s and then falling steadily to 5 m/s over 44 hours from the west.
January 20-24, 1985 .... (Stns. 133, 253)	Initially from the southwest building rapidly to 16-18 m/s, followed by a sharp decline to less than 5 m/s out of the south east and then rapidly rebuilding to 15 to 22 m/s steady from the southwest for 48 hours thereafter falling steadily for another 24 hours accompanied by a



Station 252

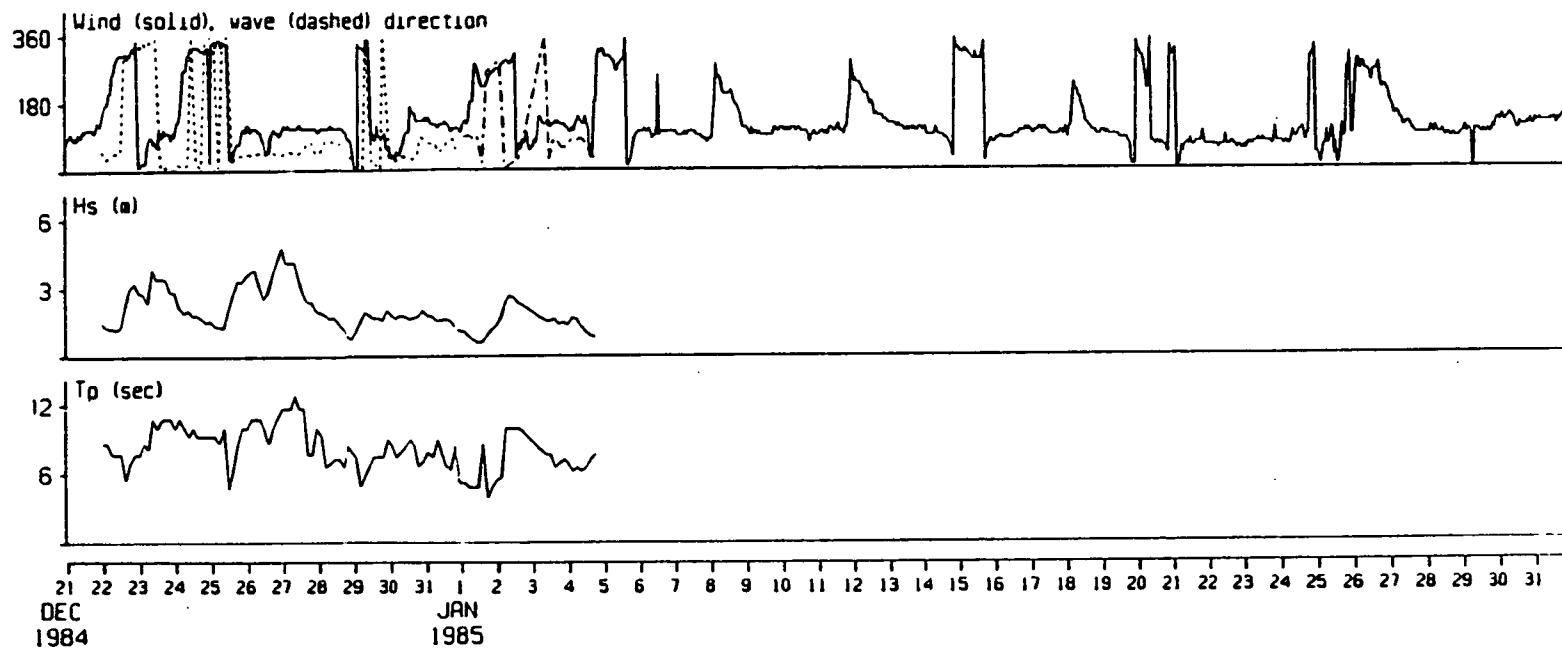
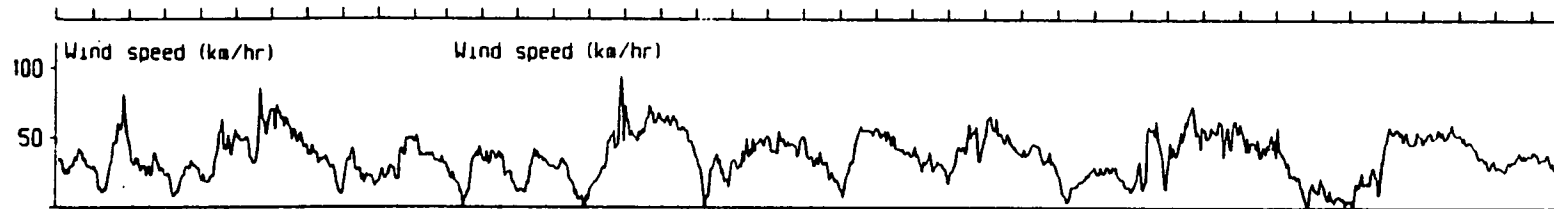


Fig. 2.7 (a) Time-series of wind speed, wind and wave directions (given as direction towards which winds are blowing and waves are propagating), significant wave height and peak period for the 1984-85 directional wave measurement program at station 252.





Station 253

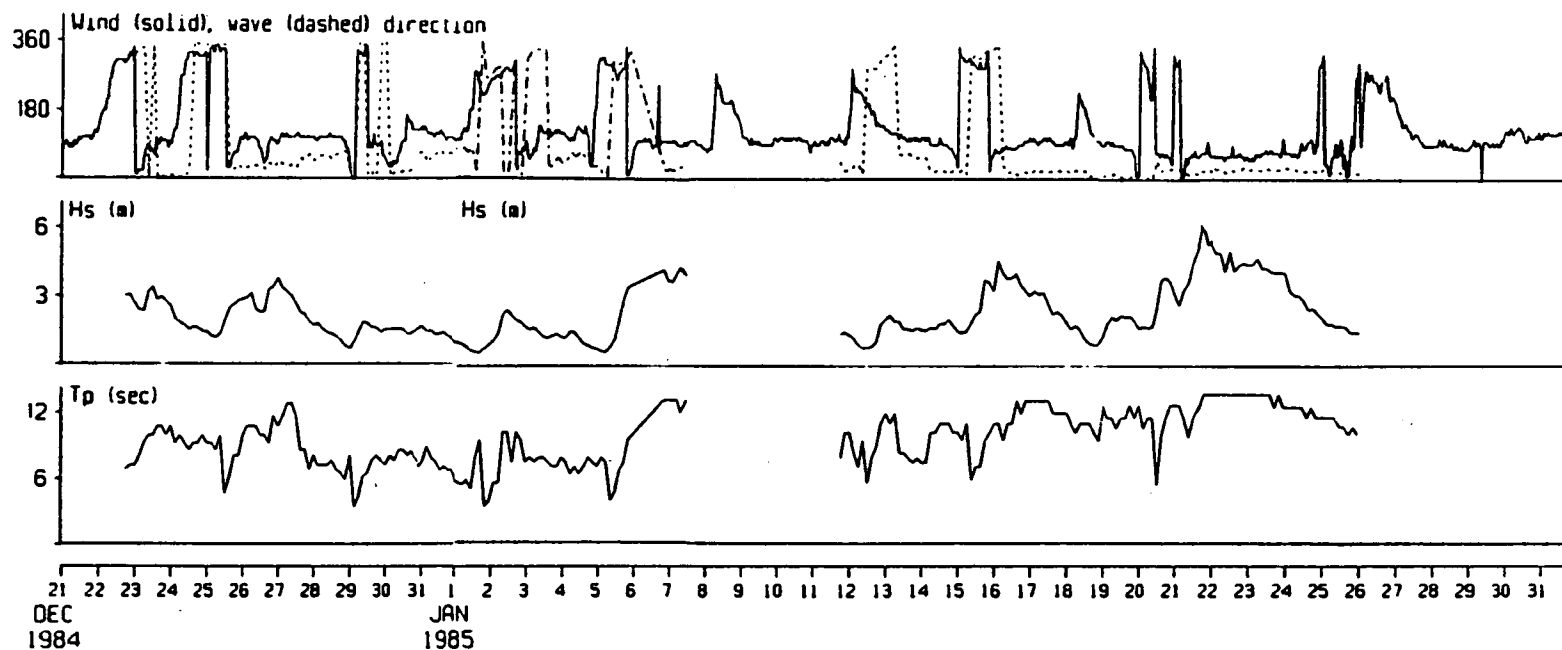


Fig. 2.7 (b) Time-series of wind speed, wind and wave directions (given as direction towards which winds are blowing and waves are propagating), significant wave height and peak period for the 1984-85 directional wave measurement program at station 253.

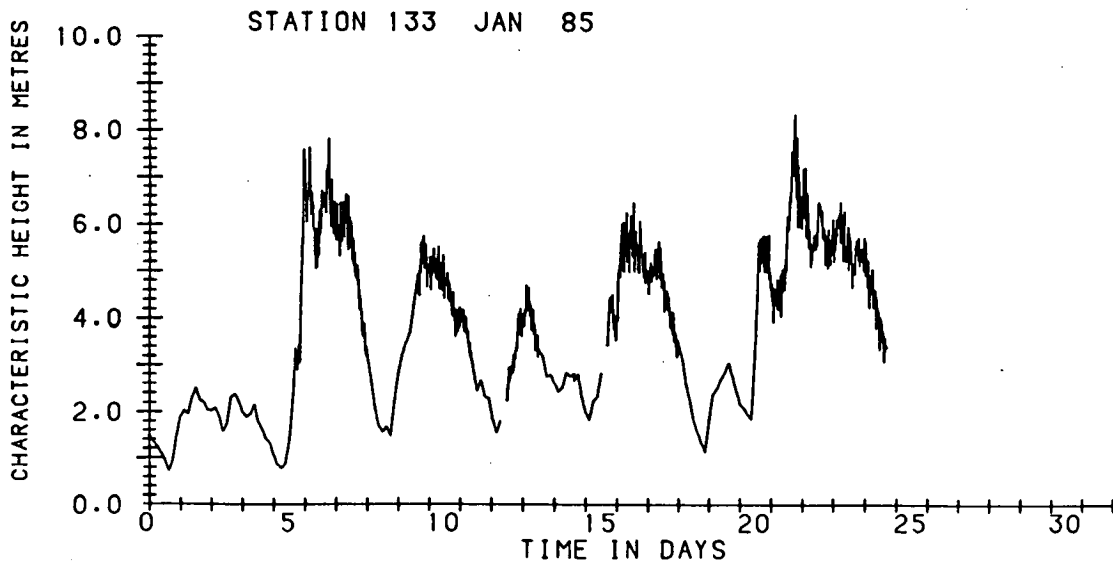
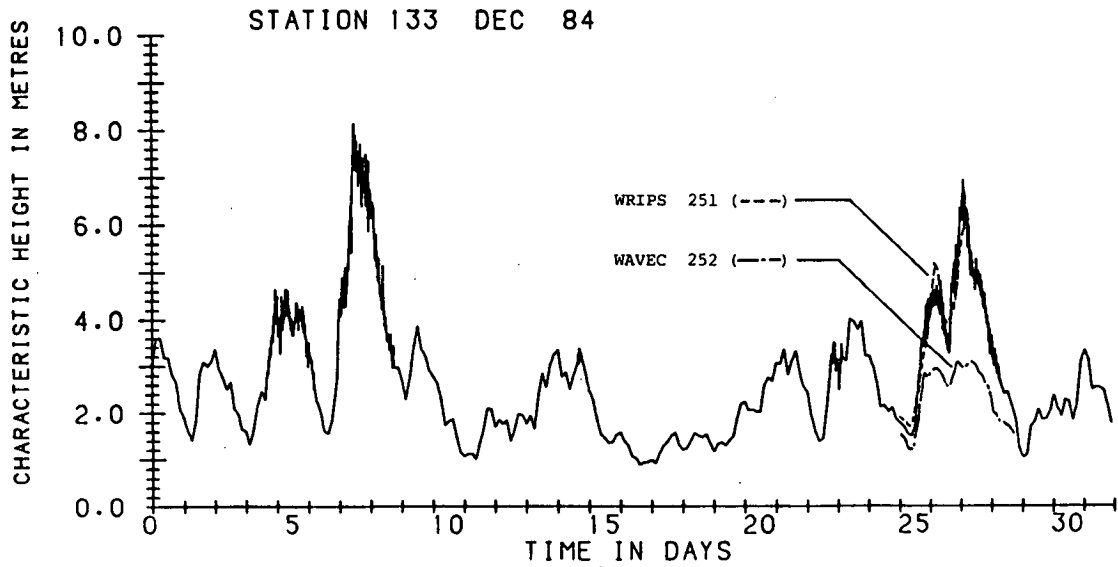


Fig. 2.8 Time-series of significant wave height measured at stations 133 and 251 in conjunction with the 1984-85 field program. A portion of the station 252 record in the December 26-28 storm is shown for comparison of deep and shallow water wave conditions.

slow shift to the west.

In each of these storms peak significant wave heights exceeded 3.8 m with peak periods in the 12 to 14 s range.

The directional data for these four storms are plotted in Fig. 2.9 so as to show the spectral energy density and mean wave direction in 20 frequency bands together with the wind vector and significant wave height. Concurrent data for stations 252 (h = 22 m) and 253 (h = 12 m) are shown in the first pair of graphs. It can be seen here that during the early part of the storm on December 25 wave directions were closely coupled to the onshore wind direction and do not differ greatly from the deeper to shallower site. As the wind shifts the high frequency energy turns with wind but the lower frequency, energetic part of the spectrum maintains a strong southwesterly direction. After 21:00Z on December 25 the effects of refraction show up in a directional shift varying from about 5 to 30 degrees counterclockwise for periods greater than 6 s. This shift brings the wave crests more nearly parallel to the bottom contours and shoreline as waves propagate from site 252 into the shallow water at 253.

The same trends are evident in the other three storms also. For onshore winds there is a close directional coupling between winds and waves at all frequencies and separate refraction effects are not clearly discernible. For winds at an angle to the bottom contours, or blowing parallel to them, low frequency wave directions appear governed by incident wave directions in deeper water, and by refraction.

There are two interesting points to note: First, the data on January 15 and 16, 1985 show that for turning winds (here from SE to SW) a lag of several hours is evident in waves with 11 to 15 s periods before alignment with the local wind is achieved; that is, there appears to be quite a long relaxation time before the longer waves achieve a directional equilibrium with the steady wind conditions following 00:00Z on January 16. A lag time of the magnitude shown here, about 12 hours at 11 s, is most likely a complicated function of the swell propagating ashore that was generated by the SE storm winds well out to sea, and of

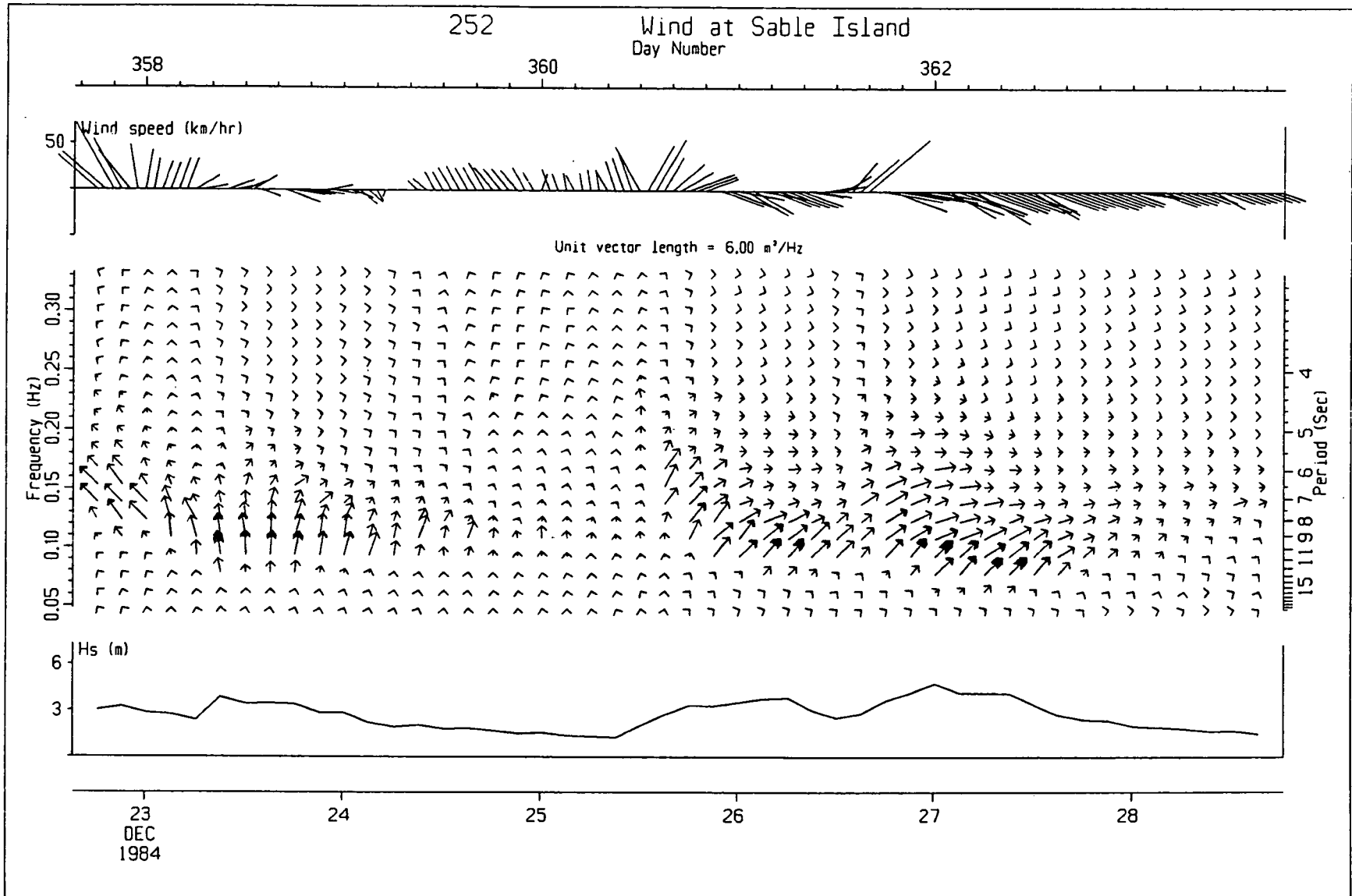


Fig. 2.9(a) Directional wave spectra from station 252 (22 m water depth) in 20 frequency bands plotted against the Sable Island measured wind and significant wave height, December 23-28, 1984.

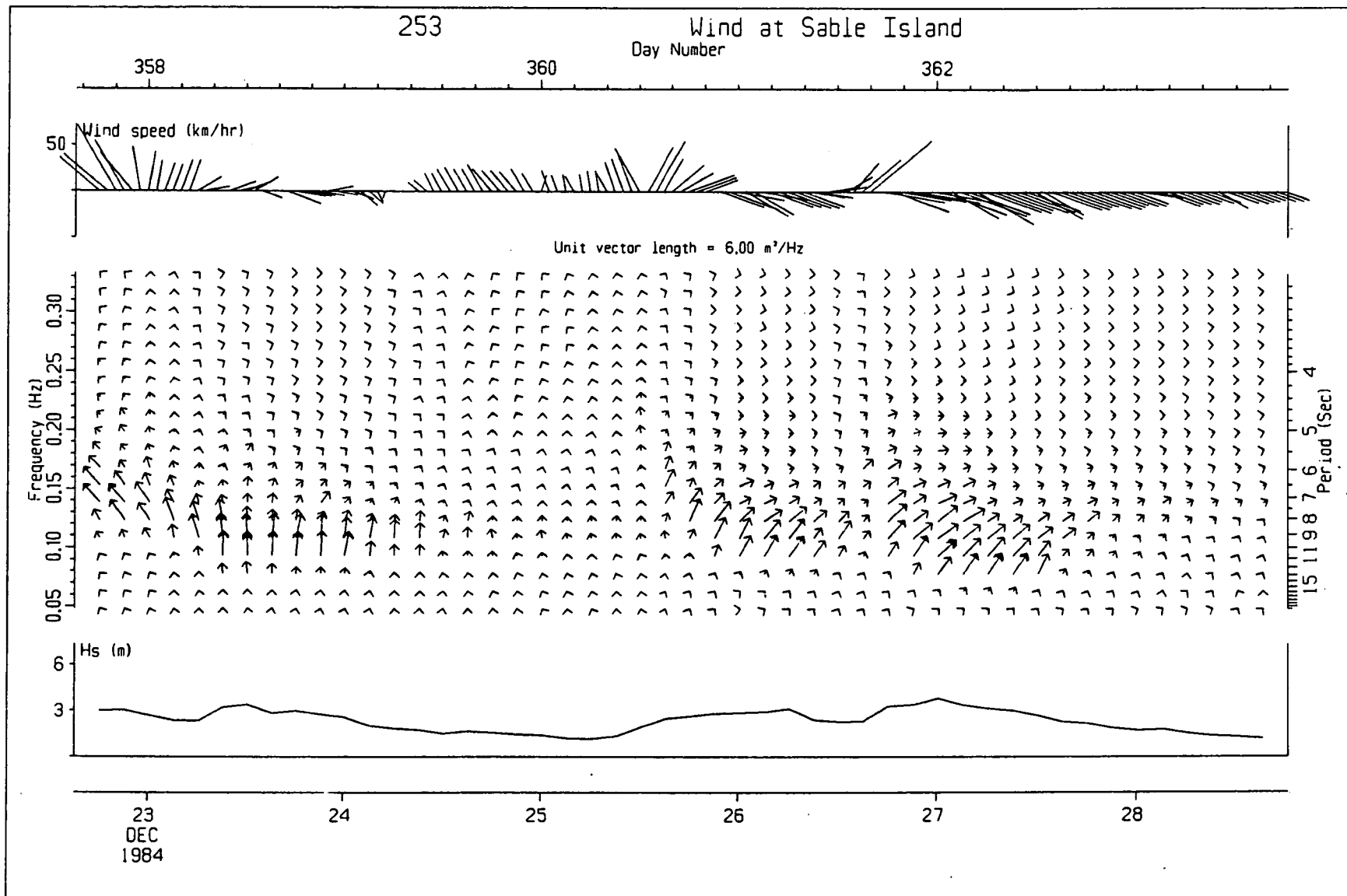


Fig. 2.9(b) Directional wave spectra from station 253 (12 m water depth) in 20 frequency bands plotted against the Sable Island measured wind and significant wave height, December 23-28, 1984.

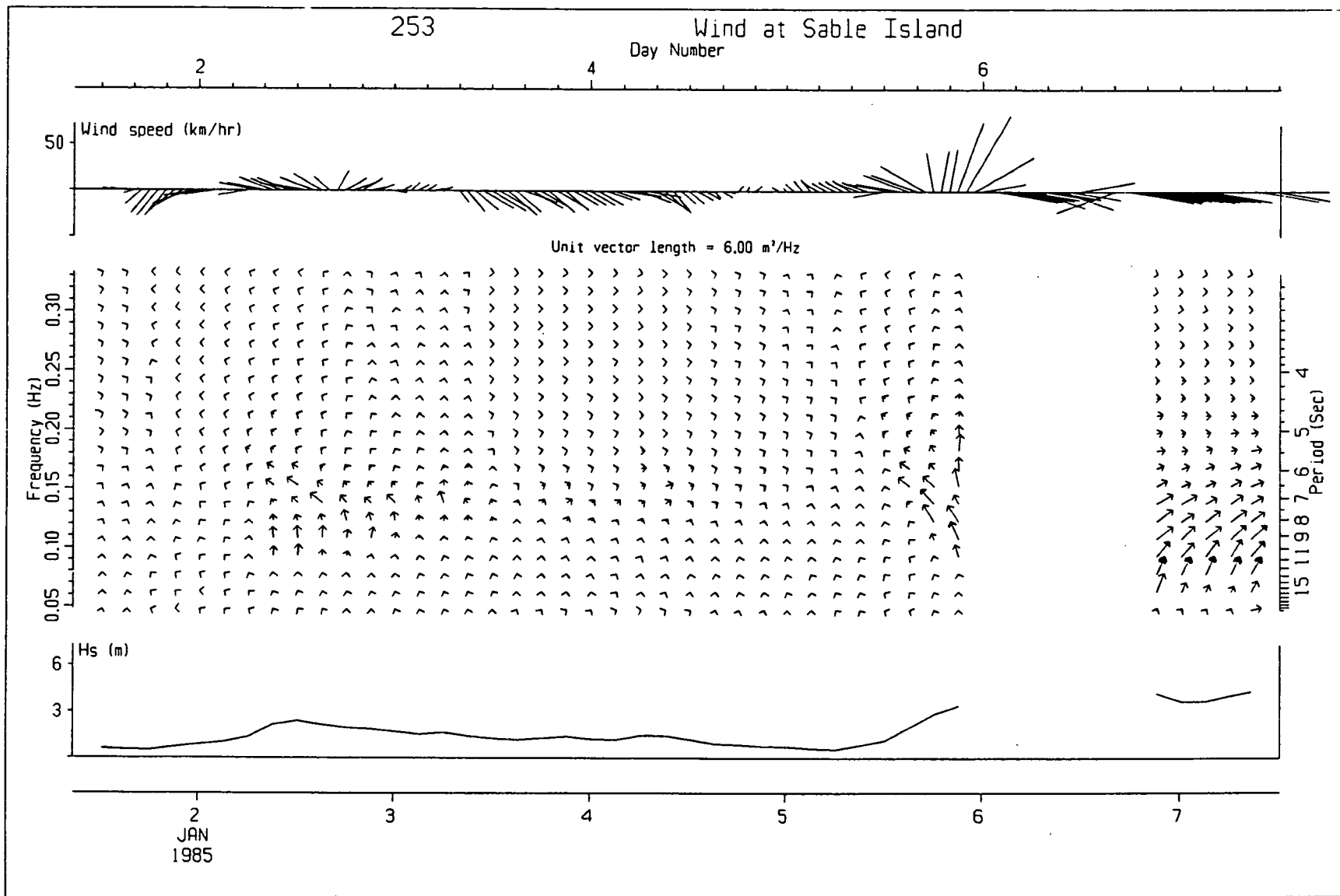


Fig. 2.9(c) Directional wave spectra from station 253 (12 m water depth) in 20 frequency bands plotted against the Sable Island measured wind and significant wave height, January 2-7, 1985.

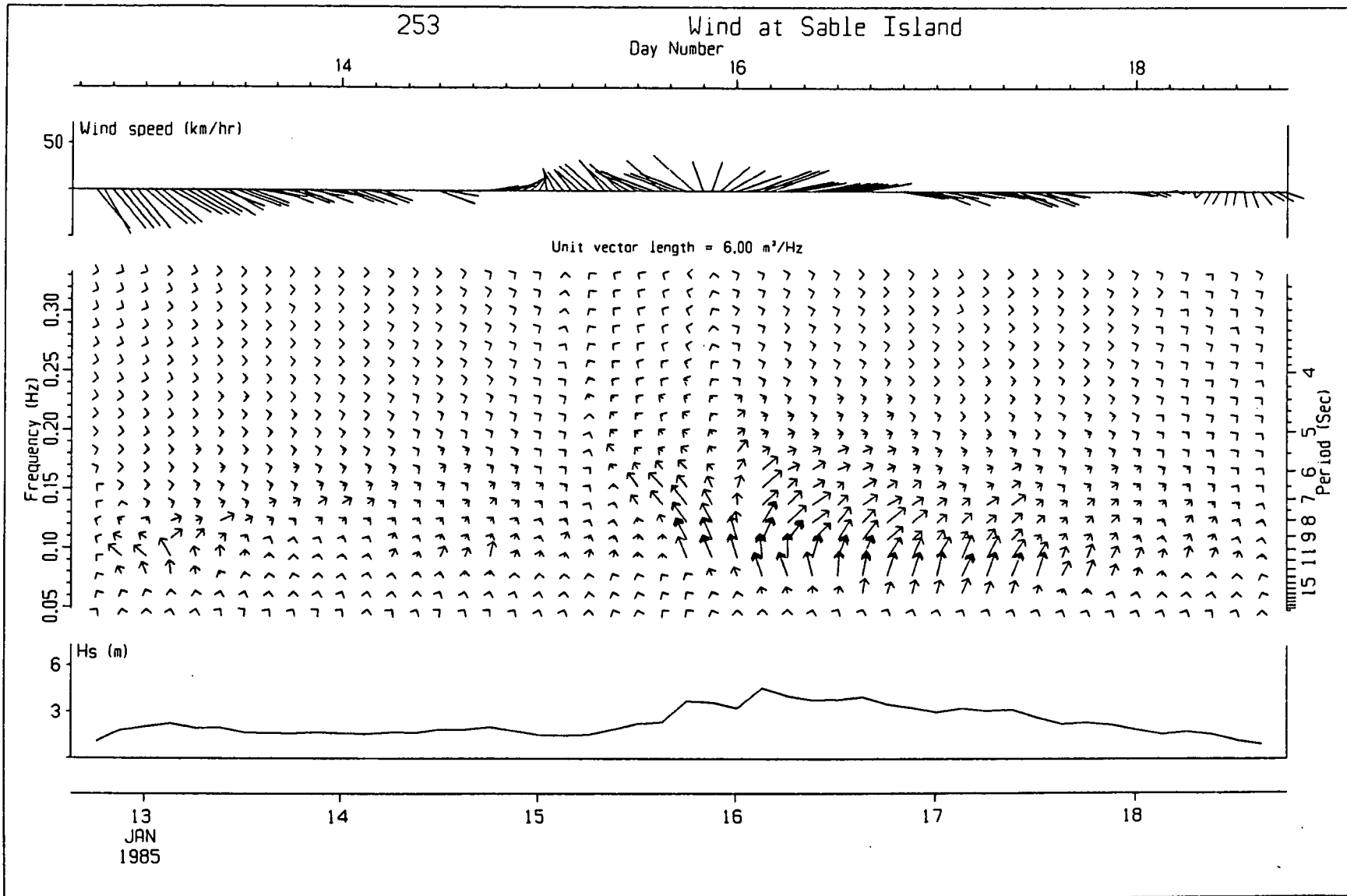


Fig. 2.9(d) Directional wave spectra from station 253 (12 m water depth) in 20 frequency bands plotted against the Sable Island measured wind and significant wave height, January 13-18, 1985.

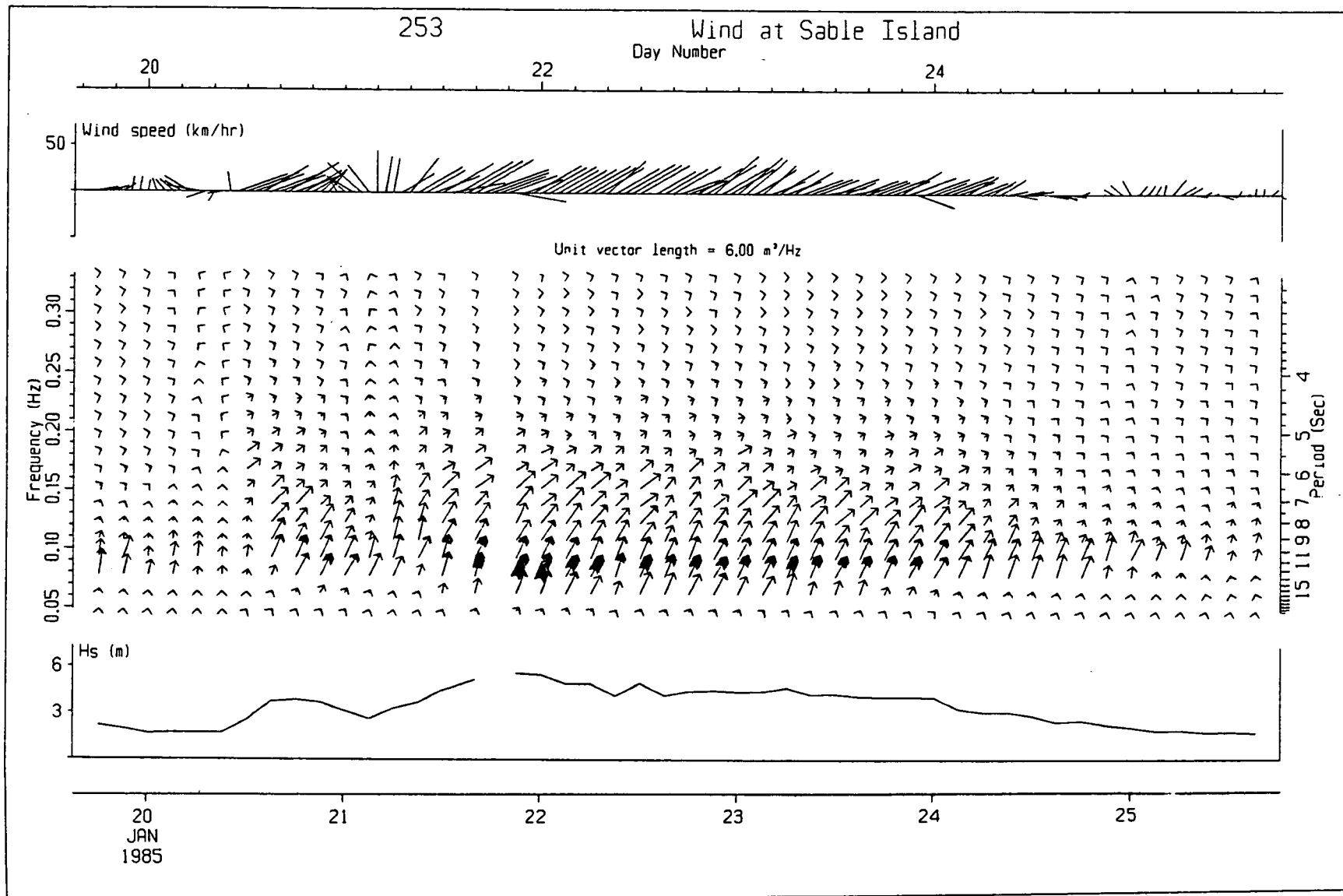


Fig. 2.9(e) Directional wave spectra from station 253 (12 m water depth) in 20 frequency bands plotted against the Sable Island measured wind and significant wave height, January 20-25, 1985.



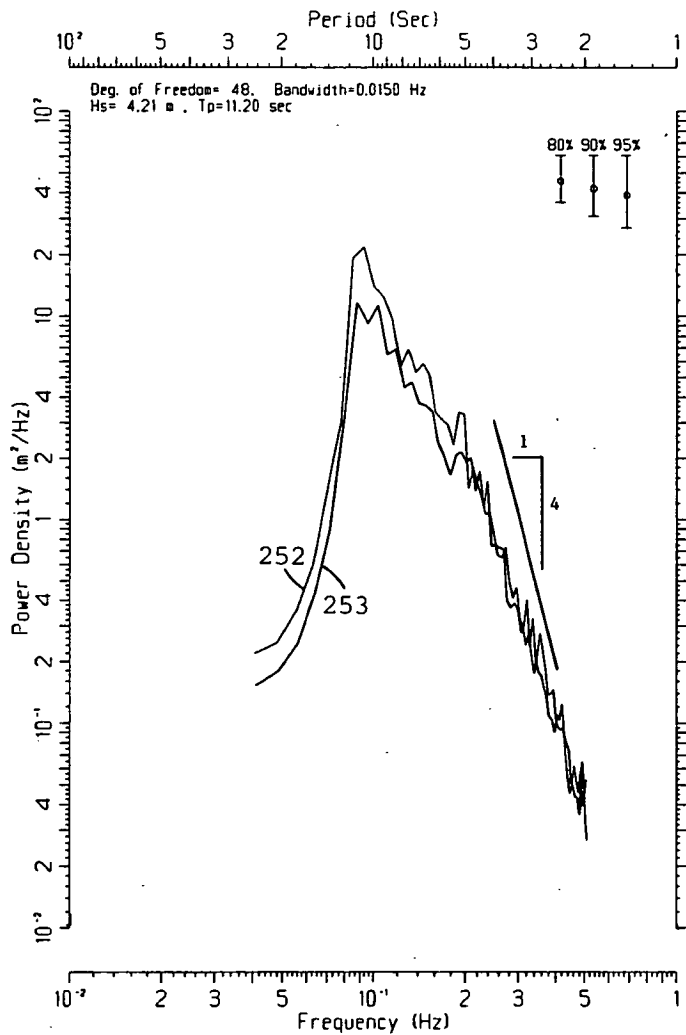
local growth on the forward face of the spectrum.

Second, the data for January 22 and 23, 1985 show that despite the very steady southwesterly winds, wave directions were consistently up to 45 degrees off the wind in the energetic part of the spectrum, rotated in the direction consistent with refraction. Thus, for this storm refraction is expected to be an important factor governing the nearshore conditions.

Two coincident spectra near the peak of the December 25-27th storm are shown in Fig. 2.10. In each case the sample spectrum from station 253 is superimposed on that from station 252 to show the reduction in energy density. It will be noticed from Fig. 2.4 that the separation distance of the two buoys is approximately 2200 m. In terms of the shallow water group velocity for 11-s waves, the travel time between the two gauges is about 3 minutes, i.e. less than 10% of the sample record length at each time of measurement (34 minutes). Thus it is valid to compare the spectra in this manner. Moreover, as can be seen in Fig. 2.9 the wave directions for 10, 11 and 12-s wave energy are very nearly aligned at these times. As a result, for all practical purposes, the wave energy crossing station 252 reaches 253 about 3 minutes later for the energetic part of the spectrum. Reductions in energy levels are due to nonlinear fluxes to the dissipation range and the forward face, and to bottom interactions. Given the sand sea bed, these latter processes, if important, are expected to be related mostly to friction.

The two sets of spectra show similar results. The greatest decrease in energy is at and to the right of the spectral peak  $f_m$ . The rear face of each pair shows an equilibrium range with about a 1:4 slope in a range of periods from about 6 down to 2.5 s. The spectra at 21:00Z on December 26 show an almost negligible forward face loss of energy in a narrow frequency band just to the left of  $f_m$  but some statistically significant losses at the lowest frequencies (periods from 16 to 27 s). As can be seen in Fig. 2.10, the same low frequencies show a loss of energy from sites 252 to 253. There is also a small loss of energy over the entire forward face, but we note that  $f_m$  differs by 0.0077 Hz and the forward

252-3 (MEDS) at 21:00:00 12-26-84



252-3 (MEDS) at 00:00:00 12-27-84

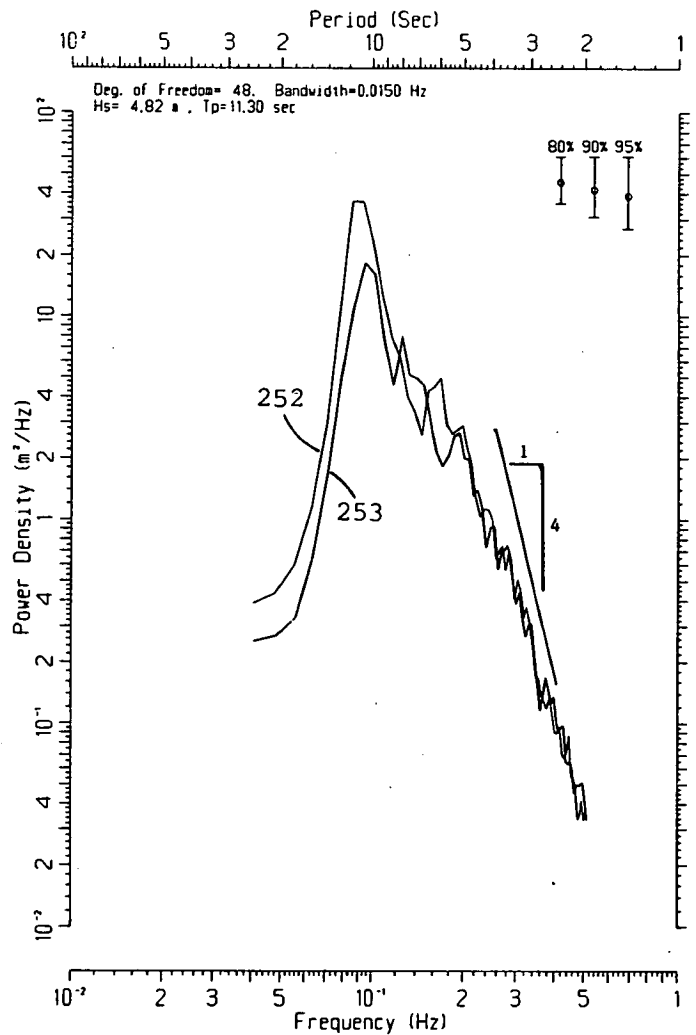


Fig. 2.10 Sample spectra from sites 252 and 253 at 84-12-26-21Z and 84-12-27-00Z.

face of the spectrum from gauge 252 could be slightly shifted to higher frequencies, thus accounting for the lower energies just to the left of the peak frequency. Such differences are more likely due to sampling variability than to the wave transformation phenomena described above.

### 3.0 WAVE PREDICTION INTERCOMPARISON

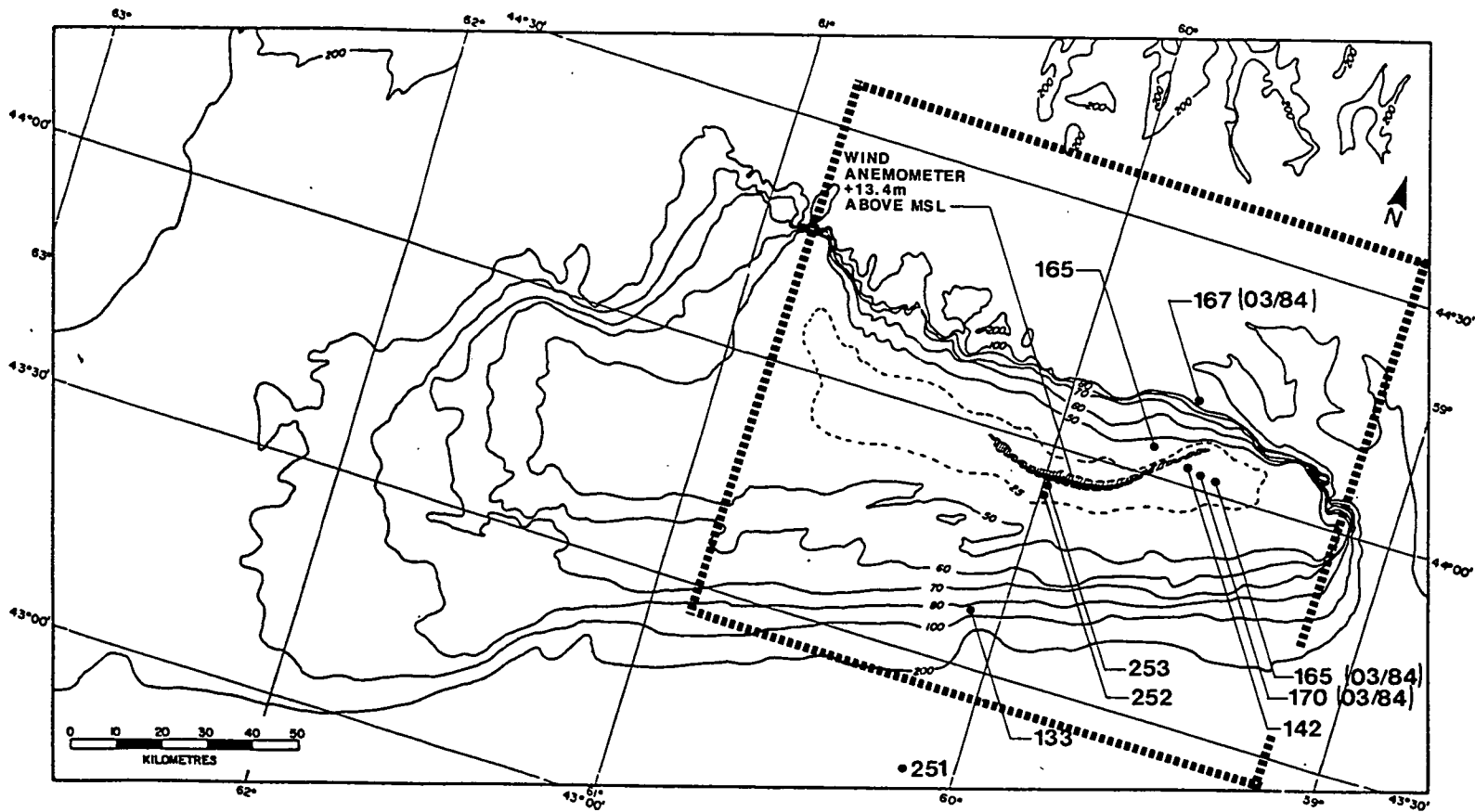
#### 3.1 Methods

Application of the two models on Sable Island Bank was designed to show the practical differences between each formulation in terms of wave height  $H_s$ , peak period  $T_p$ , mean wave direction  $\bar{\theta}$ , and spectral shape. Four storms were selected, each with different wind characteristics, and within the limitations of available directional wave data, different incident deep water wave directions. The storms are discussed more fully in the next section.

The area defined for shallow water transformation calculations is shown in Fig. 3.1 together with the locations of measured wave spectra. Deep water directional frequency spectra were hindcast for the four storms over the area shown in Fig. 3.2. The inner boundary of the intermediate nested grid exactly matched the boundary of the shallow water domain. Deep water spectra along this boundary were calculated with WAVAD using wind fields derived every 6 hours from surface weather charts. The wind fields were defined on a  $1^\circ \times 1^\circ$  latitude-longitude grid using a planetary boundary layer model to reduce gradient winds calculated from the surface pressure gradients to 10 m. A kinematic wind analysis was carried out for the area surrounding Sable Island, and the kinematic winds were blended with objective winds derived from the pressure fields to yield the final input wind field for hindcasting. Typical solutions for the wave height and direction fields at 06 GMT on December 26, 1984 are shown in Fig. 3.3.

There were no wave measurements on the deep-to-shallow water boundary with which to verify the deep water boundary conditions, and there were no wind measurements, independent of the database used to derive the input winds, for verification of the wind fields. However, wave measurements at stations 133 and 167 (Fig. 3.1) were located in deep water inside the shallow water domain and have been used to comment on the accuracy of the hindcast boundary data where possible.

Each model was applied to the shallow water domain using identical deep water boundary conditions and overwater wind fields. In addition, the



■■■■■■■■ shallow water domain

Fig. 3.1 Shallow water modelling domain on Sable Island Bank.

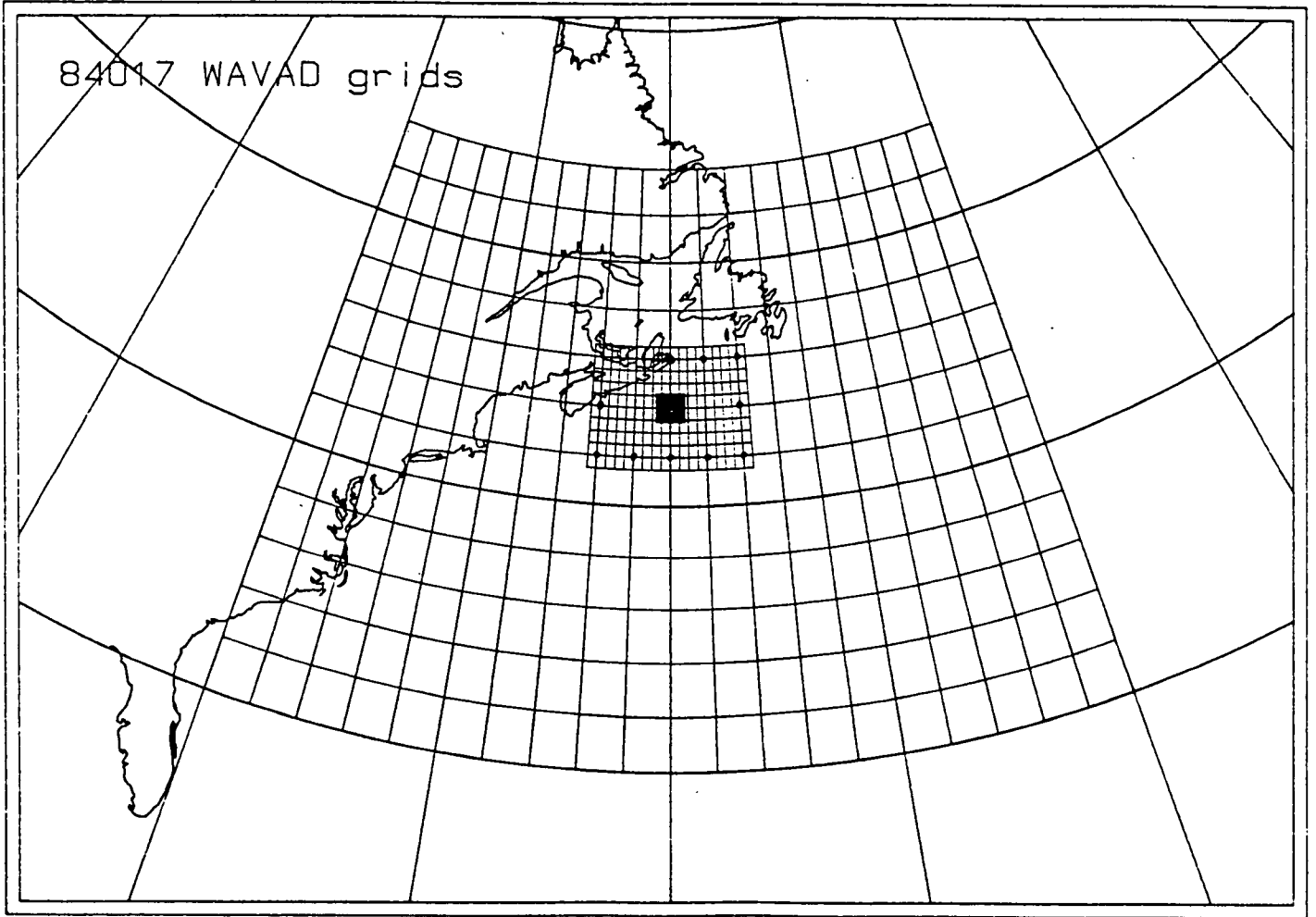


Fig. 3.2 Deep water wave modelling grids used with WAVAD.

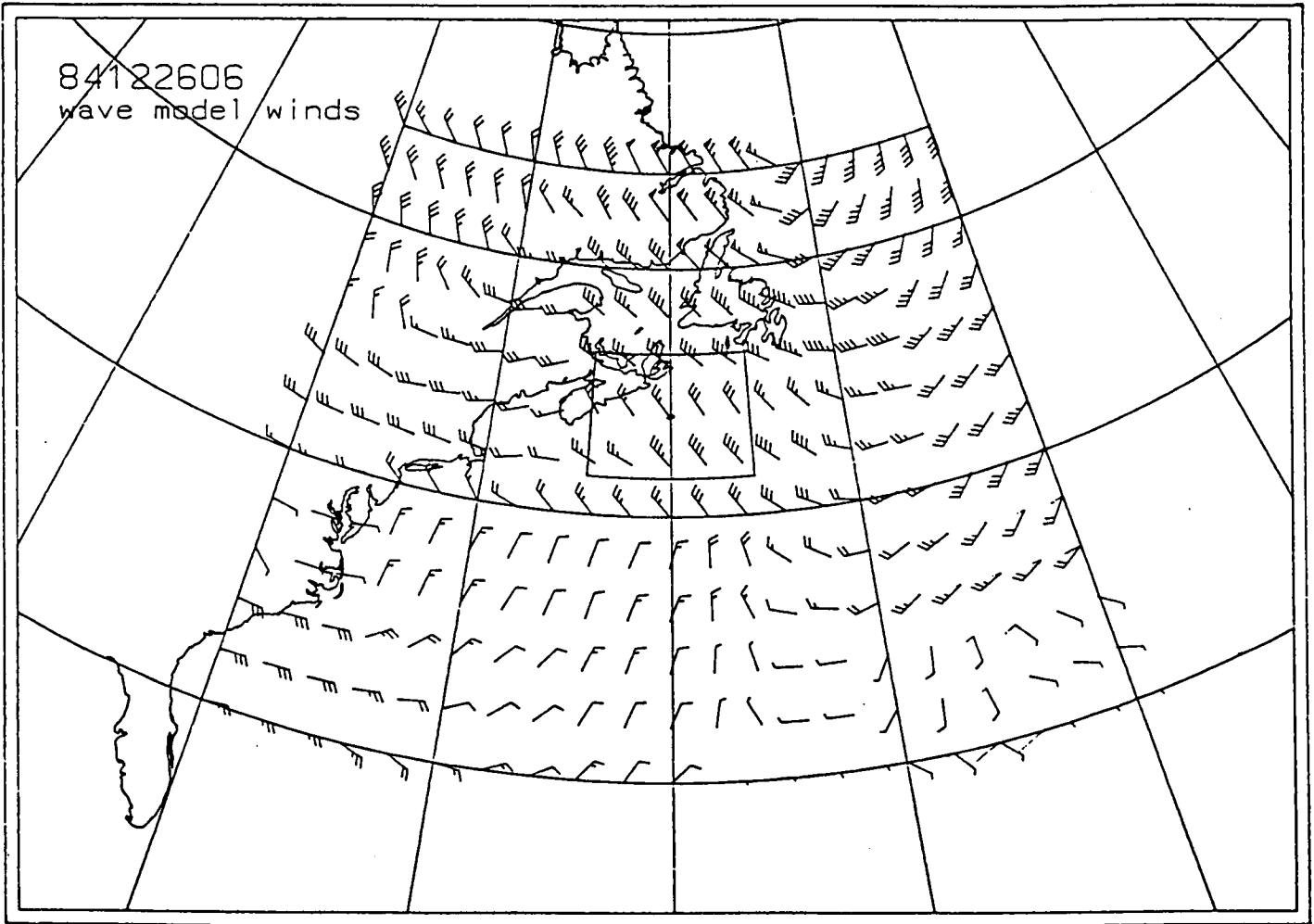


Fig 3.3(a) Wind field and deep water coarse grid wave height and direction fields at 06 GMT on December 26, 1984 calculated with WAVAD.

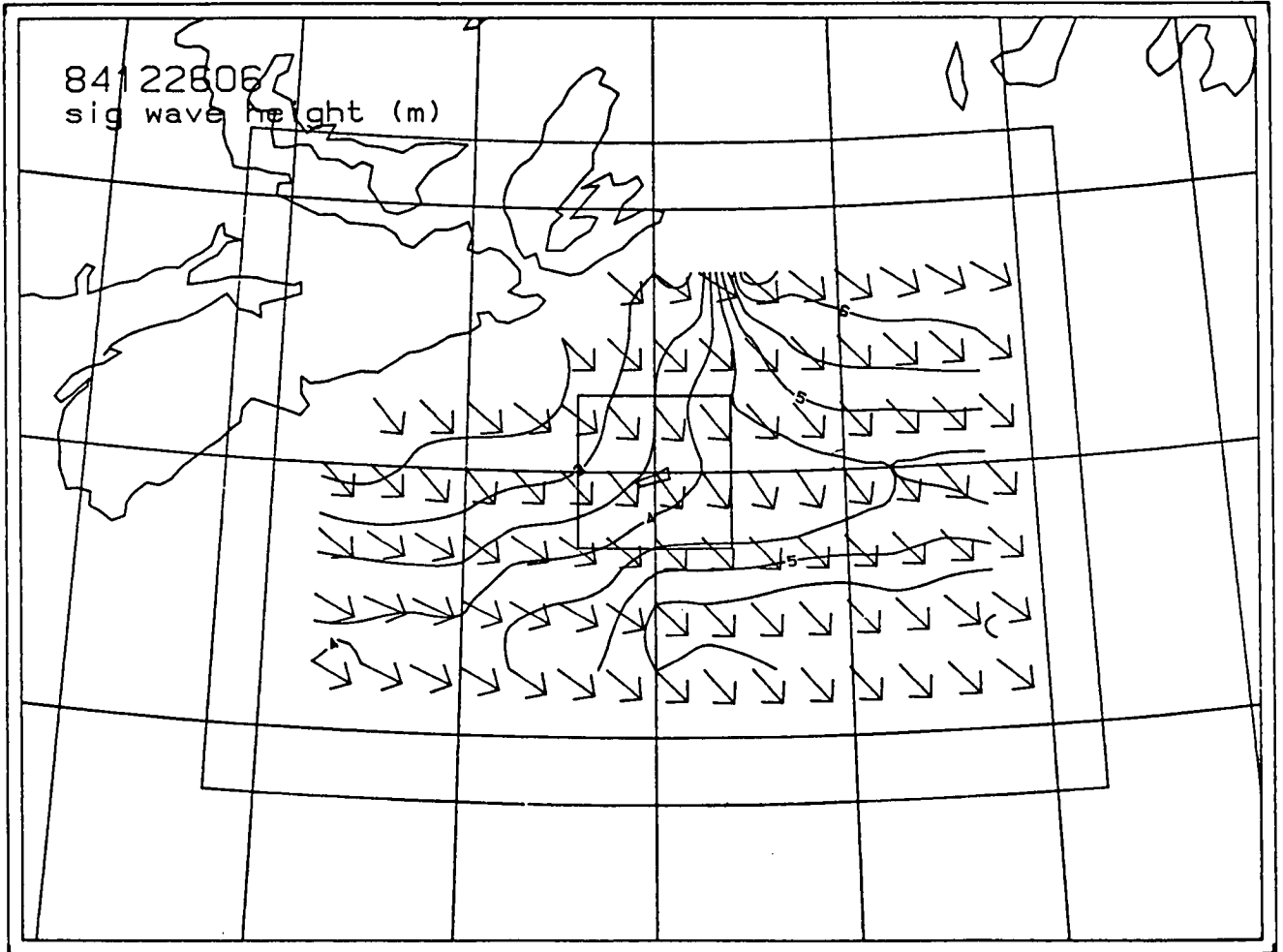


Fig. 3.3(b) Typical solution for wave height and direction on the intermediate grid (shown here for 06 GMT on December 26, 1984).



same frequency-direction resolution (16 frequencies and 16 angle bands) was used. However, the models were run independently--WAVAD by D. Resio and SPECREF by Seaconsult--with the choice of grid size and source-sink term coefficients selected as appropriate for the theory in each model. The objective here was to apply the models so as to give optimum accuracy within constraints on the grid size for normal wave hindcasting.

### 3.2 Storm Selection

The four distinct storms monitored in the new database were briefly described in Section 2.2. Of these, the first three were similar in that winds, initially strong out of the south-southeast, shifted to the west or west-northwest as the storm peaked over Sable Island. These storms produced waves from the south, turning to southwest and west as the storm developed. Storm 4 differed in that winds were comparatively steady from the southwest throughout the event.

None of the four storms produced easterly incident waves on Sable Island Bank. This was unfortunate since proposed gas production facilities on the eastern flank are likely to be governed by waves incident from easterly directions. Environmental design studies for Mobil Oil Canada, Ltd. have shown significant shallow water wave modification, including the potential for crossing breaking waves. Therefore, in order to include one storm in the hindcast analysis incident from the east, an event occurring on March 29-31, 1984 was selected. As shown in Fig. 3.1, three non-directional Waveriders were deployed in intermediate to shallow water depths on East Bar, all of which yielded good validation records. This storm was also selected because it was not one of the events identified for the Mobil sponsored hindcast study planned for 1985/86.

In view of the similarity of winds and waves in storms on December 25-28, 1984 and January 15-18, 1985, this latter storm was excluded from the hindcast, and the March 1984 event was substituted. Thus, the following events were selected to provide a set of storms with differing wind-wave conditions while optimizing the directional data:

Storm No.	Wave Directions (Deep Water)	Water Depth d (m)	Shallow Water Peak Conditions			
			$H_s$ (m)	$T_p$ (s)	$d/gT^2$	$H_s/gT^2$
1: Mar. 29-31, 1984	NE to E	21	6.8	11.4	0.0165	0.0053
2: Dec. 25-28, 1984	S to NW	12	3.8	10.4	0.0113	0.0036
3: Jan. 05-08, 1985	WSW to SW	12	4.2	13.1	0.0071	0.0025
4: Jan. 20-24, 1985	SW	12	6.2	11.4	0.0094	0.0049

Hindcasted surface pressure distributions and associated wind fields are presented in Appendix 1.

The maximum significant wave height and its corresponding peak period at the shallowest water gauge are listed above for each storm together with the values for  $d/gT^2$  and  $H_s/gT^2$ . These values are plotted in Fig. 3.4 along with the storm example from the SWIM intercomparison study reported by Bouws et al. (1985). We see that the four events modelled here fall into the range of wave heights strongly influenced by shallow water (departure from linear wave theory), and thus constitute a critical test of the models used. Each event is, in fact, slightly further into the nonlinear range than that from the North Sea used by Bouws et al. in SWIM.

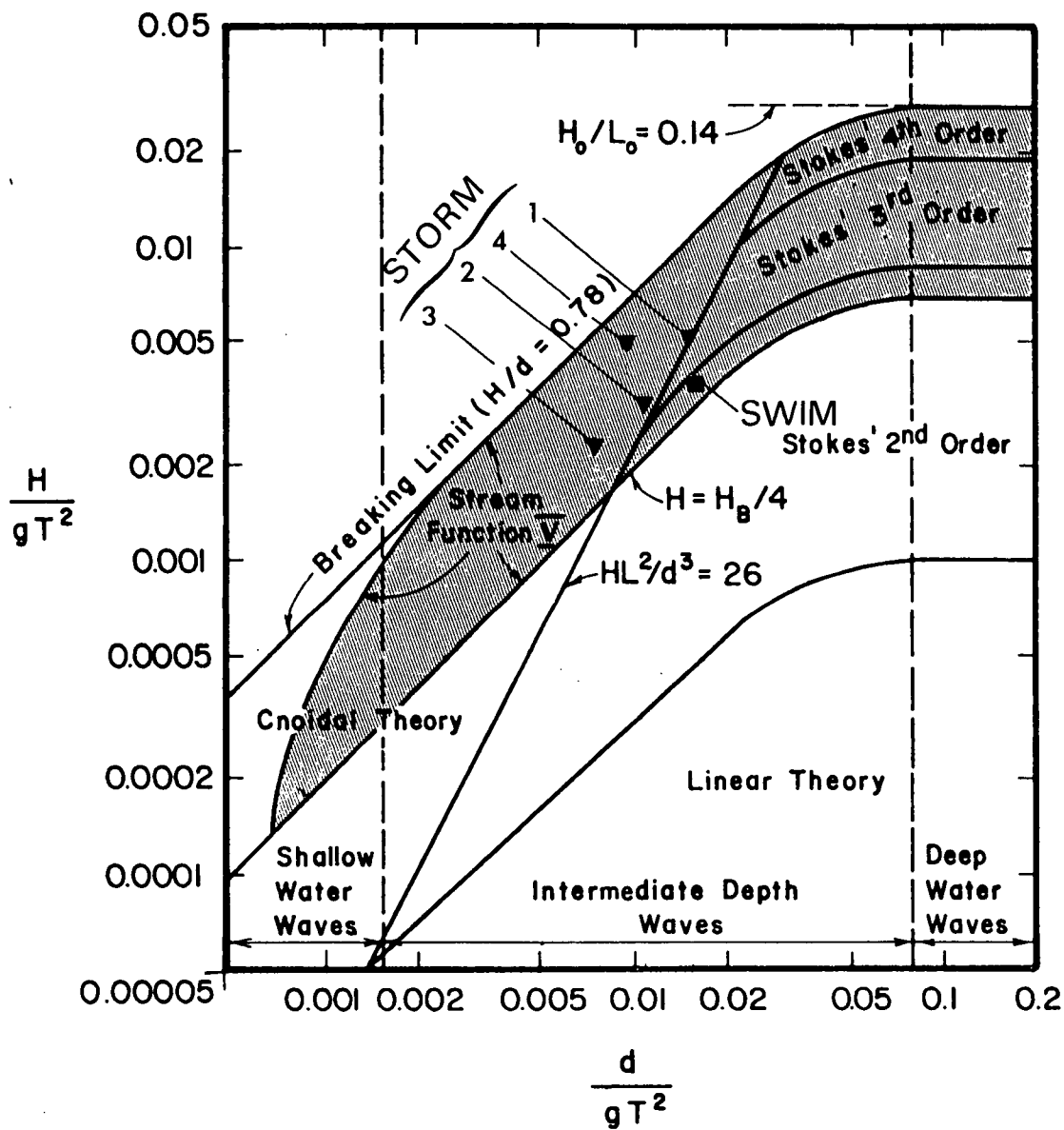


Fig. 3.4 Location of the four storm events in the wave theory graph. The SWIM point is based on data from Bouws et al. (1985).

### 3.3 Idealized Test Cases

In order to provide insight into model behaviour under wind conditions producing strong wave growth at a large angle to the incident wave propagation direction, two idealized test cases were examined. In each case, a JONSWAP spectrum (Hasselmann et al., 1973; equation 2.4.1) was specified at the open southern boundary propagating due north. In the first test, wind sea conditions were specified, whereas a wave regime more typical of swell was chosen for the second test. Each test was run first without wind, and then rerun with a wind of 40 knots out of the west for examination of the wind generated growth characteristics (4 tests in all). The actual input parameters are given in Table 3.1.

Output spectra were generated at 11 output points with water depths ranging from 101 m to 10 m along a line normal to Sable Island (column 31 of the 61 x 61 1-n.m. grid--Fig. 3.5). The output point coordinates and water depths are given in Table 3.1.

Table 3.1

Idealized Test Case Parameters

Test No	Wave Regime	$f_m$ (Hz)			$p$ (°T)	spreading exponent s	wind speed (knots)	wind direction (°T)
A1	wind sea	0.100	0.010	3.3	180	2	0	0
A2	wind sea	0.100	0.010	3.3	180	2	40	270
B1	swell	0.0625	0.002	7.0	180	4	0	0
B2	swell	0.0625	0.002	7.0	180	4	40	270

OUTPUT POINTS

	1	2	3	4	5	6	7	8	9	10	11
x-coordinate	31	31	31	31	31	31	31	31	31	31	31
y-coordinate	8	12	14	16	18	20	22	23	24	25	26
water depth (m)	101	70	61	57	53	50	40	34	29	24	10

### **3.4 Model Application to Sable Island Bank**

The WAVAD model was applied to the shallow water domain with boundary conditions  $(S(\mathbf{x},f,\theta,t))$  provided from the nested intermediate grid shown in Fig. 3.2. The grid spacing  $\Delta x$  was chosen as 5 n.m. (9260 m) for the hindcasts which provided adequate bathymetric resolution for refraction and an approximation of the Sable Island landform suitable for modelling exposed sites. The differences in predicted wave heights, periods and directions between the 5 n.m. grid and a finer grid, matched to that used with SPECREF, were examined using storm 2 (see Section 4.4). The depth field  $h(\mathbf{x})$  was scaled from CHS Field Sheets No. 4992 and 4993 for both grids.

Spectral resolution was chosen as 16 frequency bands and 16 directions giving a spectrum with 256 degrees of freedom. All storms were modelled without friction ( $C_f = 0$ ) consistent with the hypothesis that under conditions of active wave generation, frictional losses would be unimportant compared with the remaining source-sink terms in the energy balance equation. The model parameters are summarized in Table 3.2 for this application.

For the SPECREF hindcasts, the open sea boundaries of the model grid were matched exactly to those shown for the reference shallow water area in Fig. 3.2. The grid spacing  $\Delta x$  was 1 n.m. (1852 m) which provided the bathymetric resolution shown contoured in Fig. 3.5. Charted depths (CHS Field Sheets No. 4992 and 4993) were extracted on the 1 n.m. grid for the input  $h(\mathbf{x})$ .

Given this spatial resolution, convergence for  $ds = 1.\Delta x$  was established by solving for the characteristic rays at site 253 over the range of frequencies (0.05,0.20 Hz) used for the hindcast and showing that ray intersection points and angles on the boundaries fell inside tolerances of  $0.1\Delta x$  and one degree. The range of  $ds$  tested was  $1.\Delta x$  to  $0.25\Delta x$ ; all values of  $ds$  provided intersections within these tolerances.

Frequency and direction resolution was established by convergence of a discrete spectrum  $S(f,\theta)$  to a parametric JONSWAP spectrum with spreading

**Table 3.2**  
**Summary of WAVAD Parameters**

Parameter	Sable Island Bank Application
$\Delta x; \Delta y$	5 n.m. (9.260 km) 1 n.m. (1.852 km)
f (Hz)	$f_i = 0.05 + (i+1)\Delta f, i=1,2,\dots,16$ $\Delta f = 0.010$ Hz
$\theta$ (degrees True from)	$\theta_j = 0 + (j-1)\Delta\theta, j=1,2,\dots,16$ $\Delta\theta = 22.5^\circ$
$\alpha_u$ (Eq. 1.15)	0.0042
$\epsilon$ (Eq. 1.17)	100
$C_f$ (Eq. 1.12)	0.0 (i.e. no bottom friction)



1 n.m. grid

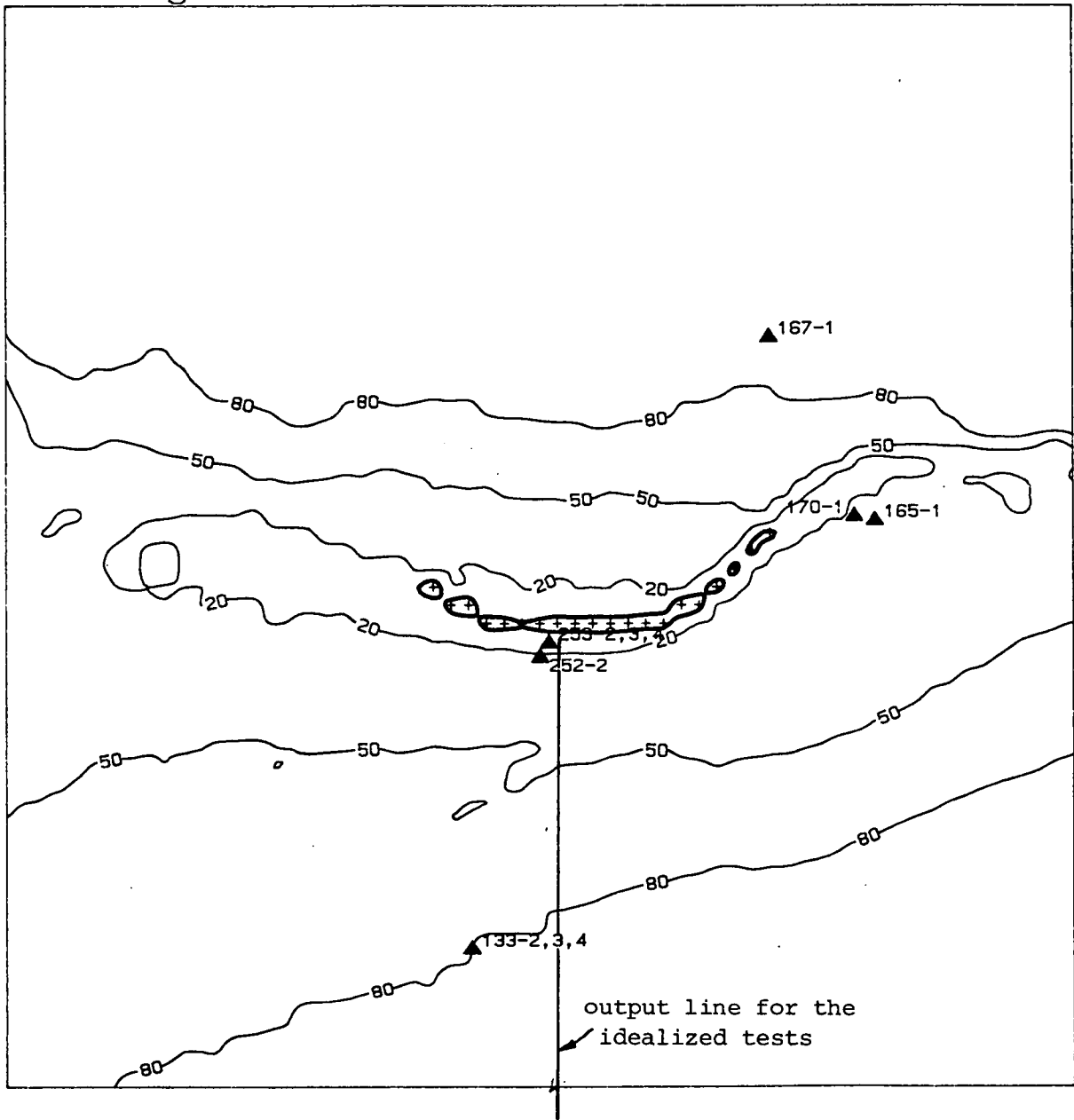


Fig. 3.5 Contoured bathymetry as resolved on the one n.m. grid used in SPECREF.

as defined by Hasselmann et al. (1980). Sixteen frequencies and 16 angle bands were found to be very adequate in resolving the spectral shape and preserving total energy.

The remaining parameters,  $\alpha$ , B-growth coefficient and  $C_f$  were chosen to conform with published values. The final run specifications are given in Table 3.3.

Table 3.3

Summary of SPECREF Parameters

Parameter	Sable Island Bank Application
$\Delta x; \Delta y$	1 n.m. (1.852 km)
f (Hz)	$f_i = 0.05 + (i+1)\Delta f, i=1,2,\dots,16$ $\Delta f = 0.010$ Hz
$\theta$ (degrees True from)	$\theta_j = 0 + (j-1)\Delta\theta, j=1,2,\dots,16$ $\Delta\theta = 22.5^\circ$
ds	1.852 km
$\alpha$ (Eq. 1.15)	0.0081
B-growth coefficient (Eq. 1.26)	5
$C_f$ (Eq. 1.28)	0.0 (i.e. no bottom friction)

#### 4.0 INTERCOMPARISON RESULTS

The results for the base set of model runs for the four hindcast storms are examined here in terms of characteristic properties of the predicted spectra (specifically significant wave height  $H_s$ , spectral peak period  $T_p$ , and wave direction  $\bar{\theta}$ ) and in terms of spectral shape by comparing predicted and measured directional spectra at stations 252 and 253. The characteristic parameters were defined as follows:

(i) from modelled spectra

$$H_s = \begin{cases} \sum_i \sum_j S(f_i, \theta_j) \Delta f \Delta \theta & 0.20 \geq f \geq 0.05 \text{ Hz} \\ + \\ \text{saturated form of } E(f) & f > 0.20 \text{ Hz} \end{cases} \quad (4.1)$$

$$T_p = f_p^{-1} \quad (4.2)$$

$$\bar{\theta} = \begin{cases} \theta(f_p) & \text{SPECREF} \\ \langle \theta \rangle \text{ weighted by} & \text{WAVAD} \\ \text{energy density} & \end{cases} \quad (4.3)$$

where  $\langle \rangle$  denotes an averaging process;

(ii) from measured spectra

$$H_s = \sum_i E(f_i) \Delta f \quad (4.4)$$

where

for stations  
(Fig. 2.1)

$0.0331 \leq f_i \leq 0.5131 \text{ Hz}$ , $f = 0.0075 \text{ Hz}$	252, 253
$0.0366 \leq f_i \leq 0.5054 \text{ Hz}$ , $f = 0.0073 \text{ Hz}$	165, 167, 170
$0.0366 \leq f_i \leq 0.4980 \text{ Hz}$ , $f = 0.0073 \text{ Hz}$	133

$$T_p = f_p^{-1} \quad (4.5)$$

$$\bar{\theta} = \theta_p \quad (4.6)$$

The modelled spectra span a smaller frequency range than the measured spectra and so are not exactly equivalent. The choice of 16 frequency bands in the modelled spectra represents a compromise between reasonable

resolution and computational efficiency. Since model performance is to be judged against the best estimate of the actual sea state, the following comparisons are made assuming that the low and high frequency contributions from outside the modelled range are negligible, or alternately that they will appear as a deficiency in model predictions.

These parameters are compared (model versus measured) in two ways-- first, as time-series plots for visual inspection, and second, in terms of four statistical measures:

- (i) systematic mean square error -  $MSE_S$

$$MSE_S = \langle (H_S(\text{meas.}) - H_S(\text{l.s.f.}))^2 \rangle \quad (4.7)$$

- (ii) unsystematic mean square error -  $MSE_U$

$$MSE_U = \langle (H_S(\text{pred.}) - H_S(\text{l.s.f.}))^2 \rangle \quad (4.8)$$

- (iii) root mean square error - RMSE

$$RMSE = (MSE_S + MSE_U)^{1/2} \quad (4.9)$$

- (iv) scatter index of  $H_S$  - SI

$$SI = \text{s.d.} \left\{ \frac{H_S(\text{pred.}) - H_S(\text{meas.})}{\langle H_S(\text{meas.}) \rangle} \right\} \quad (4.10)$$

where l.s.f. denotes the "least squares" regression of  $H_S(\text{pred.})$  onto  $H_S(\text{meas.})$  and s.d. indicates the standard deviation of the quantity contained in the brackets.

These definitions were chosen so that the predictions made here in shallow water could be compared with statistics presented by Clancy et al. (1986) for the SOWM and GSOWM deep water spectral wave models operated by the U.S. Navy.

#### **4.1 Prediction of Characteristic Wave Parameters**

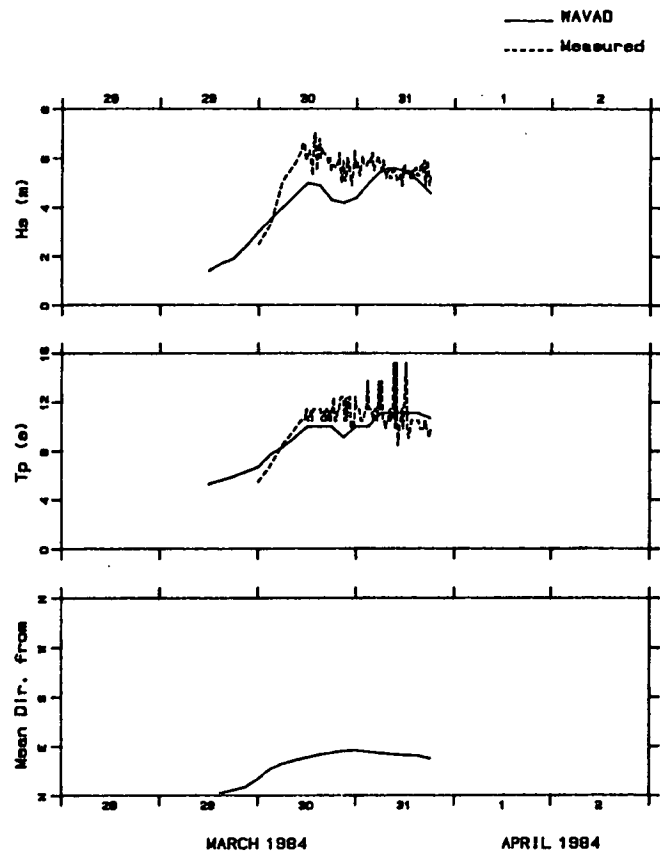
The time-series comparisons for storm 1 (March 29-31, 1984) are shown in Fig. 4.1. and 4.2 for the two available shallow water stations (165 and 170). The measured data were non-directional. This storm is interesting because it represents the important case of NE waves, giving rise to shallow water conditions on East Bar following transformation over the comparatively complicated bathymetry to the east of the island. As the measurements show, seas built rapidly on March 30th, peaking at about 7 m at station 165 and about 5.8 m at station 170. Peak periods at the time of maximum waves ranged from 11 to 12 s, but increased later in the storm to an average of approximately 13 s showing, however, a considerable range from 10 to 15.5 s.

In this example, neither spectral model captures the growth stage of the storm well (WAVAD is closer than SPECREF), but both exhibit energy levels in agreement with each other and with measurements late in the storm (March 31st) at station 165. The reason for the failure of the models early in the storm is poor resolution of strong winds at that time. The shallow water results are dominated by the boundary conditions supplied by the coarse grid prediction; hence the wind field error would show up mainly in this boundary condition (in terms of  $m_0$  or  $H_s$ ) rather than in terms of wave growth between the boundary and either measurement site during the shallow water calculation.

Peak periods are well-modelled by SPECREF through the energetic portion of the storm ( $H_s > 5$  m); they are slightly underpredicted by WAVAD. Later results indicate a similar trend for WAVAD in other storms.

The most important difference between model predictions in this storm and the wave measurements is that both models fail to reproduce the large change in total energy between the two gauge sites. These two sites are separated by about 2 km in 20 to 25 m of water (unless there is a recording error in Waverider position) and there is no indication that the change in sea state intensity measured by the buoys is not real. Thus we find that wave properties on Sable Island Bank exhibit large spatial variations down to scales of about 5 to 10 km. The failure

Storm #1 - Stn. 165



Storm #1 - Stn. 165

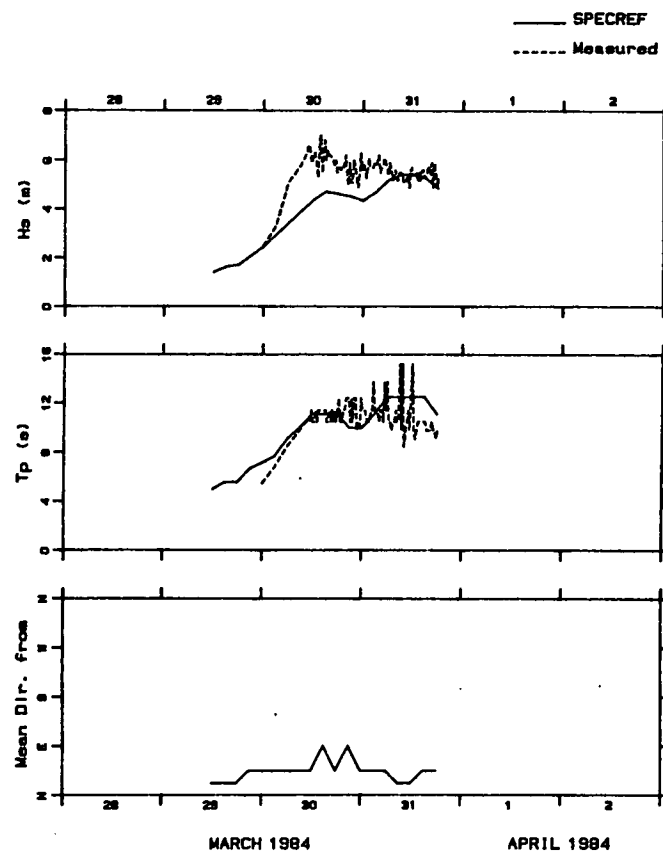
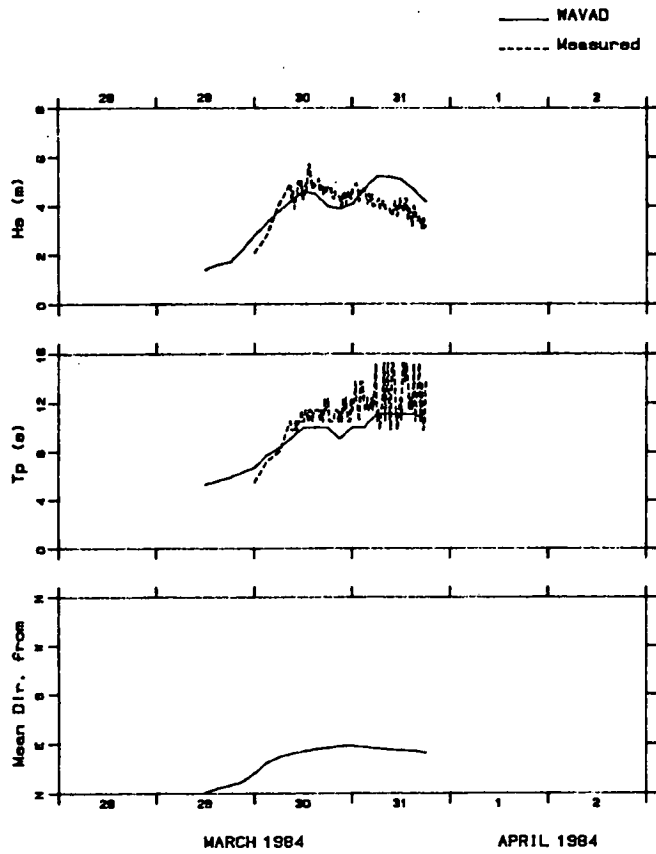


Fig. 4.1 Comparison of predicted and measured wave properties in storm 1 (station 165).

Storm #1 - Stn. 170



Storm #1 - Stn. 170

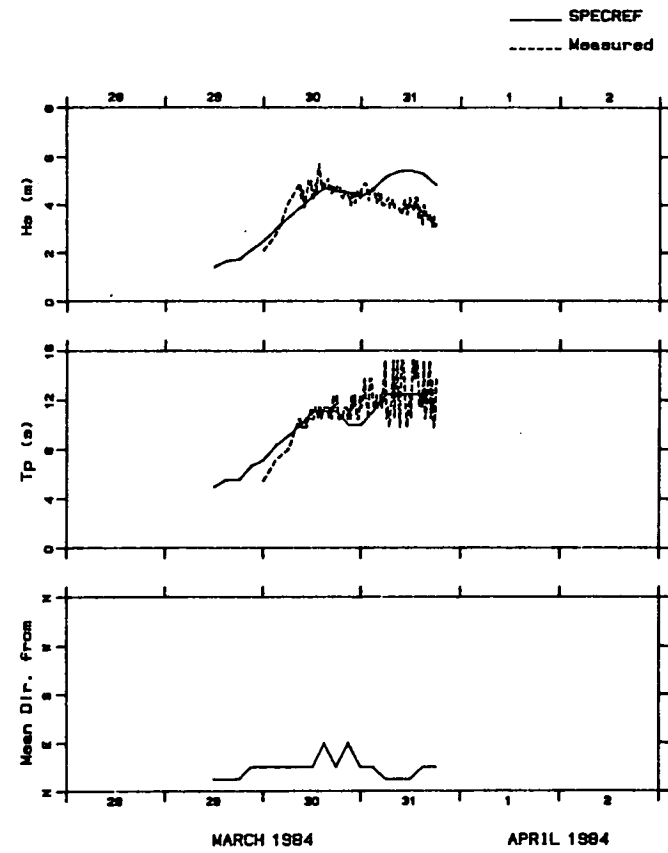


Fig. 4.2 Comparison of predicted and measured wave properties in storm 1 (station 170).



of the models to reflect this sensitivity may be related to such model parameters as grid spacing and frequency/direction resolution, or to boundary condition errors in wave period or direction. Without directional wave measurements on the boundary it is not possible to identify which of these causes is important.

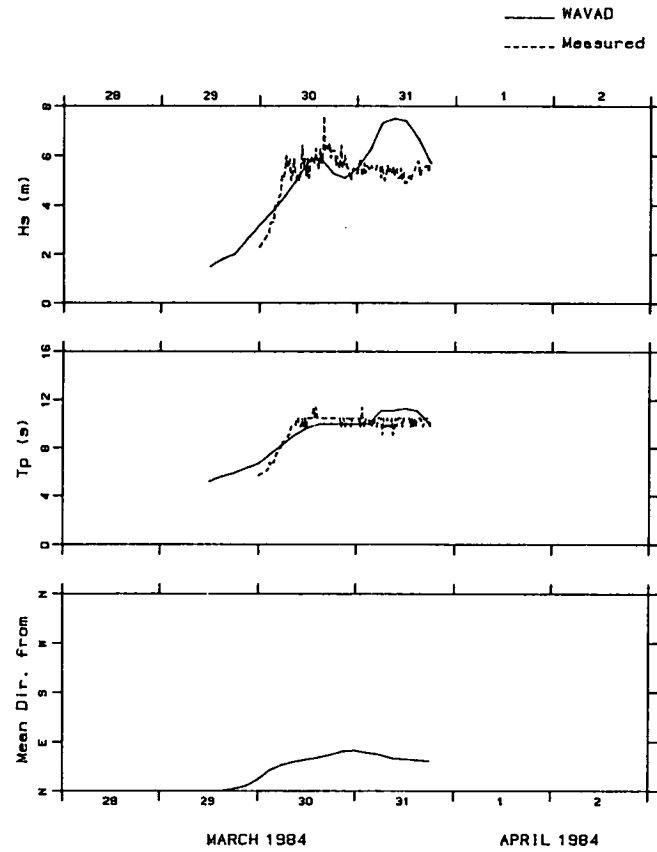
Nevertheless, the error in the peak  $H_S$  value amounts to about 20% (low) at station 165 during the most severe portion of the storm. This error estimate is derived by smoothing  $H_S$ -measured to remove some of the sampling variability contained in the 20-minute data plotted in the figures.

Deep water comparisons at station 167 (Fig. 2.1) are shown in Fig. 4.3. The two-peaked character of the modelled time-series is very evident here and produces substantial disagreement in  $H_S$  in the late stages of the storm. Neither model gives particularly good predictions of the rapid sea state development and subsequent 24 h of sustained 5 to 6 m  $H_S$  wave heights, but both reproduce the peak  $H_S$  value within about 10 to 15% of the measured values. The lack of agreement in the time-series behaviour is consistent with the trends found in shallow water and, as stated above, most likely results from wind field errors.

In storms 2, 3 and 4 comparison plots will be presented for Station 133 which, although not located exactly on the deep water seaward boundary of the shallow water model, is close enough to it so that depth-dependent processes are weak. This comparison thus provides an indication of how well the boundary conditions have been reproduced for input to the shallow water models, and what errors may be attributed to these conditions rather than to transformation processes in the individual formulations.

The station 133 comparison for storm 2 is shown in Fig. 4.4. The general character of the storm between December 25th and late on the 27th is well modelled except for the rapid decay in  $H_S$  just following the second peak on December 27. There are clearly differences between the model responses, evidenced by the generally lower energy levels in the SPECREF predictions. This difference provides a better fit to data during the

Storm #1 - Stn. 167



Storm #1 - Stn. 167

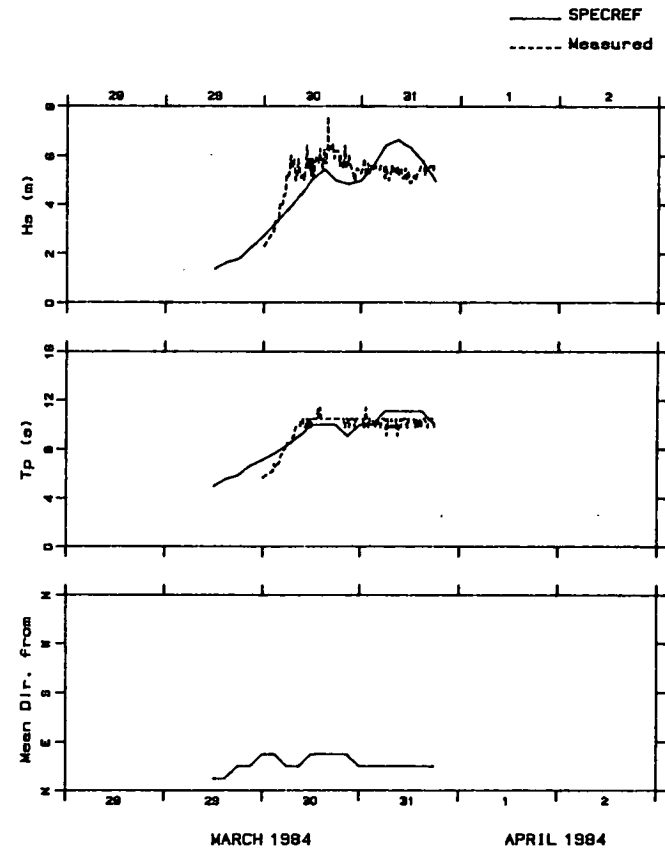
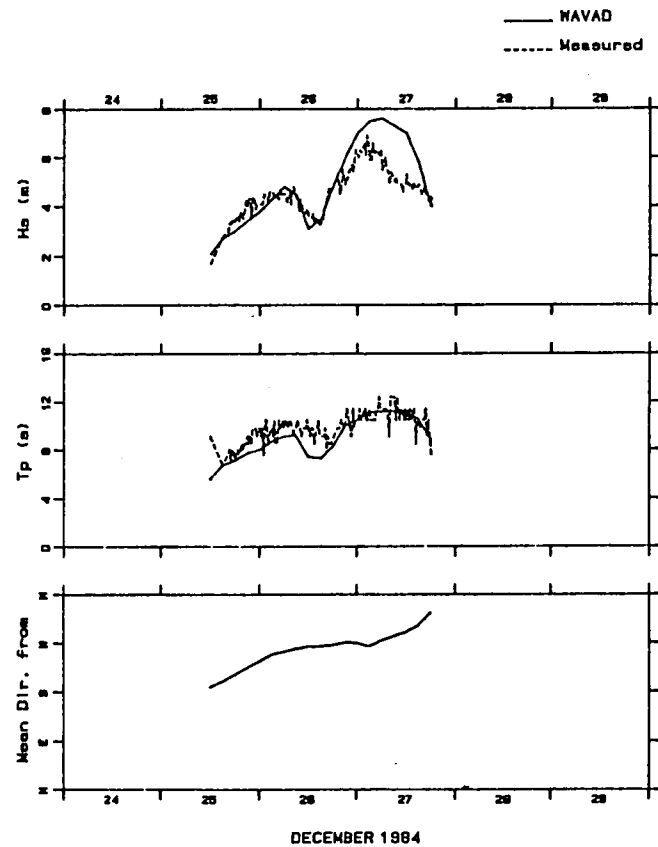


Fig. 4.3 Comparison of predicted and measured wave properties in storm 1 (station 167).

Storm #2 - Stn. 133



Storm #2 - Stn. 133

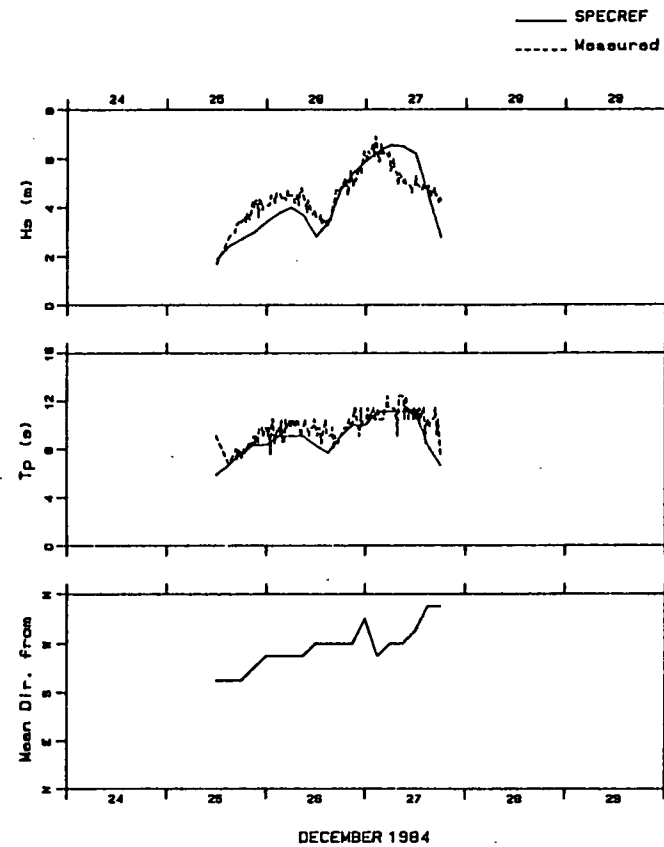


Fig. 4.4 Comparison of predicted and measured wave properties during storm 2 (station 133).

second peak but the opposite is true during the December 26th maximum when WAVAD is generally more accurate. Both models underpredict peak period during the first stage of the storm but give good agreement during the second.

The storm 2 shallow water comparisons in 22 m of water (Fig. 4.5) show that both SPECREF and WAVAD model  $H_s$  for the second growth-decay stage (December 26-27) well but underestimate the first stage. In the case of SPECREF this is consistent with the station 133 results; it is harder to explain for WAVAD since energies in deeper water were well modelled at this time. In shallow water ( $h = 12$  m) the  $H_s$  predictions are in very close agreement with measurements (Fig. 4.6).

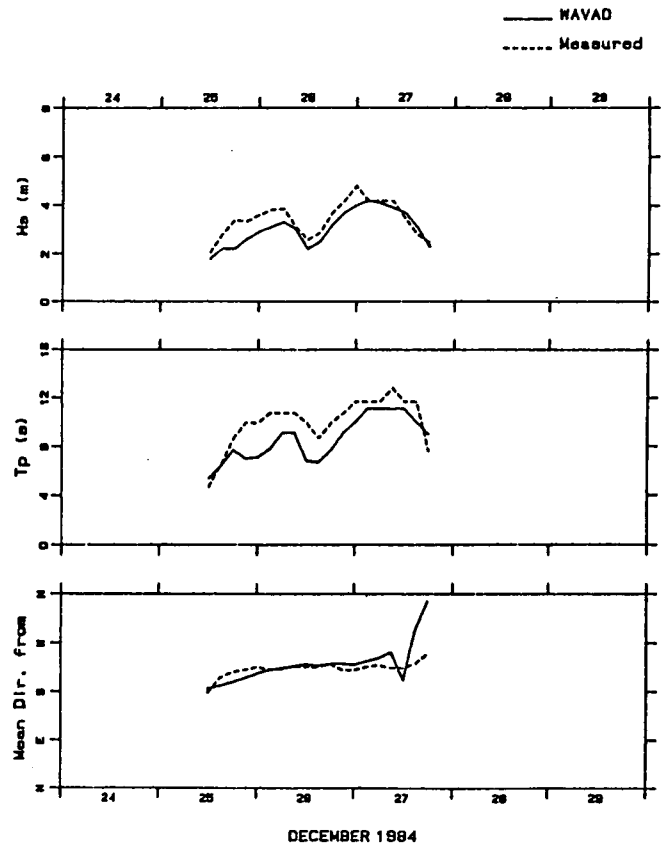
In general, WAVAD underestimates  $T_p$  at all times with perhaps an increasing error as one moves into shallower water. SPECREF provides low estimates of  $T_p$  during the first stage, consistent with the boundary data, but gives a very favourable prediction at station 253 in the second stage.

The WAVAD directions in both water depths also compare favourably with measurements except late in the storm when winds have decayed to under 30 knots. There is greater variability in the SPECREF directions, linked obviously to changes in  $T_p$ , but this model too shows reasonable agreement with measurements. Importantly the data show about a 20° to 30° directional shift in wave energy between  $h = 22$  m and  $h = 12$  m; both models do reproduce this shift in direction produced by refraction.

The station 133 comparisons for storm 3 are shown in Fig. 4.7: neither model picked up the very rapidly developed first peak late on January 5th that coincided with winds exceeding 60 knots for 3 to 4 hours, but both models do capture the subsequent developments. WAVAD generally overestimated  $H_s$  in this later period while SPECREF shows good agreement; both models give a good prediction of  $T_p$  after noon on January 6th and show insignificant differences in wave direction throughout the storm.

Unfortunately, a recorder failure limits the data near the early peak of

Storm #2 - Stn. 252



Storm #2 - Stn. 252

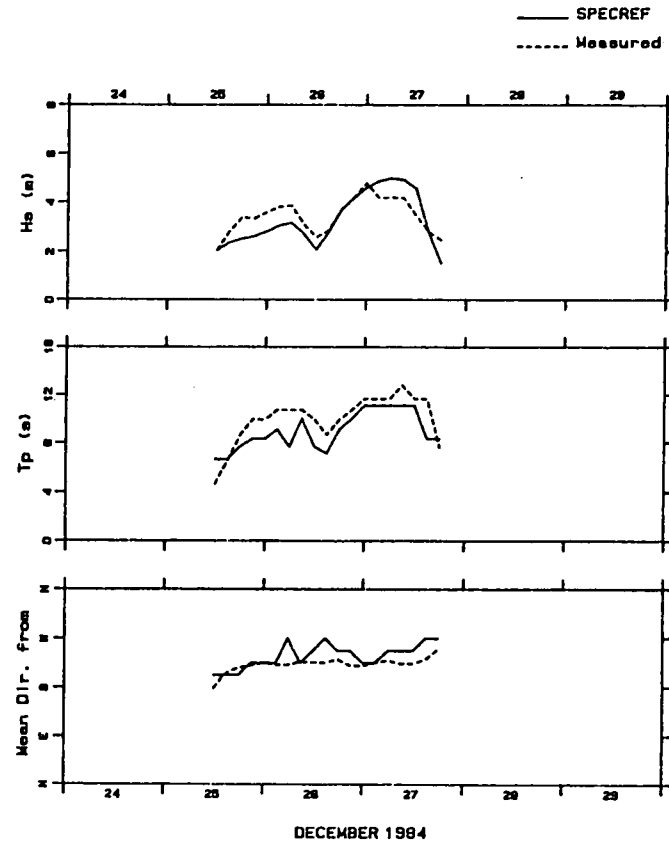
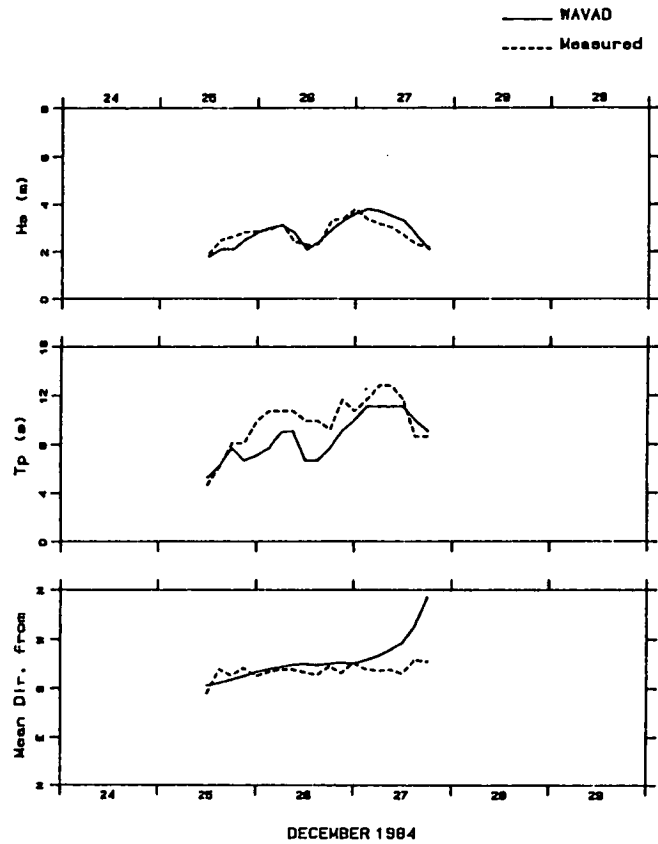


Fig. 4.5 Comparison of predicted and measured wave properties in storm 2 (station 252).

Storm #2 - Stn. 253



Storm #2 - Stn. 253

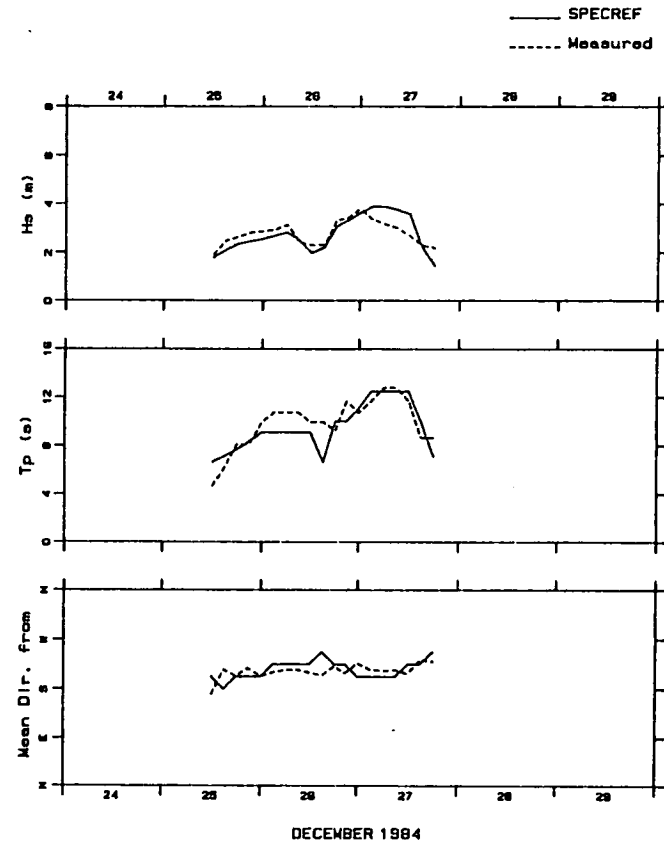
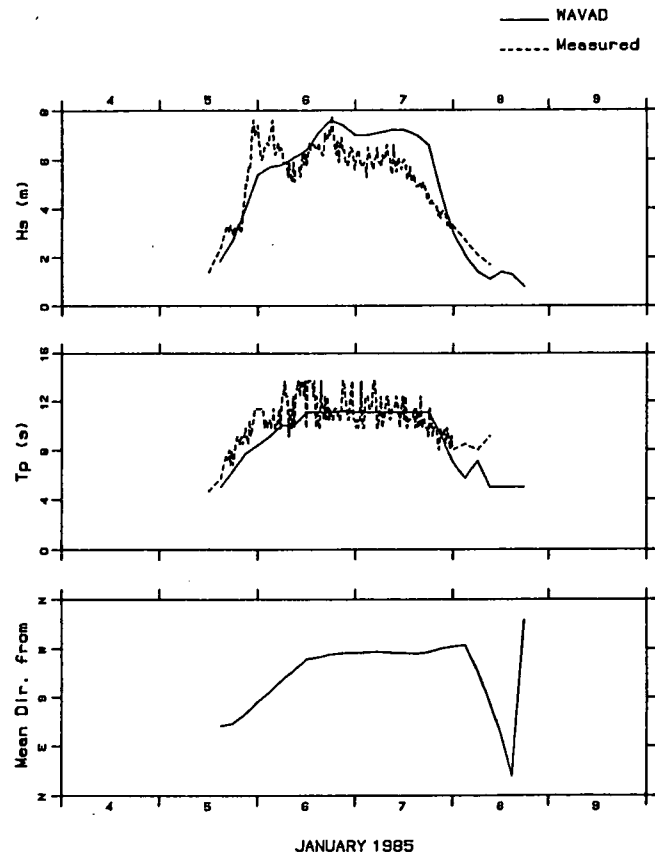


Fig. 4.6 Comparison of predicted and measured wave properties in storm 2 (station 253).

Storm #3 - Stn. 133



Storm #3 - Stn. 133

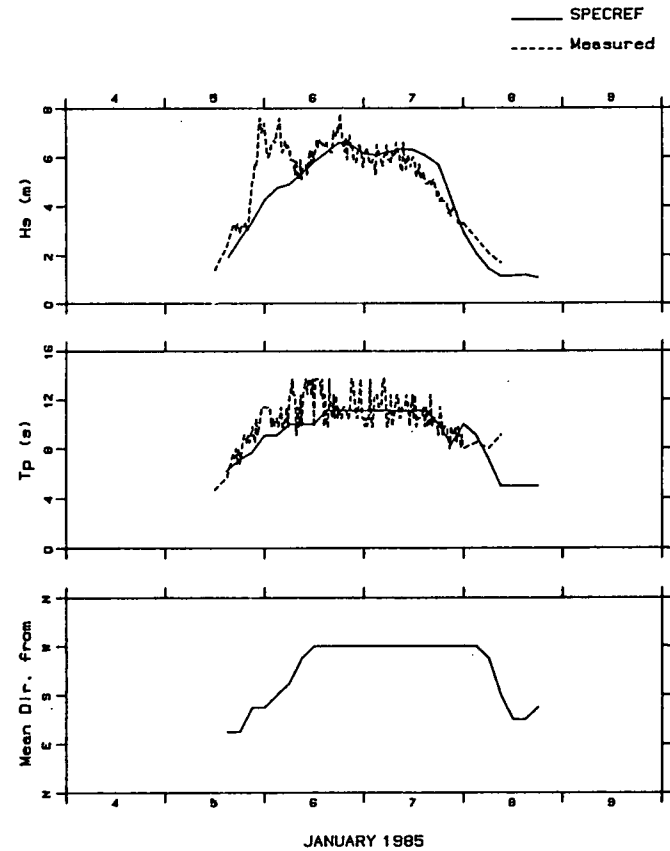


Fig. 4.7 Comparison of predicted and measured wave parameters for storm 3 (station 133).

the storm, but the second, sustained peak was measured. Both spectral models appear to give a very satisfactory prediction of  $H_s$  and  $\bar{\theta}$  in 12 m of water (Fig. 4.8). As noted previously WAVAD has a tendency to underestimate  $T_p$  and this is in evidence in this storm also.

It is noted that this storm was characterized by steadily turning winds during the growth stage. It presents quite a severe test of the deep water spectral model as well as of the shallow water transformations. Storm 4 by contrast, was characterized by comparatively steady wind directions. The deep water time-series for storm 4 are shown in Fig. 4.9. In general both models follow the storm variations well: WAVAD has a tendency to overpredict  $H_s$  and under-estimate  $T_p$ ; SPECREF shows slightly better agreement for both parameters. At station 253 we found, however, a substantial difference in the model predictions (Fig. 4.10). SPECREF fails to model the peak response in  $H_s$  on January 21st (a 20% error against the measured value), but correctly simulates the late stages of the storm. This decoupled model overestimates  $T_p$  in this event but very adequately models wave direction  $\bar{\theta}$ .

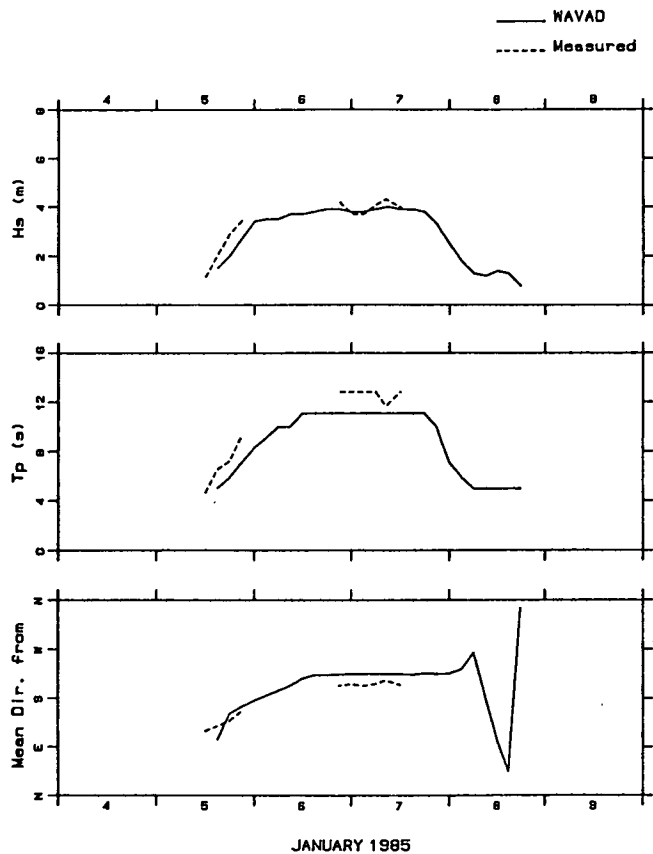
WAVAD in this case is consistently low in  $H_s$  by more than 1 m in 5 to 6 m measured and low with respect to  $T_p$ . There is no apparent explanation in terms of wave direction since at various times in storms 2 and 3 waves were from the SW, as they were in storm 4, without the corresponding lack of agreement in  $H_s$  and  $T_p$ .

These time-series are valuable in showing how well each model performs in reproducing the storm sea histories for different incident wind and wave conditions. To give a more quantitative measure of model accuracy the statistical parameters defined in (4.7) to (4.10) were computed for  $H_s$ , and means and standard deviations were calculated for errors in  $T_p$  and  $\bar{\theta}$ . In order to reflect the error in  $T_p$  in a manner that incorporates the frequency resolution used in each model a new parameter  $E_{TP}$  was defined as follows

$$E_{TP} = \text{INT} \left\{ \frac{f_p(\text{meas.}) - f_p(\text{predict.})}{\Delta f} \right\} \quad (4.11)$$



Storm #3 - Stn. 253



Storm #3 - Stn. 253

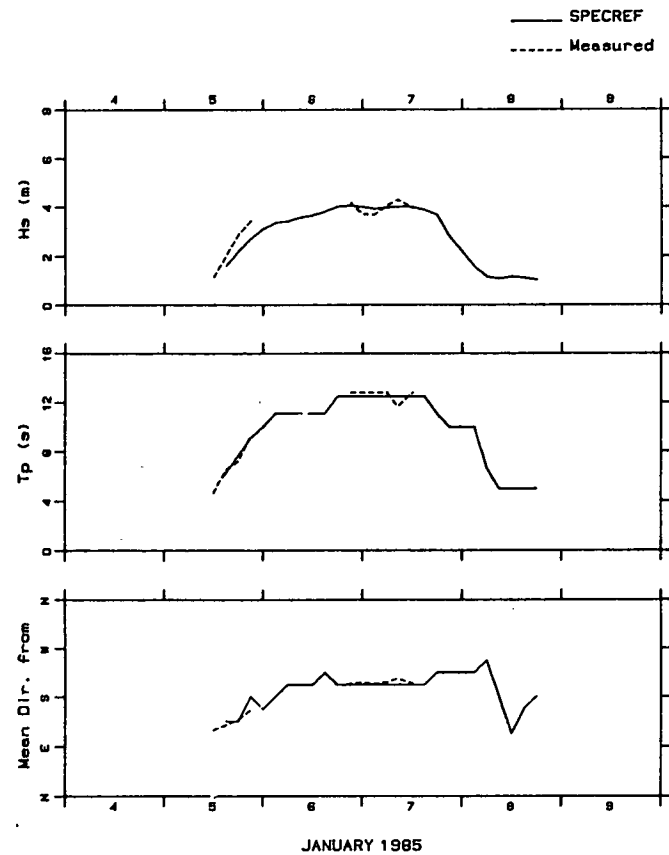
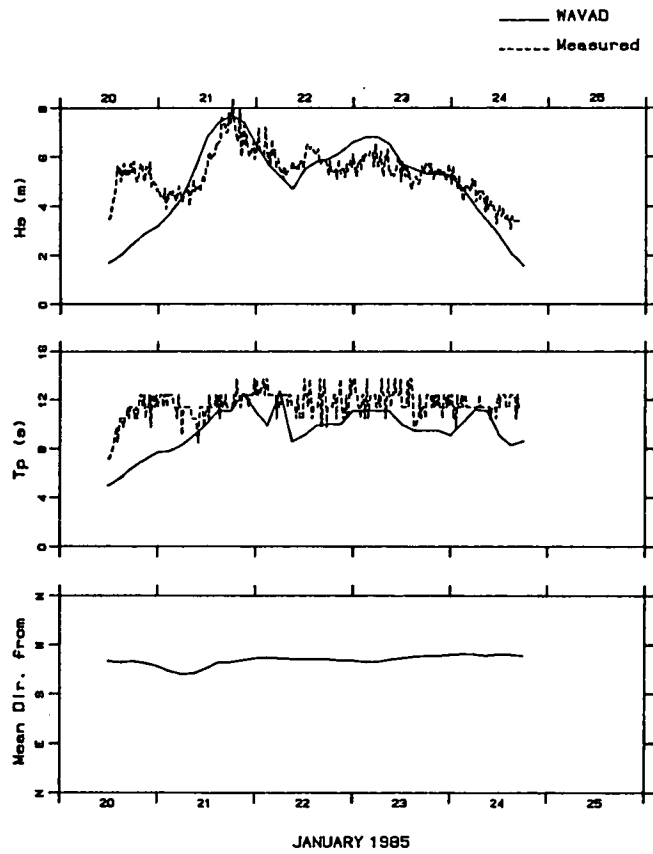


Fig. 4.8 Comparison of predicted and measured wave parameters for storm 3 (station 253).

Storm #4 - Stn. 133



Storm #4 - Stn. 133

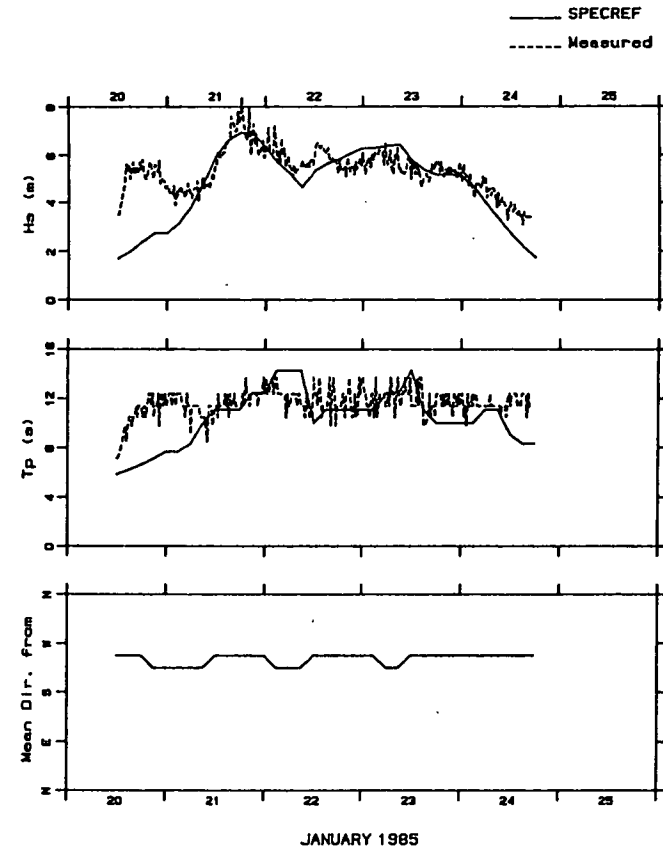
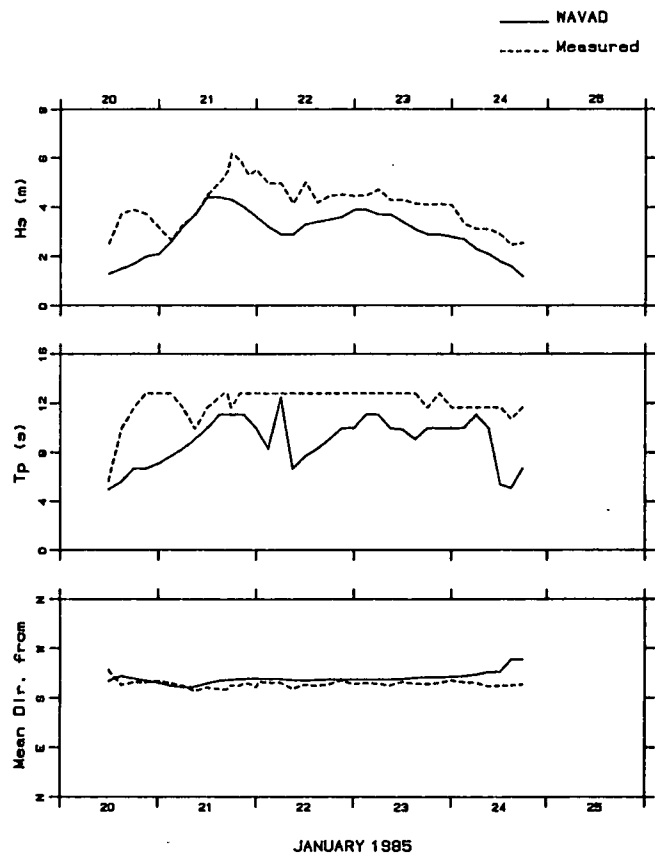


Fig. 4.9 Comparison of predicted and measured wave parameters for storm 4 (station 133).

Storm #4 - Stn. 253



Storm #4 - Stn. 253

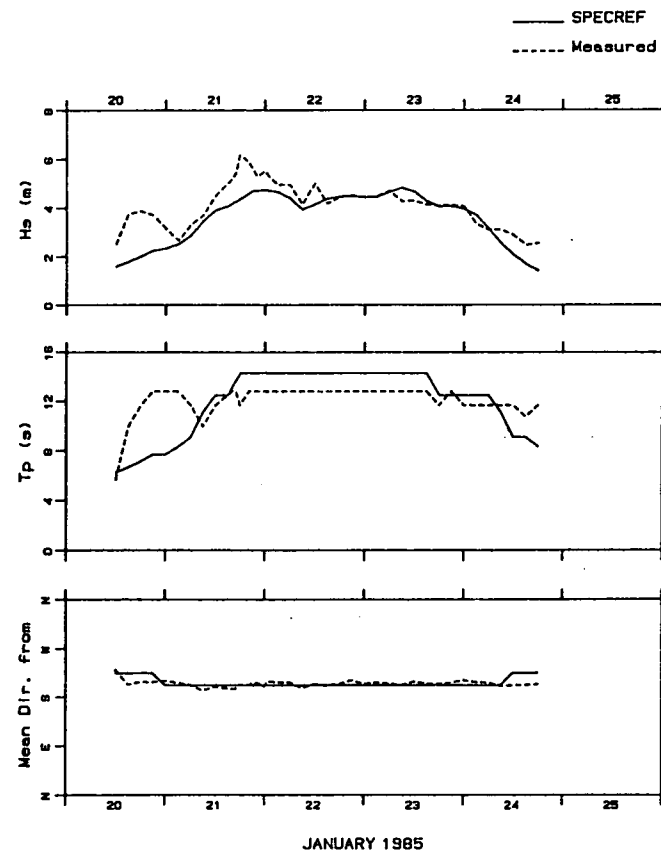


Fig. 4.10 Comparison of predicted and measured wave parameters for storm 4 (station 253).

where  $f$  is the frequency spacing and INT denotes the nearest integer value. This parameter shows the number of frequency bin-widths by which model predictions differ from measured values of the peak frequency. The analogous parameter  $E$  for wave direction was defined as

$$E = \text{INT} \left\{ \frac{\bar{\theta}(\text{meas.}) - \bar{\theta}(\text{predict.})}{\Delta\theta} \right\} \quad (4.12)$$

These statistics were computed for each entire storm history after the boundary conditions had been spun up bringing the sea state into balance with the overwater wind field. The spin-up period for each storm was at least 36 h long. The data pairs forming the statistics were extracted every 3 h at exactly coincident times; thus, these measures of performance incorporate both magnitude and timing errors.

The statistics have been grouped into two classes by water depth, i.e. one where  $h > 25$  m incorporating data from stations 133 and 167, and a second where  $h < 25$  m combining data from stations 252, 253, 165 and 170. The separation by water depth has the effect of providing statistics for model predictions in deep water where shallow water effects are negligible, and in shallow water where the transformation processes related to bathymetry are important. The regressions of  $H_s(\text{pred.})$  onto  $H_s(\text{measured})$  are shown in Fig. 4.11. The frequency histograms for  $E_{TP}$  and  $E$  are shown in Fig. 4.12 and 4.13 respectively. The statistics are summarized in Table 4.1.

Perhaps the most unexpected result is that the decoupled propagation model, bounded above with a KKZ saturation spectrum, shows a slightly higher accuracy than the fully coupled WAVAD formulation. Overall the RMSE for SPECREF was found to be 1.02 m with a SI of 0.15 compared with RMSE = 1.27 m and SI = 0.21 for WAVAD. We note that Janssen et al. (1984) remark that the expected scatter index for "hindcasts with sophisticated models and high quality wind fields" is about 0.2; thus, both models are close to meeting and exceeding this criterion on accuracy.

Clancy et al. (1986) report GSOWM (a more accurate replacement for the

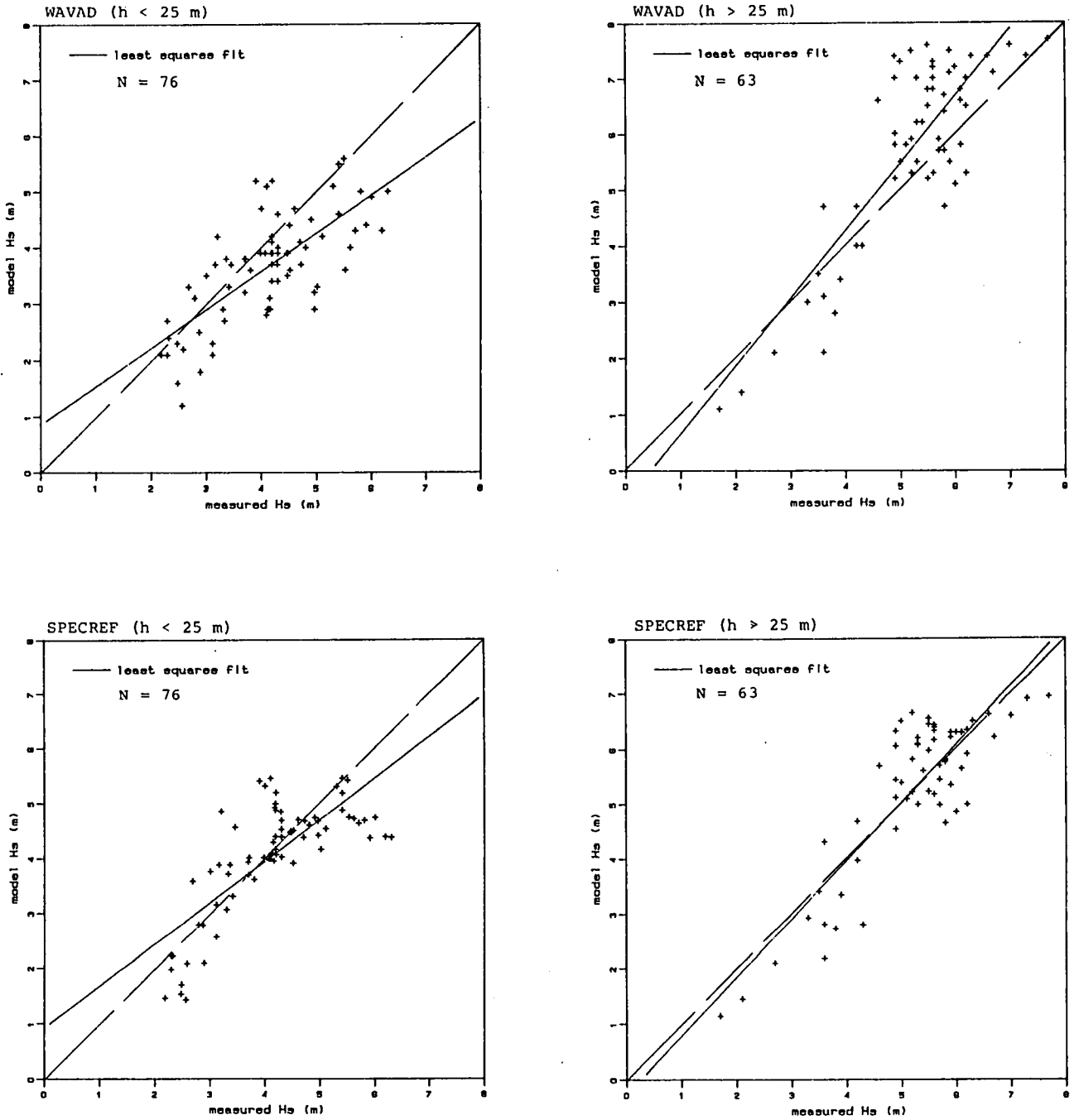


Fig. 4.11 Regressions of  $H_s$  - predicted onto  $H_s$  - measured for deep ( $h > 25$  m) and shallow ( $h < 25$  m) water on Sable Island Bank for the four hindcast storms.

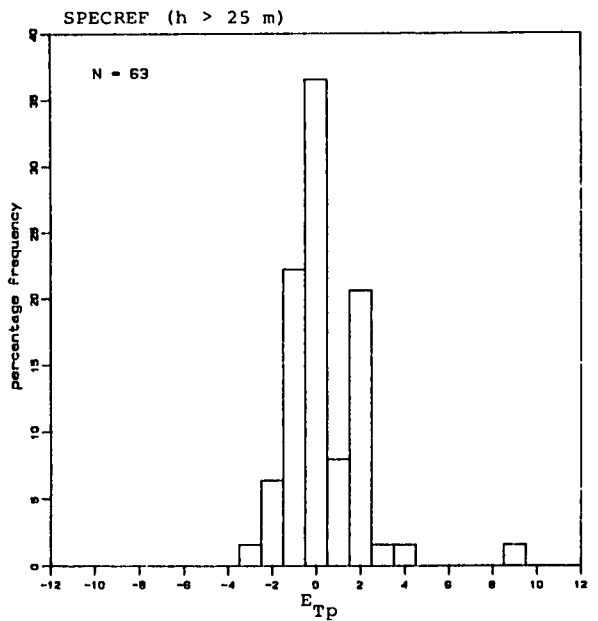
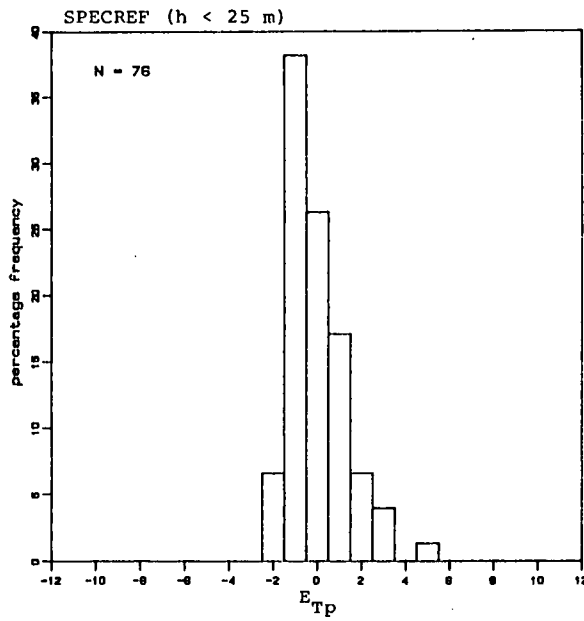
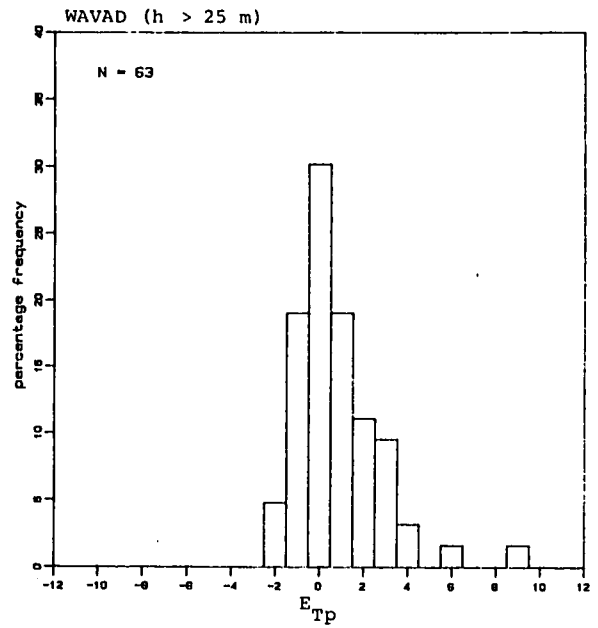
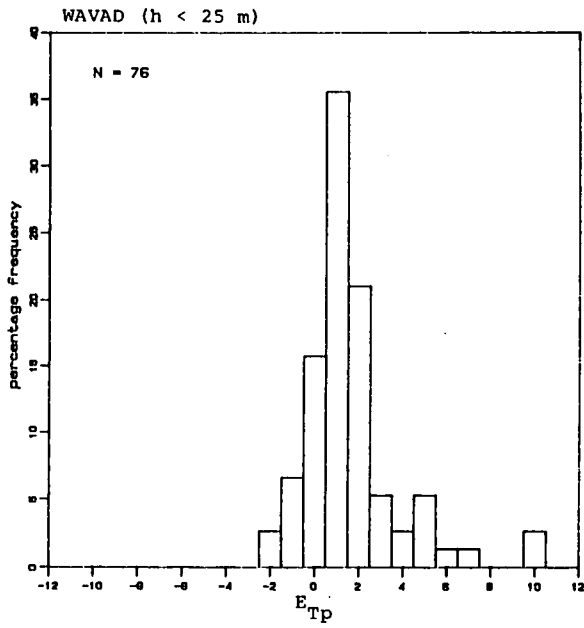


Fig. 4.12 Frequency histograms for  $E_{Tp}$ .

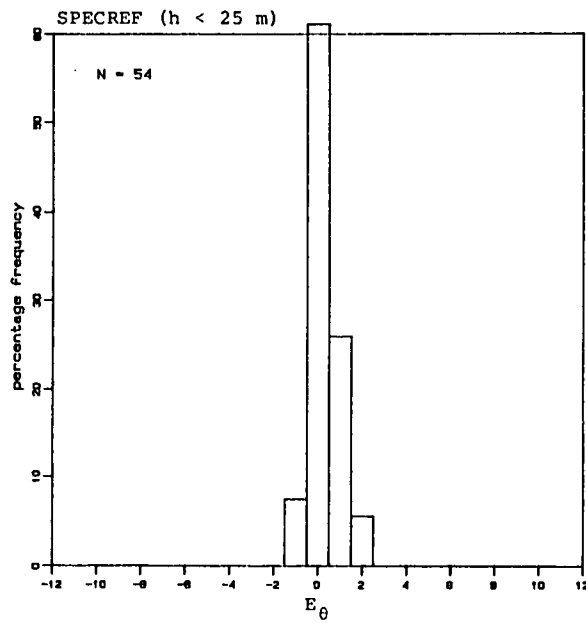
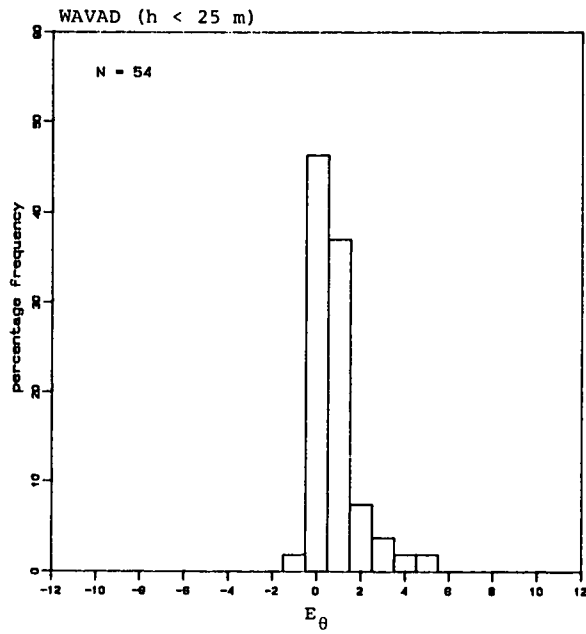


Fig. 4.13 Frequency histograms for  $E_\theta$ .

**Table 4.1**  
**Wave Model Statistical Analysis Results**

		$H_S$				$E_{Tp}$		$E_{\bar{\theta}}^{(1)}$	
		$MSE_S$	$MSE_U$	RMSE	SI	$\mu$	$\sigma$	$\mu$	$\sigma$
all data (N=139)	WAVAD	0.70	0.91	1.27	0.21	1.24	2.10	-	-
	SPECREF	0.55	0.49	1.02	0.15	0.14	1.55	-	-
h > 25 m (N=63)	WAVAD	0.56	0.82	1.17	0.18	0.78	1.91	-	-
	SPECREF	0.44	0.50	0.97	0.14	0.35	1.76	-	-
h < 25 m (N=76)	WAVAD	0.95	0.44	1.18	0.18	1.62	2.17	0.78	1.08
	SPECREF	0.74	0.42	1.08	0.17	-0.03	1.33	0.30	0.68

(1) measured peak directions available only at stations 252 and 253 (N=54)

$\mu$  = mean

$\sigma$  = standard deviation



older SOWM model) RMSE's ranging from 0.73 to 0.95 m over the NW Atlantic Ocean and 0.88 to 1.27 m over the NE Pacific Ocean with SI's of 0.28 to 0.45 depending upon the month of the year (December 1984, and January and February 1985 were examined). Thus we find that both spectral models used here, with RMSE's and SI's falling within the GSOWM ranges, are roughly equivalent in accuracy to the deep water operational model even with the added complexity of shallow water effects. It should be noted that the wind fields used with SPECREF and WAVAD were carefully hindcast, and not derived strictly from operational atmospheric diagnostic models. In principle these hindcast winds should be more accurate and this may indeed be reflected in the lower  $H_s$ -scatter indices found for the shallow water models.

As shown in Fig. 4.12, WAVAD exhibits a low bias in  $T_p (=f_p^{-1})$  with a mean error of  $1.24\Delta f \pm 2.10$  (Table 4.1). By comparison, SPECREF is essentially unbiased with a mean error of  $0.14\Delta f \pm 1.55$ . The histograms show that 82% of the  $f_p$  predictions in shallow water fall within  $\pm 1.5\Delta f$  for SPECREF, but that only 58% of the WAVAD predictions meet this same criterion.

Wave direction statistics were calculated from the 54 available data points at stations 252 and 253. Both models appear to be essentially unbiased with mean errors of  $0.78\Delta\theta \pm 1.08$  and  $0.30\Delta\theta \pm 0.68$  for WAVAD and SPECREF respectively.

The  $MSE_g$  may be interpreted as containing the systematic errors produced by model formulation whereas unsystematic errors and sample variability in measurements show up in  $MSE_u$  (Clancy et al., 1986). The systematic mean square error in  $H_s$  is found to be significantly higher in shallow water than in deep water (Table 4.1) for both models; roughly, these statistics are about two times higher in shallow water. The unsystematic error shows the opposite trend for WAVAD, and is approximately equal in deep and shallow water for SPECREF. It is difficult to give a causative explanation for these trends but we note that the values derived here, again, are bounded by the values reported for GSOWM. Generally, they also point to superior performance by WAVAD and SPECREF

compared with, for example, the original SOWM model which is a first-generation decoupled spectral model.

#### 4.2 Prediction of Spectral Shape

In terms of model performance we have found that the  $f_p$ -scaling in shallow water differs between the two models and is evident in the shallow water comparisons with measurements. Consequently, predicted spectral forms are expected to differ. Selected spectra from storms 2, 3 and 4 are compared with measurements in this section. Additional plotted spectra, in larger format, are presented in Appendices 2, 3 and 4 for reference.

Two examples of predicted and measured spectra from storm 2 are shown in Fig. 4.14 and 4.15 for the two shallow water stations (252 and 253). The spectra occur just after a wind shift to WNW near the peak of the storm and are representative of others in this event (Appendix 2). The measured energy distributions are fairly broad near  $f_p$  and energy is quite widely spread about  $\bar{\theta}(f)$ .

The WAVAD spectra show a single peak frequency with energy decreasing comparatively slowly on both the forward face and over the saturated high frequency range. The forward face predicted by WAVAD is, however, much flatter than measured. The energy spread is narrower than measured but is still reasonably representative of the natural seas allowing for a shift in  $T_p$ : most importantly the spectra  $S(f,\theta)$  show a smooth directional transition from low to high frequency.

The SPECREF results capture some of the broadening of energies about  $f_p$ . However the two-dimensional spectra  $S(f,\theta)$  exhibit a distinct step-like shape, with a narrow energy spread about the central direction in each "step". These shapes most likely result from the isolated propagation of SW swell generated earlier in the storm and westerly wind sea matched more closely to the local overwater wind direction. The step-like appearance is a consequence of the frequency-decoupled formulation (neglect of wave-wave interactions) and shows up, for example, in the mid-range of frequencies in the right-hand tail (Fig. 4.15) as an abrupt shift of energy. Such an energy jump is not consistent with the theory presented in Chapter 1 concerning an equilibrium between wind input and nonlinear fluxes to the right of  $f_p$ .

84122621 0  
station #252

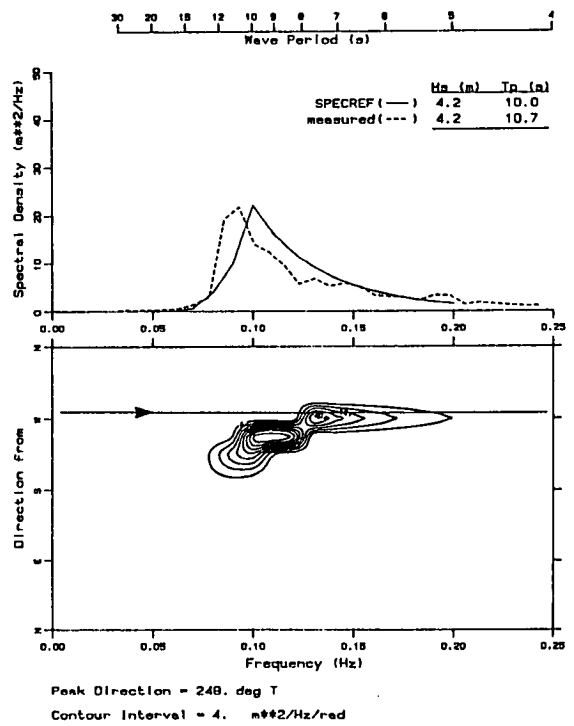
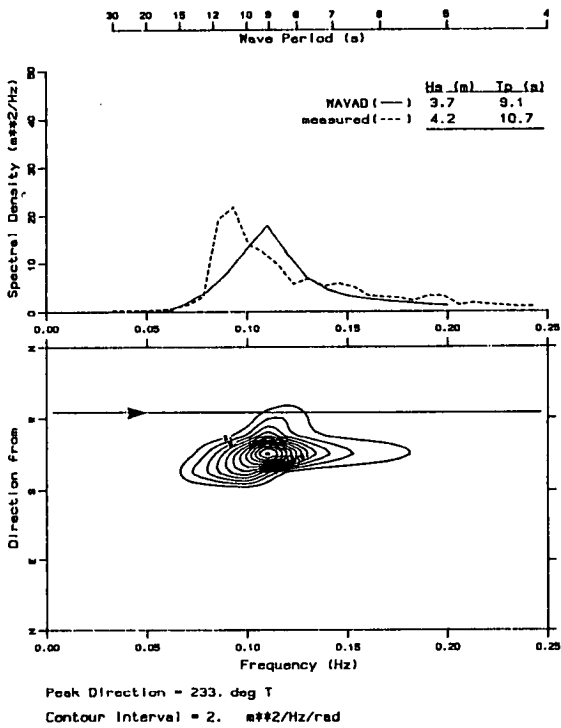
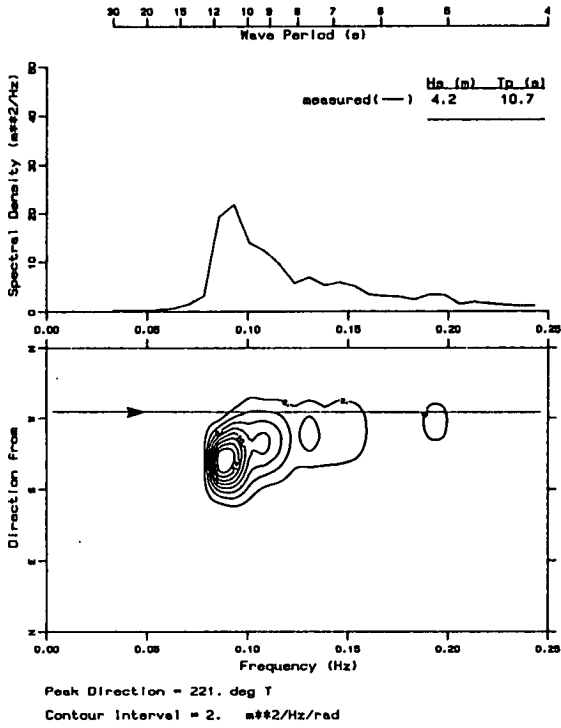


Fig. 4.14 Comparison of measured and predicted spectra in storm 2 (station 252). The arrowhead indicates wind direction.

84122621 0  
station #253

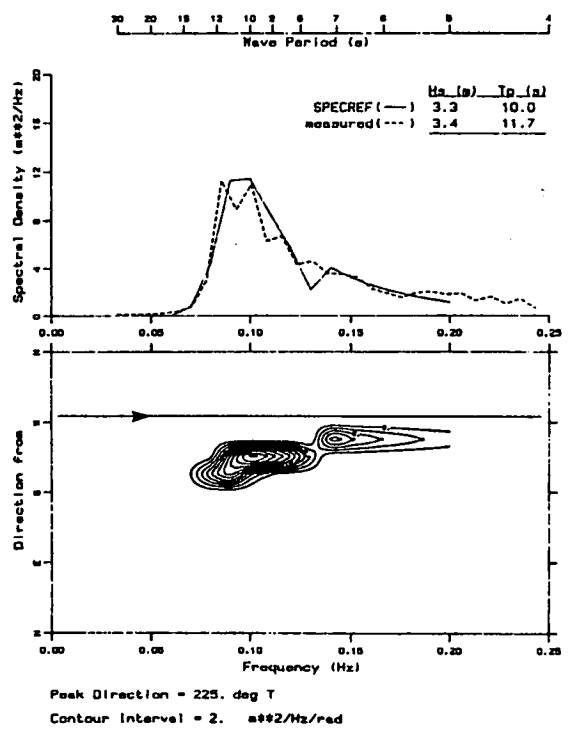
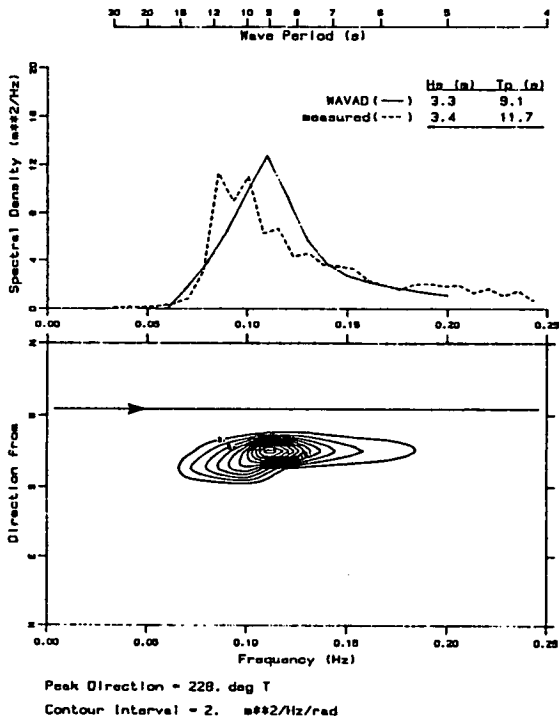
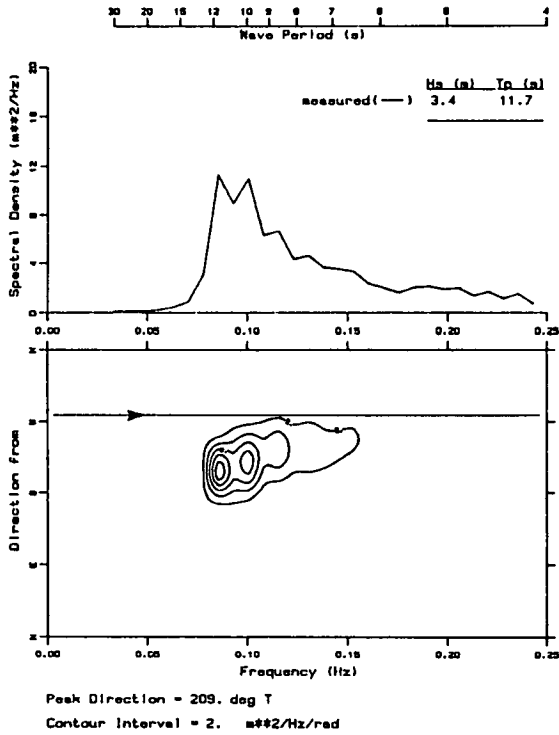


Fig. 4.15 Comparison of measured and predicted spectra in storm 2 (station 253). The arrowhead indicates wind direction.

Representative spectra from storm 3 under comparatively steady winds in the late stages of this event are shown in Fig. 4.16. In this case both wave models give an excellent reproduction of  $H_s$  and  $T_p$ . However, the same tendency noted above for WAVAD, in terms of a low forward face slope, is found here also. The shape of the forward face, position of  $T_p$ , and fit of the rear face is slightly better for SPECREF, at least on the basis of a visual comparison. Refraction effects are evident in all results although WAVAD gives a smoother directional transition with frequency than SPECREF and is in better agreement with the measurements. The SPECREF spectra again exhibit the almost discontinuous directional shifts with frequency. Both models are characterized by a narrower spread of energy than found in nature.

Two sets of spectra selected near the peak of storm 4 are presented in Fig. 4.17. As noted in the time-series comparisons, WAVAD predictions are low for both total energy and peak period, and thus the fit of the spectra is not good (see also Appendix 4). In this storm the winds are steady; both measured and WAVAD spectra exhibit no perceptible wave direction shift with frequency at 85-01-22-21. Six hours later (85-01-23-03) the measured high frequency energy lies slightly closer to the wind than the lower frequency peak. WAVAD does not reflect this change. At both times shown here, SPECREF predicts approximately a  $30^\circ$  to  $40^\circ$  shift in energy direction with higher frequencies moving toward but not onto the wind direction. The spectra also exhibit the step-like structure noted in storms 2 and 3. In this storm the SPECREF results for  $E(f)$  provide an excellent match to measured data, but as also noted above the energy spread is too narrow about the mean wave direction.

Neither model studied here shows any manifestation of finite amplitude effects giving rise to secondary peaks at  $2f_p$ . This result is consistent, however, with the use of a saturation range to the right of  $f_p$  provided that energy levels are governed by this function. The "smooth" shape of the rear face in, for example, Fig. 4.14 and 4.16 is actually the saturation form--the use of this function masks out any secondary peaks and this is one limitation common to both models.

85010712  
station #253

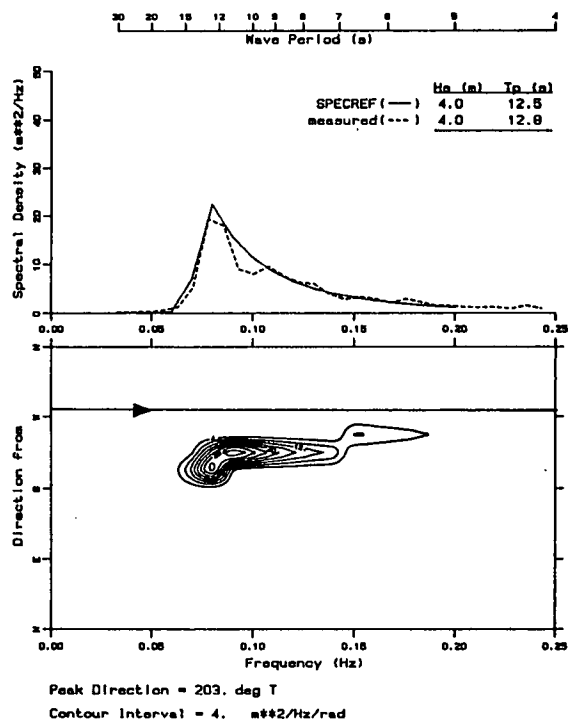
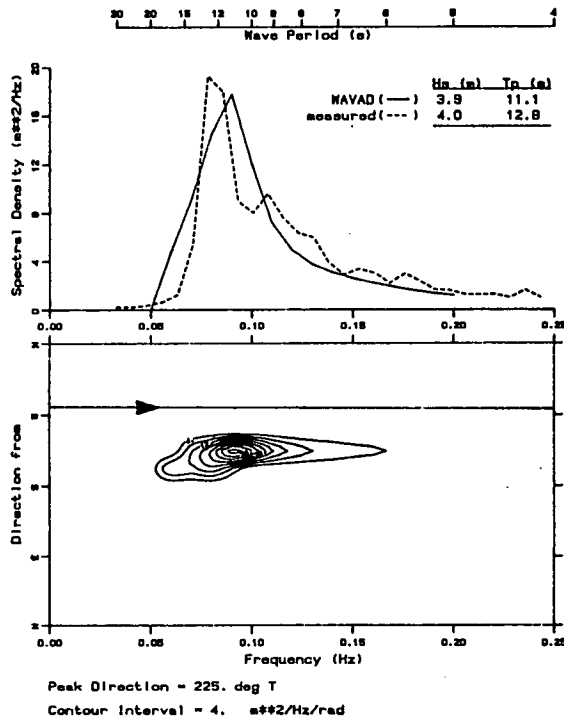
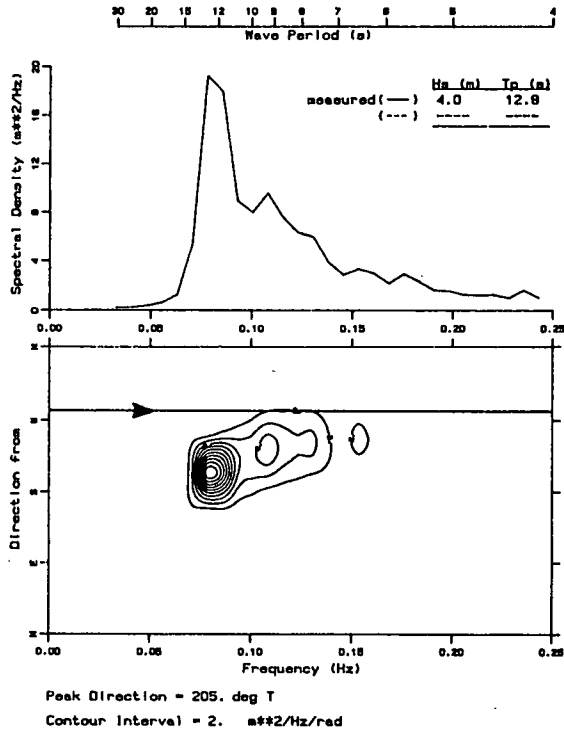


Fig. 4.16 Comparison of measured and predicted spectra in storm 3 (station 253). The arrowhead indicates wind direction.

85012221 0  
station #253

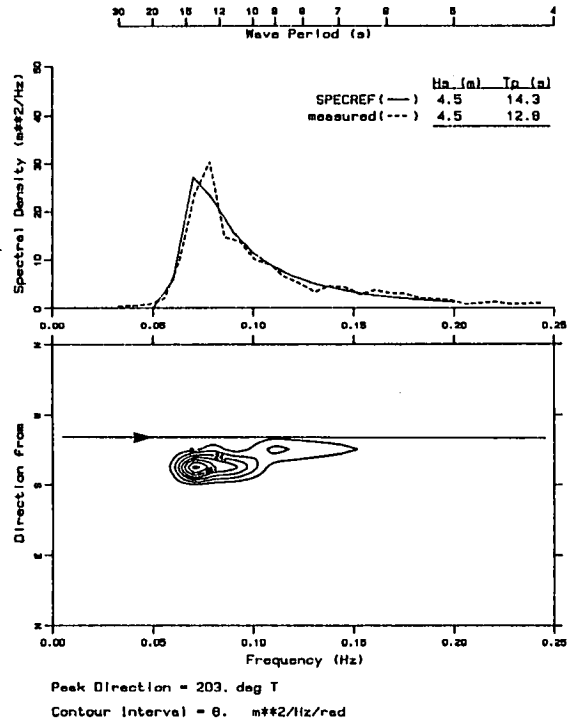
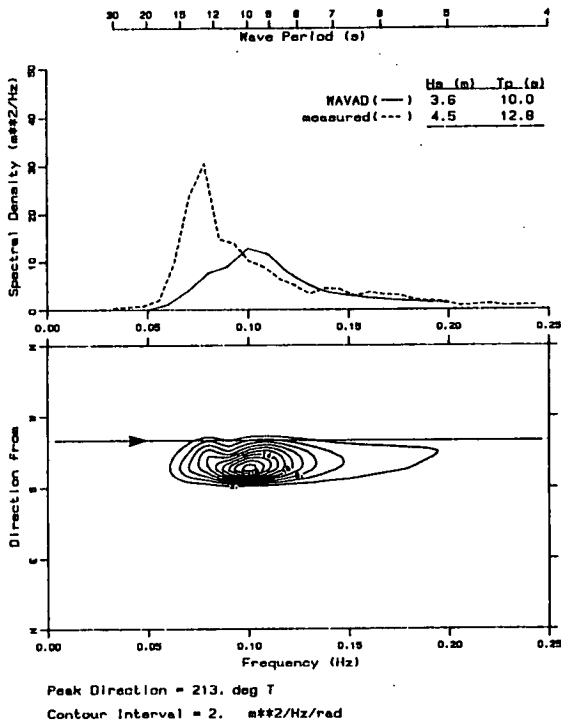
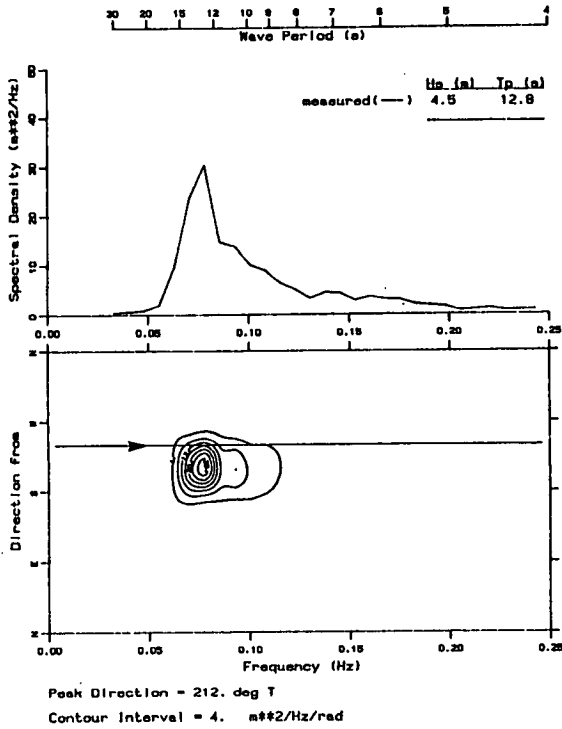


Fig. 4.17 Comparison of measured and predicted spectra in storm 4 (station 253). The arrowhead indicates wind direction.



It has been stressed earlier that the fundamental difference between WAVAD and SPECREF lies in the treatment of nonlinear fluxes produced by wave-wave interactions. Unlike WAVAD, SPECREF does not include any estimate of this energy flux. Nevertheless, one of the principal effects of these wave-wave interactions--a shape restoring tendency giving rise to self-similar spectral forms--is incorporated into SPECREF through the saturation range equation (1.4). Thus SPECREF does not rely on a sink mechanism such as bottom friction to limit the growth of energy on the rear face of the spectrum. Friction is able to affect the energy content of the front face, however, and it is of interest to examine the sensitivity of results to changes in the bottom friction coefficient. Similarly it has been noted above that the wind source term is important in the transformation process. The influence of these two terms is examined in the following section using the SPECREF model. We note that the results described above were obtained with wind input but no bottom friction.

### 4.3 Sensitivity to Wind Input and Bottom Friction

The influence of the wind source term was investigated by rerunning storm 2 using only the spectral boundary conditions for input, and comparing  $H_s$ ,  $T_p$  and  $\bar{\theta}$  with the full simulation including wind. These results (Fig. 4.18) show that ashore to a certain water depth the wind source term is crucially important to maintaining enough energy in the wave field. Traditional refraction analyses that neglect wind input for rays more than a few kilometres long will almost certainly fail to model  $H_s$  well.  $T_p$  and  $\bar{\theta}$  are less sensitive to wind than  $H_s$ ; rather, they are dominated by their incident values on the boundary, and by refraction in the case of  $\bar{\theta}$ .

Shoreward of a certain depth, which depends on the wind history in a given storm and the wind speed and direction at the time of interest, the saturated form will largely govern the total energy content and the shape of the rear spectral face. In these depths the wind source term itself plays a negligible role: the energy tends to be maintained up to the saturated level by propagation from deeper into shallower water. Thus we find that the influence of wind growth on  $H_s$  at station 253 in 12 m of water is almost nil, while still of great importance at both gauge sites in deeper water (Fig. 4.18).

Bottom friction was examined using two forcing wind conditions and two bounding values for the bottom friction coefficient,  $C_f$  at four measurement times in storm 2 (84-12-26-18; 84-12-26-21; 84-12-27-00; 84-12-27-03). Significant wave heights averaged about 3.7 to 4.5 m at stations 253 and 252 respectively. The cases considered were:

<u>U(m/s)</u>	<u>0</u>	<u>20</u>	<u>20</u>	<u>20</u>
<u><math>C_f</math></u>	<u>0</u>	<u>0</u>	<u>0.005</u>	<u>0.01</u>

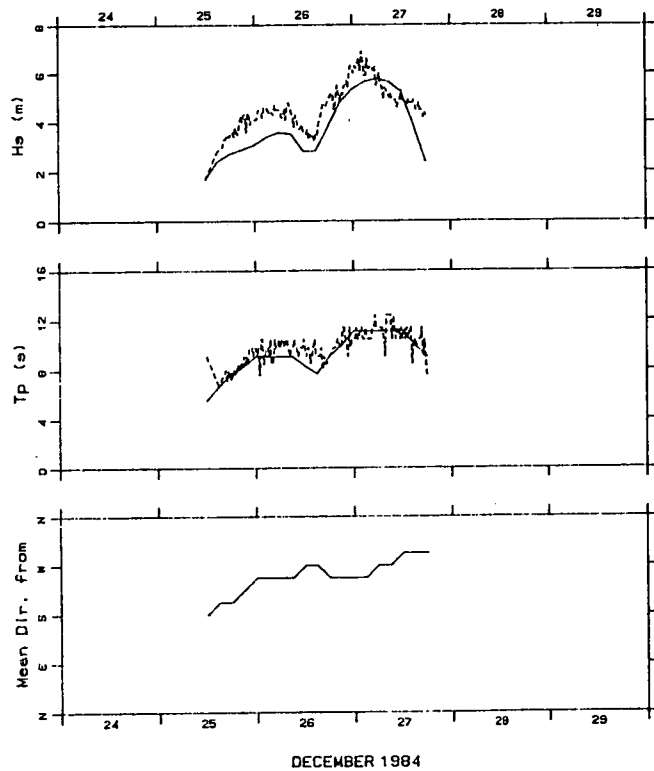
These values for  $C_f$  bound those presented by Shemdin et al. (1977) for fine sands.

The results of transforming  $H_s$  under these four sets of conditions are summarized in Table 4.2. We find that for zero wind and zero friction, predictions are systematically low by about 15% of the measured value.

Storm #2 - Stn. 133

(no wind)

—— SPECREF  
----- Measured



Storm #2 - Stn. 133

—— SPECREF  
----- Measured

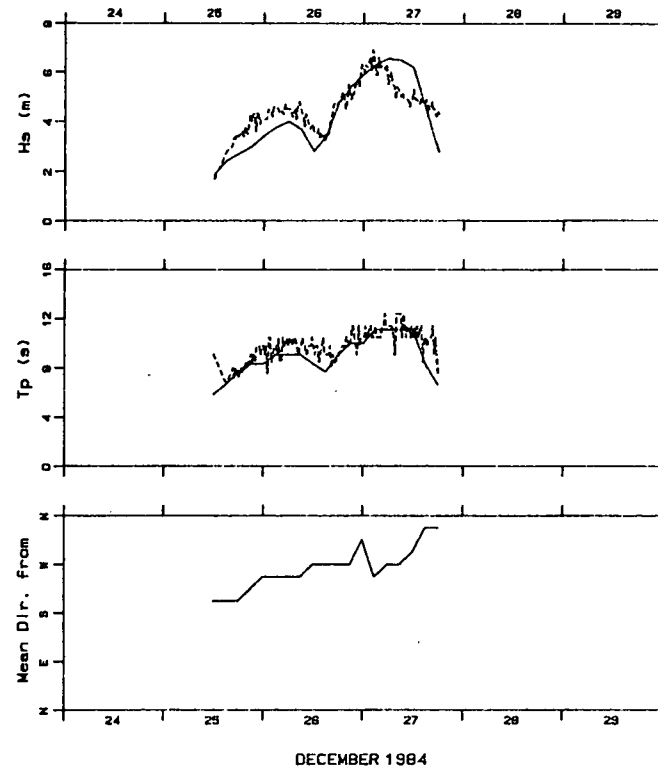
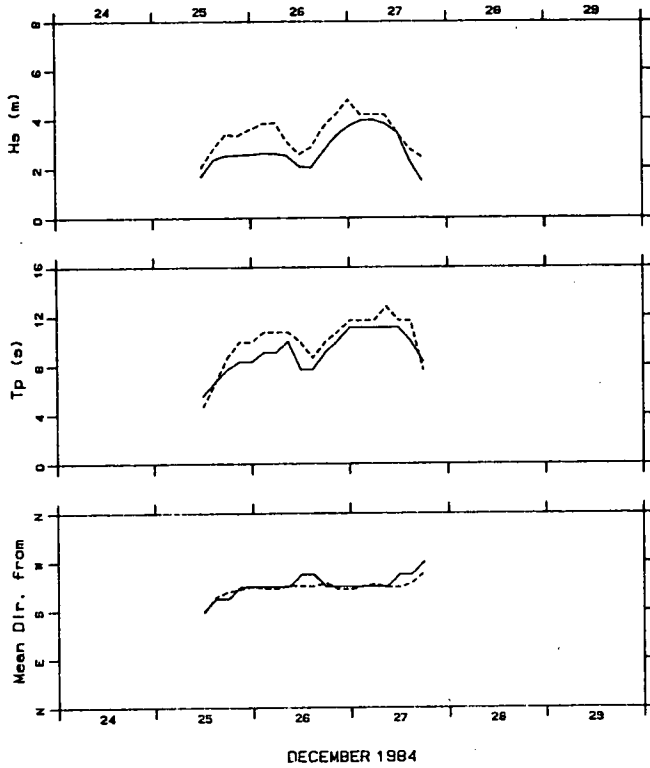


Fig. 4.18a Comparison of predicted and measured wave parameters with wind input (right) and without wind input (left) at station 133.

Storm #2 - Stn. 252

(no wind)

— SPECREF  
- - - Measured



Storm #2 - Stn. 252

— SPECREF  
- - - Measured

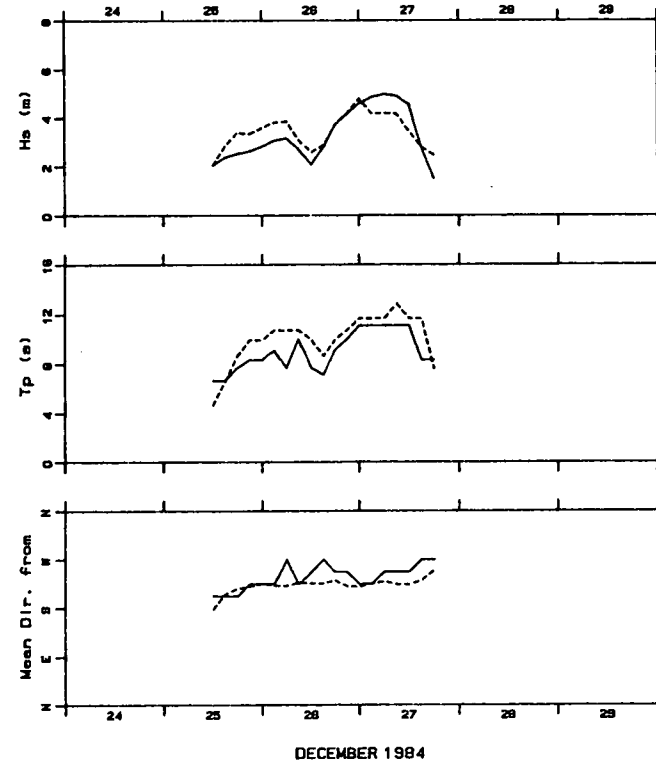


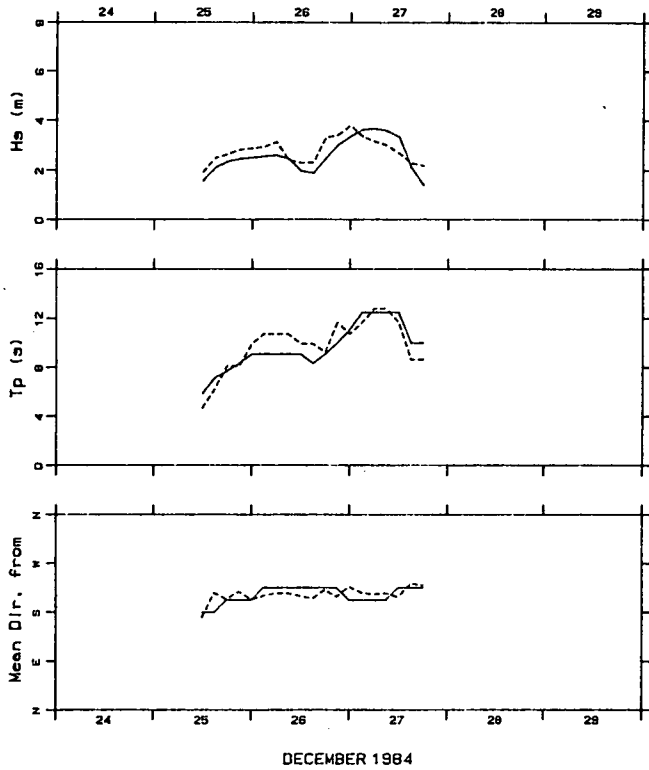
Fig. 4.18b

Comparison of predicted and measured wave parameters with wind input (right) and without wind input (left) at station 252.

Storm #2 - Stn. 253

(no wind)

— SPECREF  
- - - Measured



Storm #2 - Stn. 253

— SPECREF  
- - - Measured

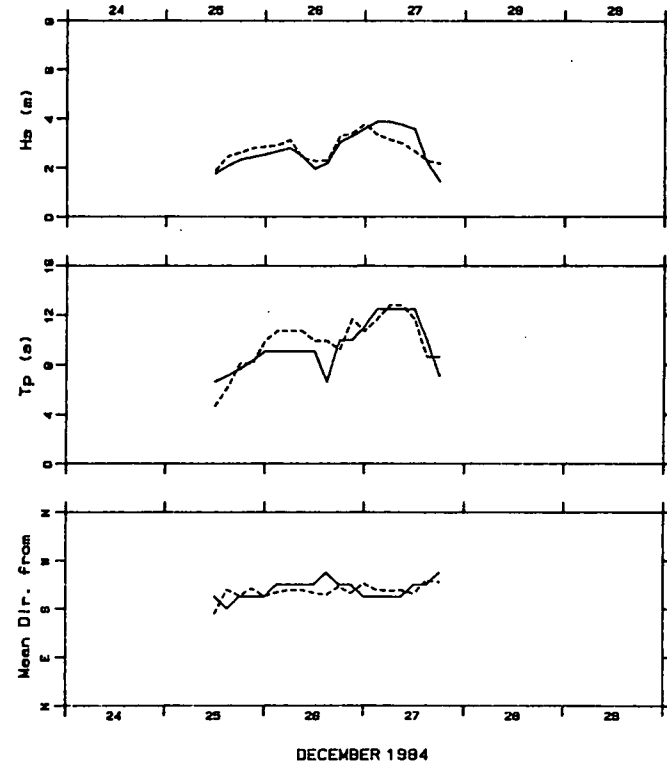


Fig. 4.18c Comparison of predicted and measured wave parameters with wind input (right) and without wind input (left) at station 253.

Table 4.2

**Comparison of Measured and Predicted  $H_s$  for  
Various Wind and Bottom Friction Conditions**

Station	Date	Time	[ $H_s$ (pred.) - $H_s$ (measured)] / $H_s$ (measured) x 100%			
			U=0 m/s $C_f=0$	U=20 m/s $C_f=0$	U=20 m/s $C_f=0.005$	U=20 m/s $C_f=0.01$
252	84-12-26	18:00	-27	0	-1	-1
		21:00	-21	-1	-2	-4
252	84-12-27	00:00	-23	-4	-6	-10
		03:00	-6	16	13	7
253	84-12-26	18:00	-25	-7	-8	-10
		21:00	-12	-3	-8	-10
253	84-12-27	00:00	-12	-5	-9	-10
		03:00	8	16	11	8
Averages			-14.8	+1.5	-1.3	-3.8

Adding wind but keeping  $C_f = 0$ , brings the station 252 ( $h = 22$  m) results into better agreement (+1.5% averaged over all 8 data points although the 16% overestimate at both sites at 03 GMT on December 27th likely reflects a boundary condition difference rather than the result of changes to the source-sink terms). Adding low and high friction into the transformation lowers the results, as expected. Averaged over the 8 points,  $C_f = 0.005$  produces a change of 2.8% from the wind only run and  $C_f = 0.01$  yields an average change of 5.3%. Two aspects of these changes are important: first, even at the highest reasonable friction coefficient, the percentage change is about one-third of the beneficial change made by incorporating the wind source term, and second, incorporating friction actually degrades the model performance. Moreover, we note that the average changes due to friction are well within the uncertainty in  $H_s$  due to sampling variability.

Thus, it is concluded that under strong wind forcing the sink term due to bottom friction is of secondary importance. This result does not hold for all wave transformations: swell transformation under conditions of weak or no wind will be governed to a greater extent by bottom friction and shoaling than the energetic wind-seas examined here. This hypothesis is borne out by the WAVAD calculations given in Resio (1988).

#### **4.4 Sensitivity to Bathymetric Resolution**

The intercomparison results discussed above were generated on two different grid resolutions, 1 n.m. for SPECREF and 5 n.m. for WAVAD. To illustrate the behaviour of WAVAD for differing bottom resolutions, storm 2 was rerun on the 1 n.m. grid. The wind input and boundary conditions were identical with those applied to the actual storm hindcast for both models discussed previously.

The results in terms of  $H_s$ ,  $T_p$ , and direction are shown in Fig. 4.19. The peak periods are virtually identical as would be expected since they are interpolated from the values on the boundary of the shallow water domain. The small differences result from the slightly different weights in the interpolating functions due to the change in grid spacing and in grid points relative to the boundary. Significant wave heights are in good agreement for both grid resolutions. During the second maximum on December 26/27, heights from the 1 n.m. grid lie slightly above those from the 5 n.m. grid at station 252, and vice versa at station 253. These small differences result from the fact that the output points in the two grids had slightly different depths and are located at different distances out from the island barrier (null points in the wave model land/sea mask) and the open sea boundaries.

Wave directions are also in good agreement except for the first 6 hours modelled, and near the end of the time-series. Late in this storm, winds had shifted to the northwest and the wave energy was abating in concert with falling wind speeds. WAVAD predicts a sudden shift to northwesterly waves at the shallow sites. This shift is delayed in the 1 n.m. grid solutions, and reduced at station 252 (in 22 m of water). The measurements show that neither solution is realistic here: this discrepancy results from incorrect sheltering by Sable Island as resolved in either grid. This problem worsens closer to the island.

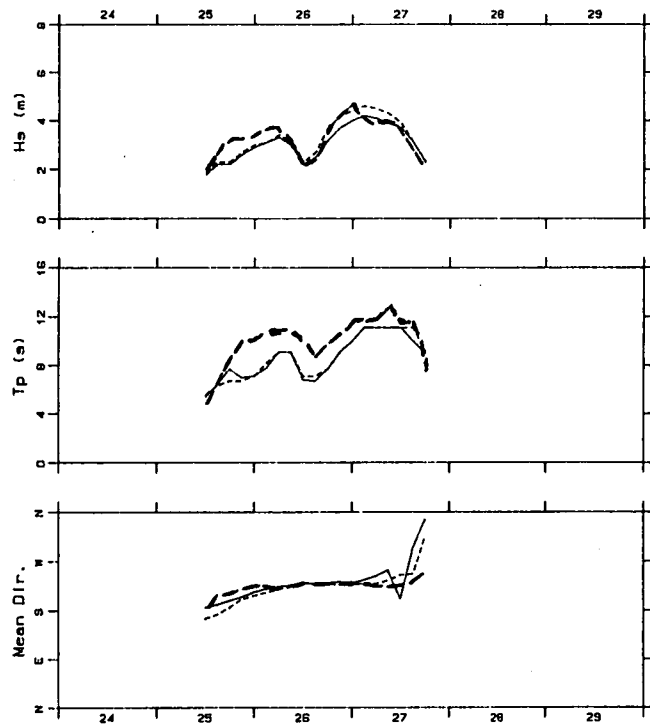
Two examples of one-dimensional spectra are shown in Fig. 4.20, together with the measured spectra. Additional spectra are presented in Appendix 5. These comparisons show that there are small differences in predicted energy levels, which are reflected in the  $H_s$ -differences noted above,



Storm 2

(Station 252)

— 5 nm grid  
- - - 1 nm grid

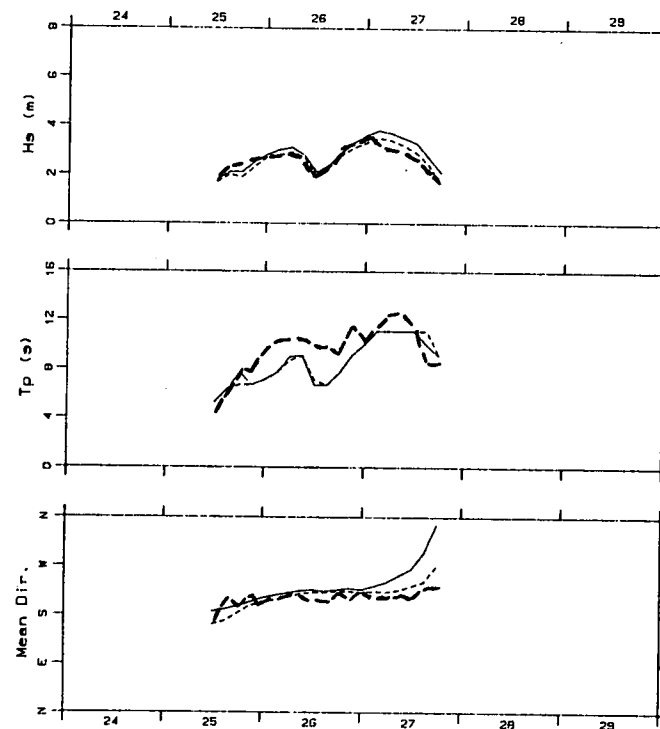


DECEMBER 1984

Storm 2

(Station 253)

— 5 nm grid  
- - - 1 nm grid

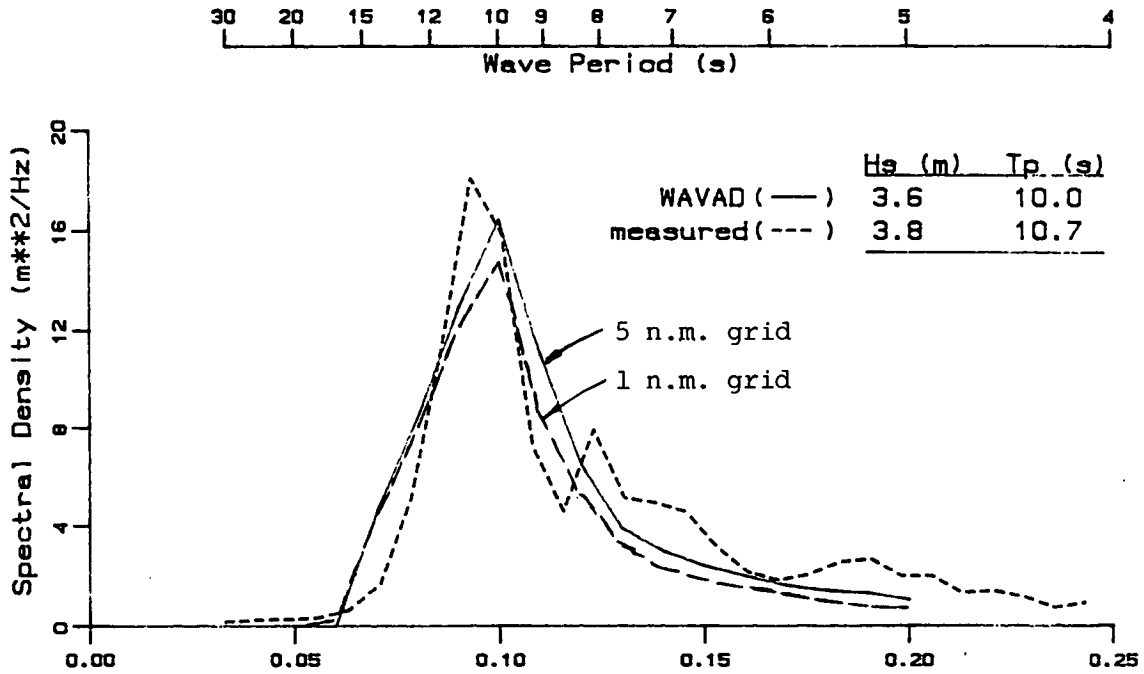


DECEMBER 1984

- - - measurements

Fig. 4.19 Comparison of WAVAD results for storm 2 modelled on the 1 n.m. and the 5 n.m. grids.

84122700  
station #253



station #252

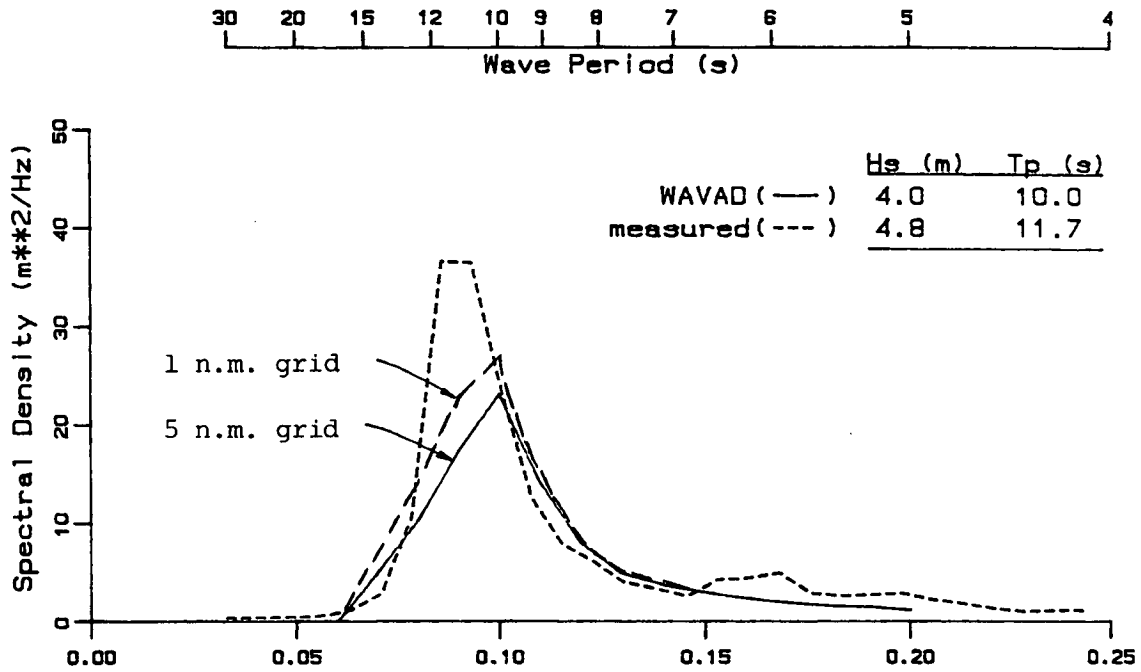


Fig. 4.20 Comparison of 1-dimensional spectra from WAVAD modelled on the 1 n.m. and the 5 n.m. grid.

but that the overall shape of the spectra remains the same.

Comparison of model results with measurements illustrates that the predictions show no clear improvement through increased resolution on the 1 n.m. grid. At times the finer grid results are in better agreement with measurements, yet at other times wave heights and particularly directions are better modelled on the 5 n.m. grid. In any event, the differences between grid resolutions are explicable in terms of small deviations in the  $h(\mathbf{x})$  fields at the output points, and are not due to a fundamental difference in representing the spectral energy balance, particularly the influence of bathymetric refraction.

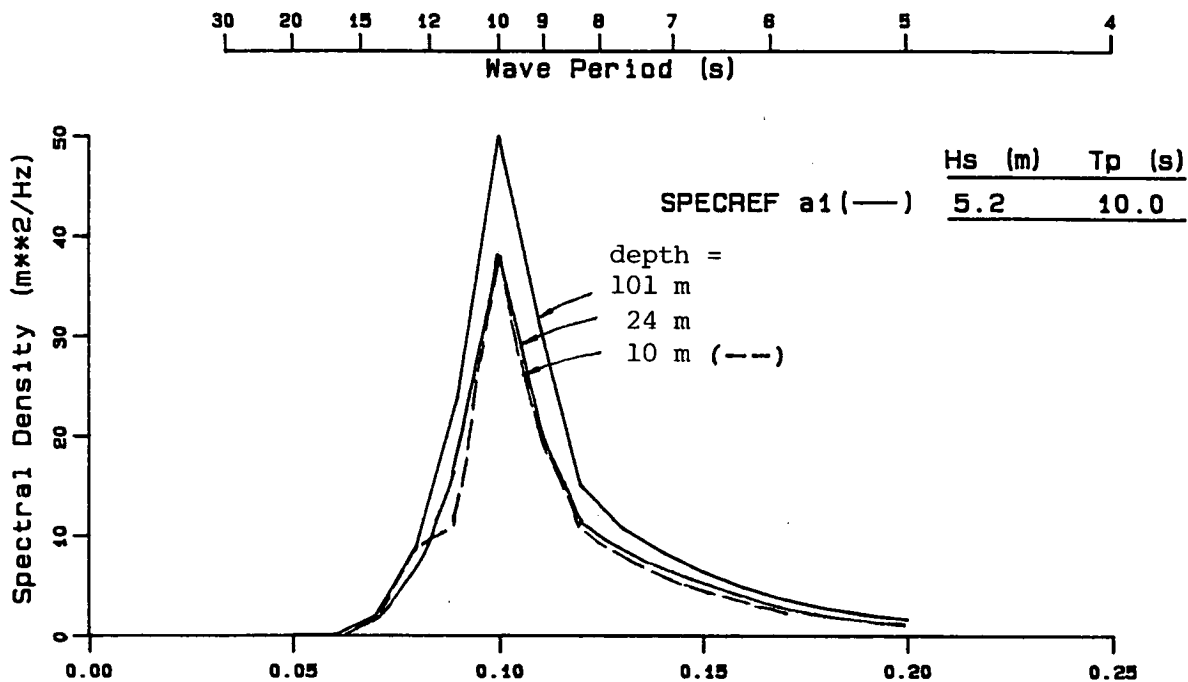
#### **4.5 Idealized Test Results**

The purpose of these tests was to illustrate differences between the model predictions for wave propagation without the influence of the wind source term, and for the condition of strong wind-wave generation across the direction of wave travel. We consider first the model behaviour in the absence of wind. Figure 4.21 illustrates 1-dimensional spectra at decreasing water depths computed by SPECREF and WAVAD for test A1 (Table 3.1). There is clearly a major difference in model behaviour for these wave conditions: WAVAD predicts a continuous loss of wave energy, distributed across all frequencies, as spectra are calculated from deep into shallow water. On the other hand, SPECREF predicts a much smaller decrease in total wave energy, right into 10 m of water. Significant wave heights along the transect are shown in Table 4.3. WAVAD predicts a 41% decrease in total energy from deep to shallow water compared with a 15% decrease in SPECREF. The peak periods and wave directions are unchanged along the transect. In each model simulation the spectra represent a balance between the saturated form governing the dissipation region to the right of  $f_p$ , and the effects of refraction and shoaling near and to the left of  $f_p$ . WAVAD differs from SPECREF in that it also provides for a transfer of energy from central frequencies to the forward face of the spectrum; however, in these calculations the exact balance between these different source terms has not been evaluated.

In a test of this nature the correct forms of spectra at different water depths are unknown, but we have seen in the hindcast of storm 4 for steady wind conditions that WAVAD overestimated dissipation compared with the source term balance in SPECREF, and consequently underestimated the significant wave heights.

In test A2 a wind of 40 knots from the west was imposed over the wave calculation domain. The results are presented in a series of companion 1- and 2-dimensional spectral plots, where the first graph shows spectra for the zero-wind condition, followed by the equivalent spectra with wind input. The results for SPECREF are shown in Fig. 4.22, followed by those for WAVAD in Fig. 4.23, omitting grid point (31,8) in the latter figure since there was no difference evident. The complete set of

at grid point (31.00, 8.00)



at grid point (31.00, 8.00)

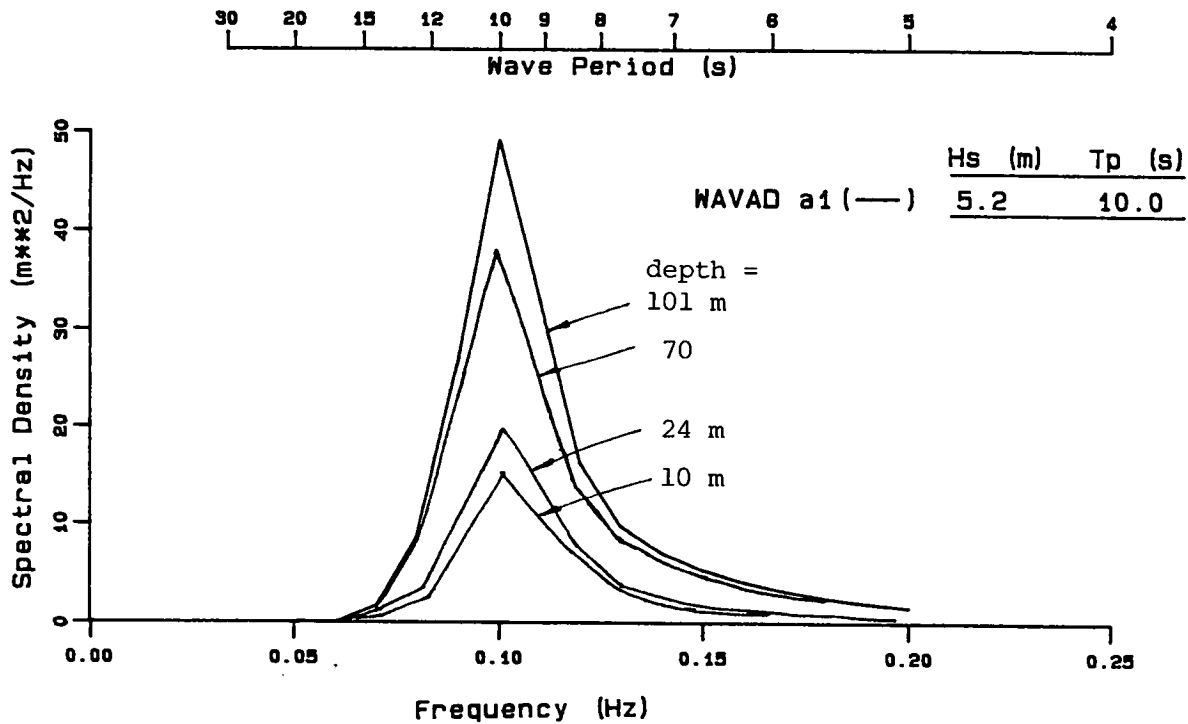
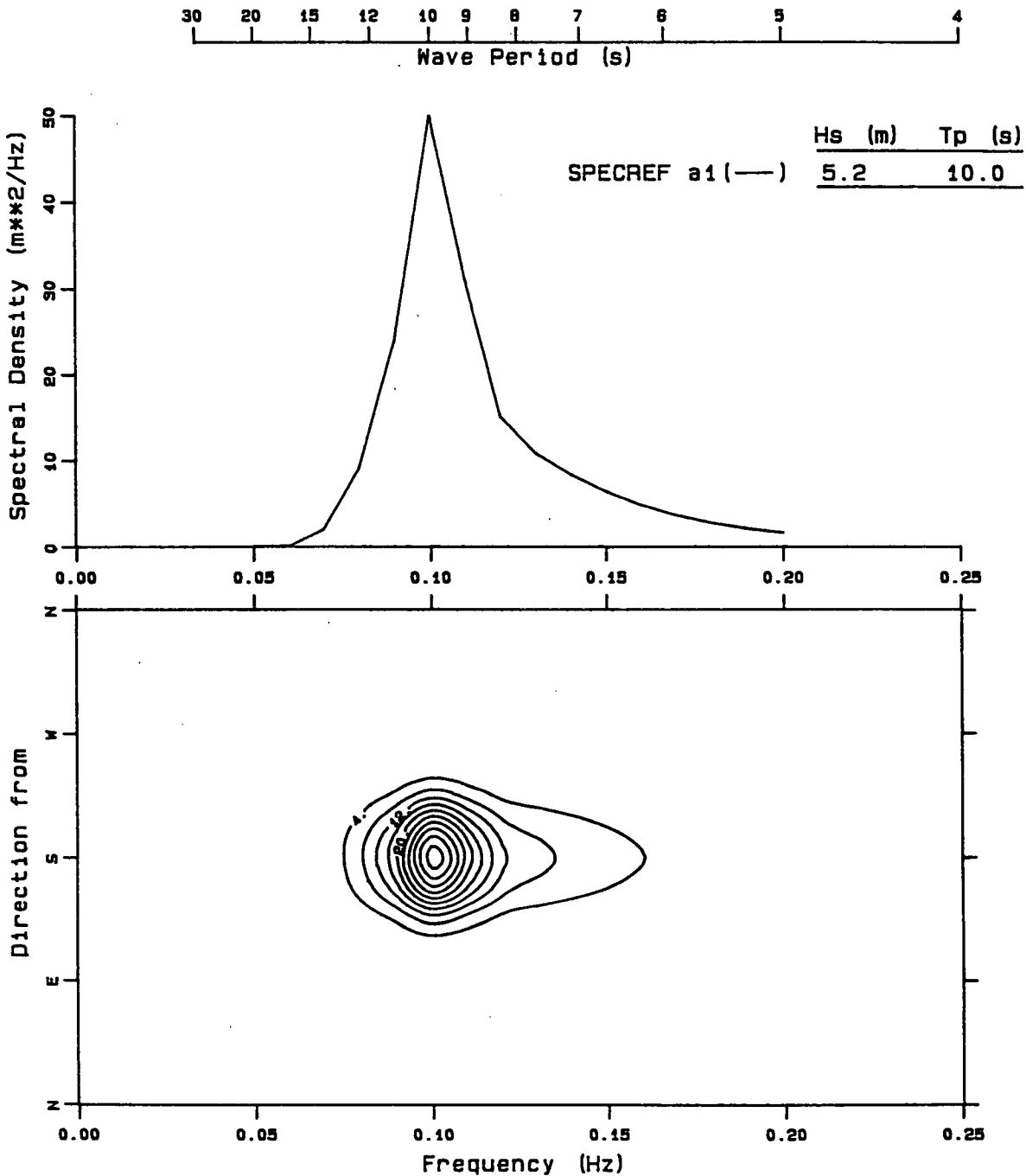


Fig. 4.21 Comparison of spectra at different water depths for idealized test A1.

**Table 4.3**  
**Comparison of Significant Wave Heights**  
**for the Idealized Test Cases**

SPECREF					
Case Point	h	A.1 $H_S$	A.2 $H_S$	B.1 $H_S$	B.2 $H_S$
1	101	5.24	5.33	7.54	7.86
2	70	5.17	5.32	7.23	7.56
3	61	5.13	5.30	6.98	7.32
4	57	5.10	5.28	6.81	7.15
5	53	5.07	5.26	6.66	7.01
6	50	5.07	5.27	6.60	6.95
7	40	4.98	5.22	6.50	6.85
8	34	4.87	5.22	6.52	6.86
9	29	4.74	5.06	6.79	7.11
10	24	4.58	4.91	5.84	6.22
11	10	4.46	4.75	4.69	4.92
$T_p$		10	10	16.67	16.67
$\theta_p$		180	180	180	180
WAVAD					
1	101	5.23	5.23	7.51	7.82
2	70	4.58	4.59	7.32	7.63
3	61	4.34	4.36	7.30	7.60
4	57	4.10	4.13	7.04	7.33
5	53	3.87	3.92	6.62	6.82
6	50	3.76	3.82	6.31	6.54
7	40	3.53	3.60	6.02	6.31
8	34	3.44	3.52	6.00	6.24
9	29	3.32	3.40	5.90	6.13
10	24	3.33	3.42	5.82	6.00
11	10	3.06	3.13	4.93	5.12
$T_p$		10	10	16.67	16.67
$\theta_p$		180	180	180	180

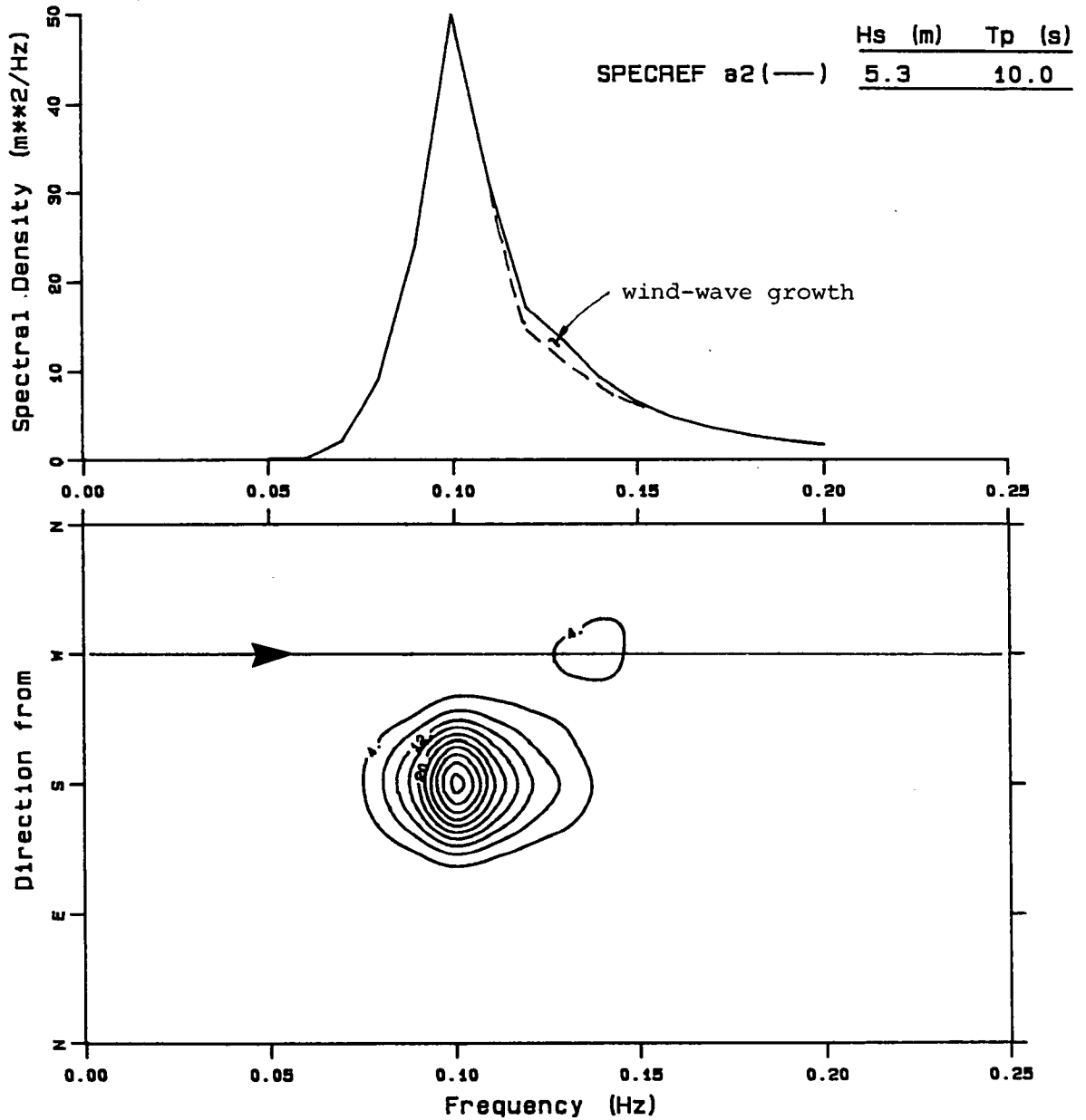
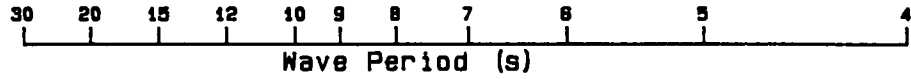
89062300 0  
at grid point (31.00, 8.00)



Peak Direction = 180. degrees True  
Contour Interval = 4.  $m^2/Hz/rad$

Fig. 4.22 Spectra computed by SPECREF for various water depths with and without wind (A1 versus A2).

89062300 0  
at grid point (31.00, 8.00)

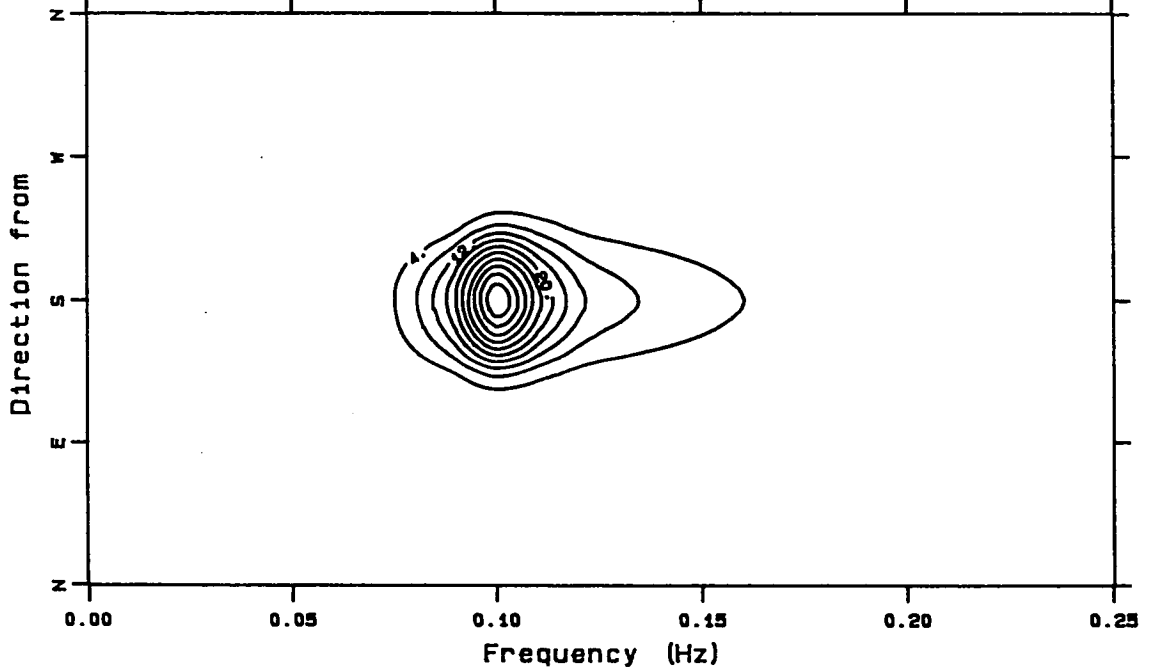
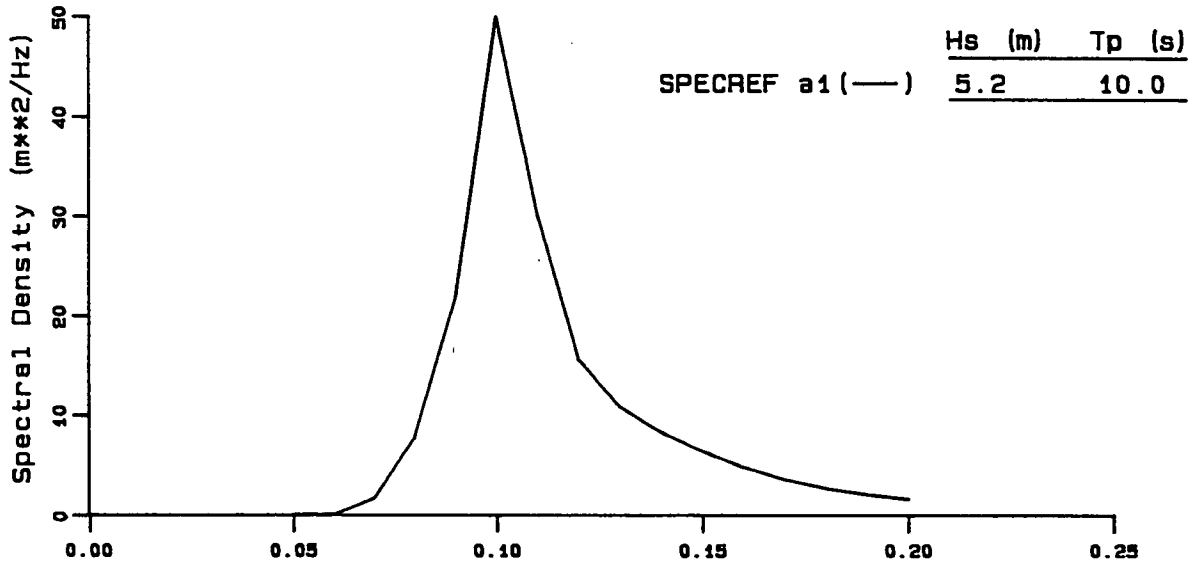
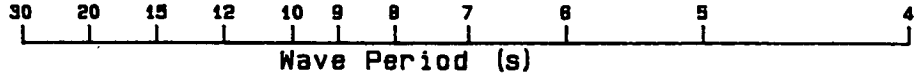


Peak Direction = 180. degrees True  
Contour Interval = 4.  $m^2/Hz/rad$

Fig. 4.22 Continued.



89062300 0  
at grid point (31.00, 12.00)

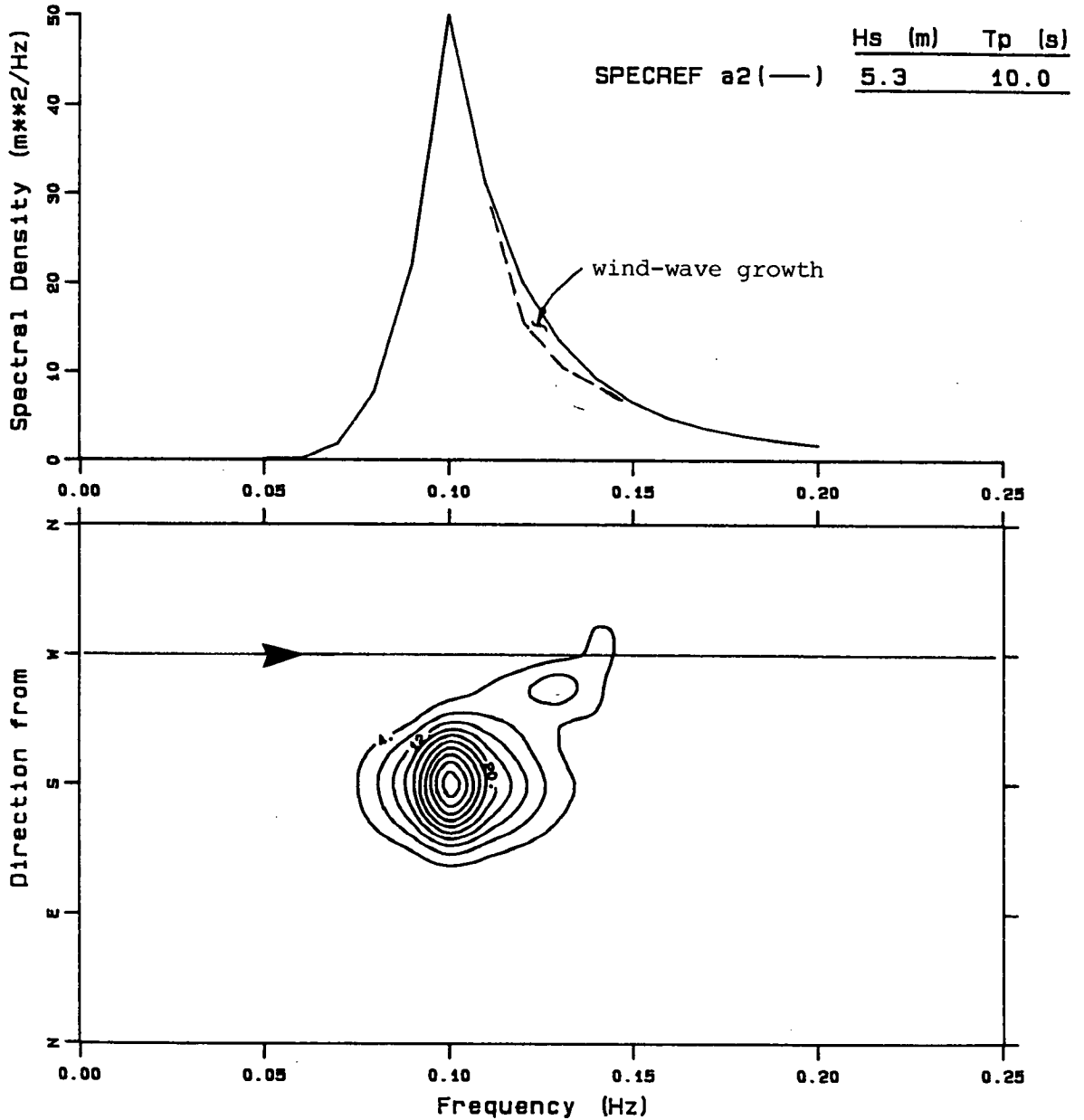
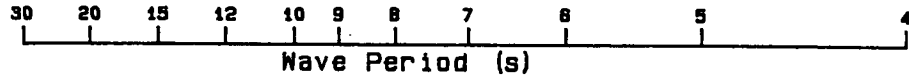


Peak Direction = 180. degrees True  
Contour Interval = 4. m<sup>2</sup>/Hz/rad

Fig. 4.22 Continued.

89062300 0

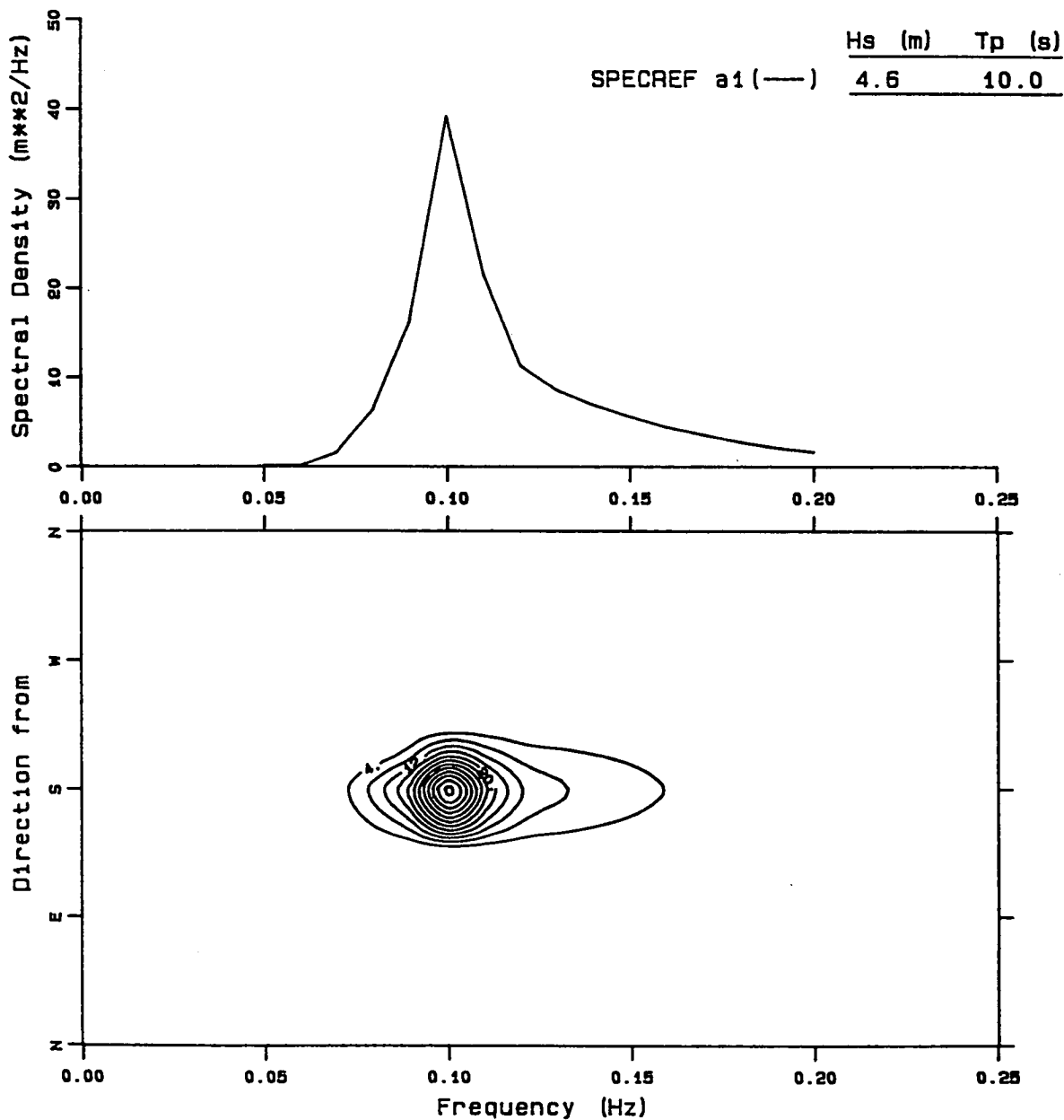
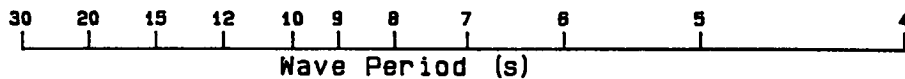
at grid point (31.00, 12.00)



Peak Direction = 180. degrees True  
Contour Interval = 4.  $m^2/Hz/rad$

Fig. 4.22 Continued.

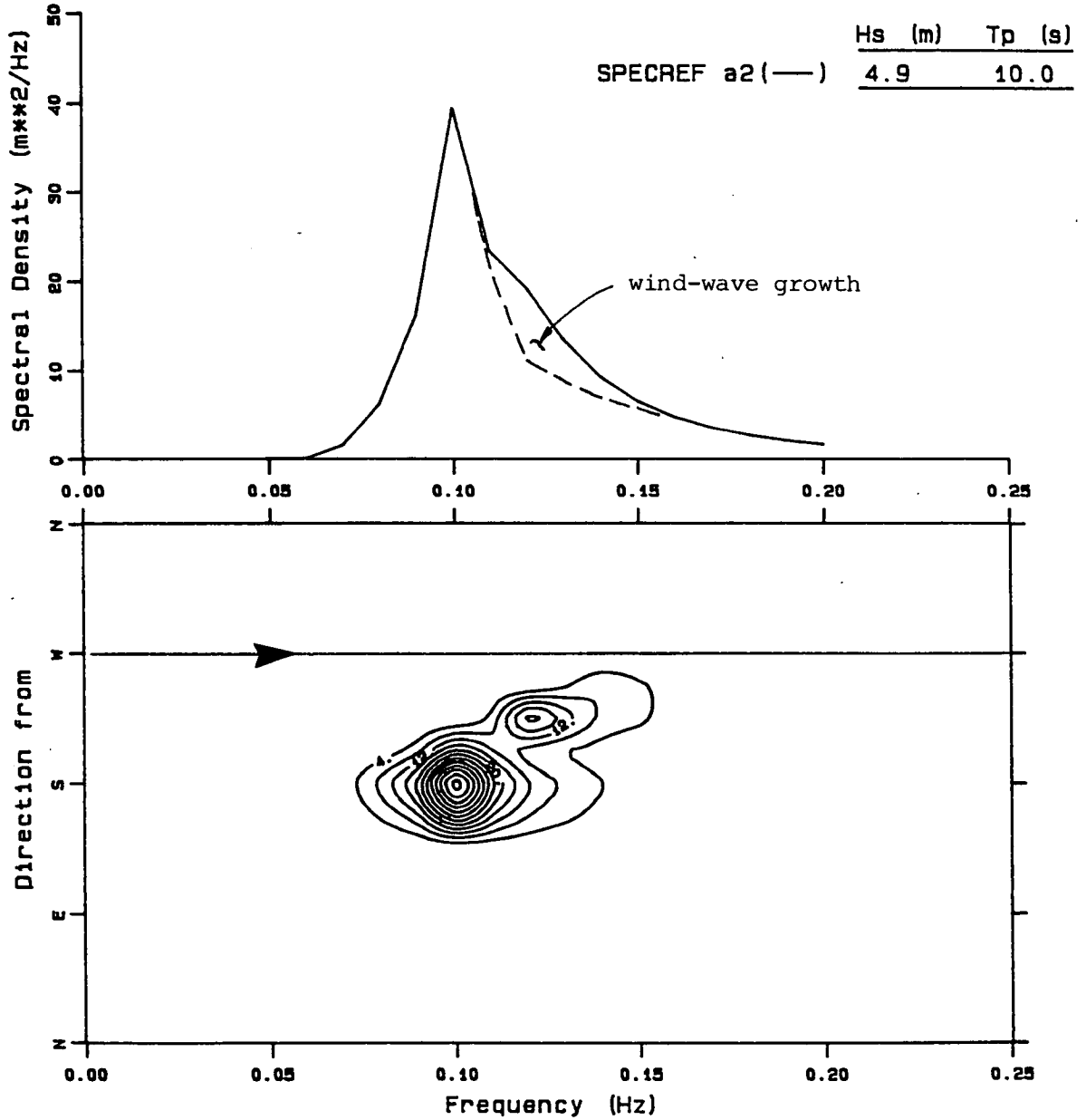
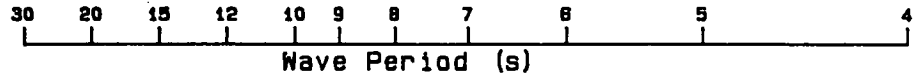
89062300 0  
at grid point (31.00, 25.00)



Peak Direction = 180. degrees True  
Contour Interval = 4. m<sup>2</sup>/Hz/rad

Fig. 4.22 Continued.

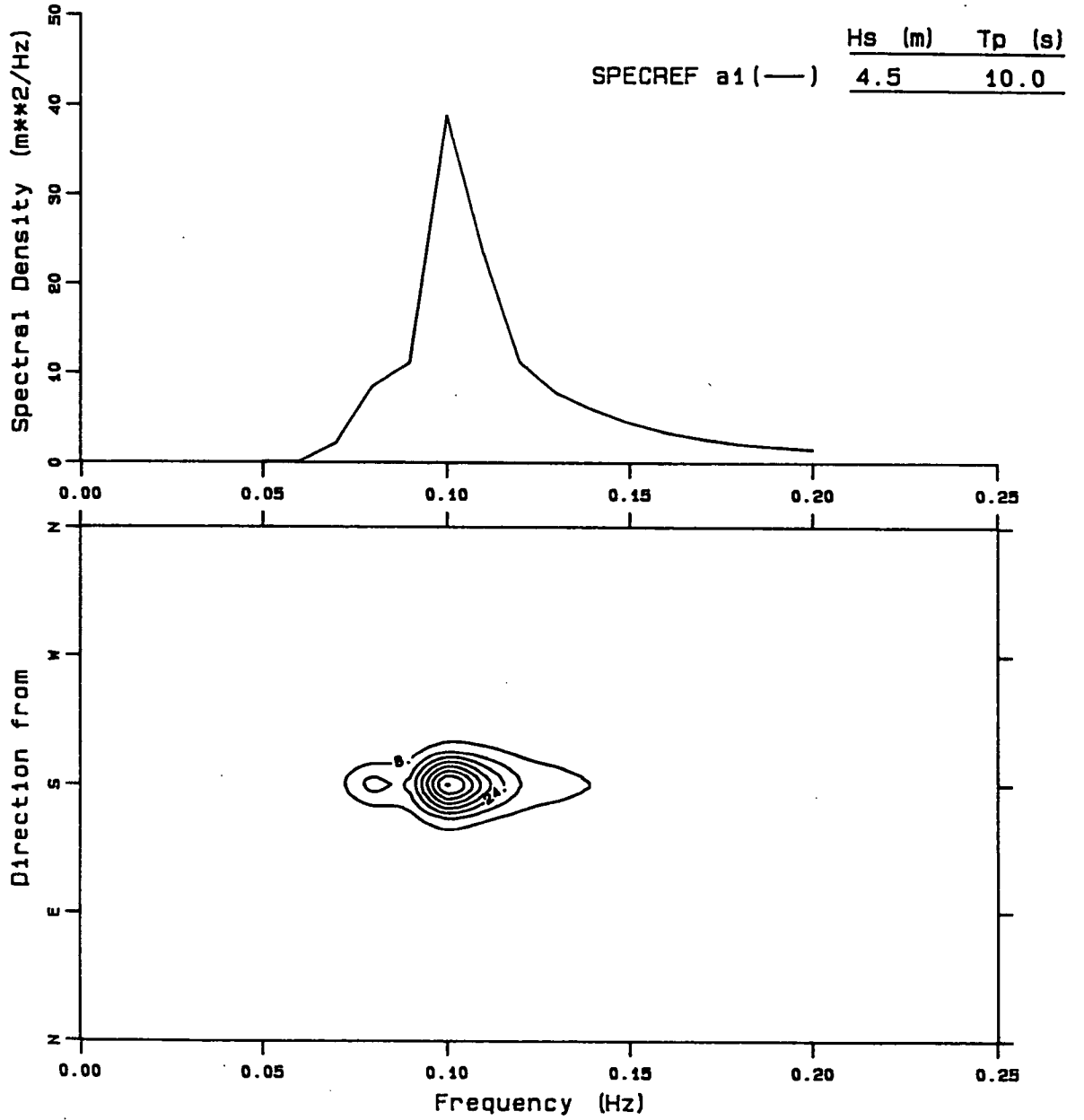
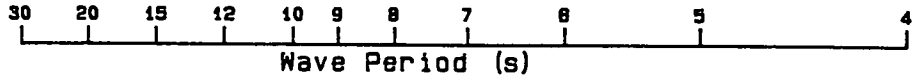
89062300 0  
at grid point (31.00, 25.00)



Peak Direction = 180. degrees True  
Contour Interval = 4.  $m^2/Hz/rad$

Fig. 4.22 Continued.

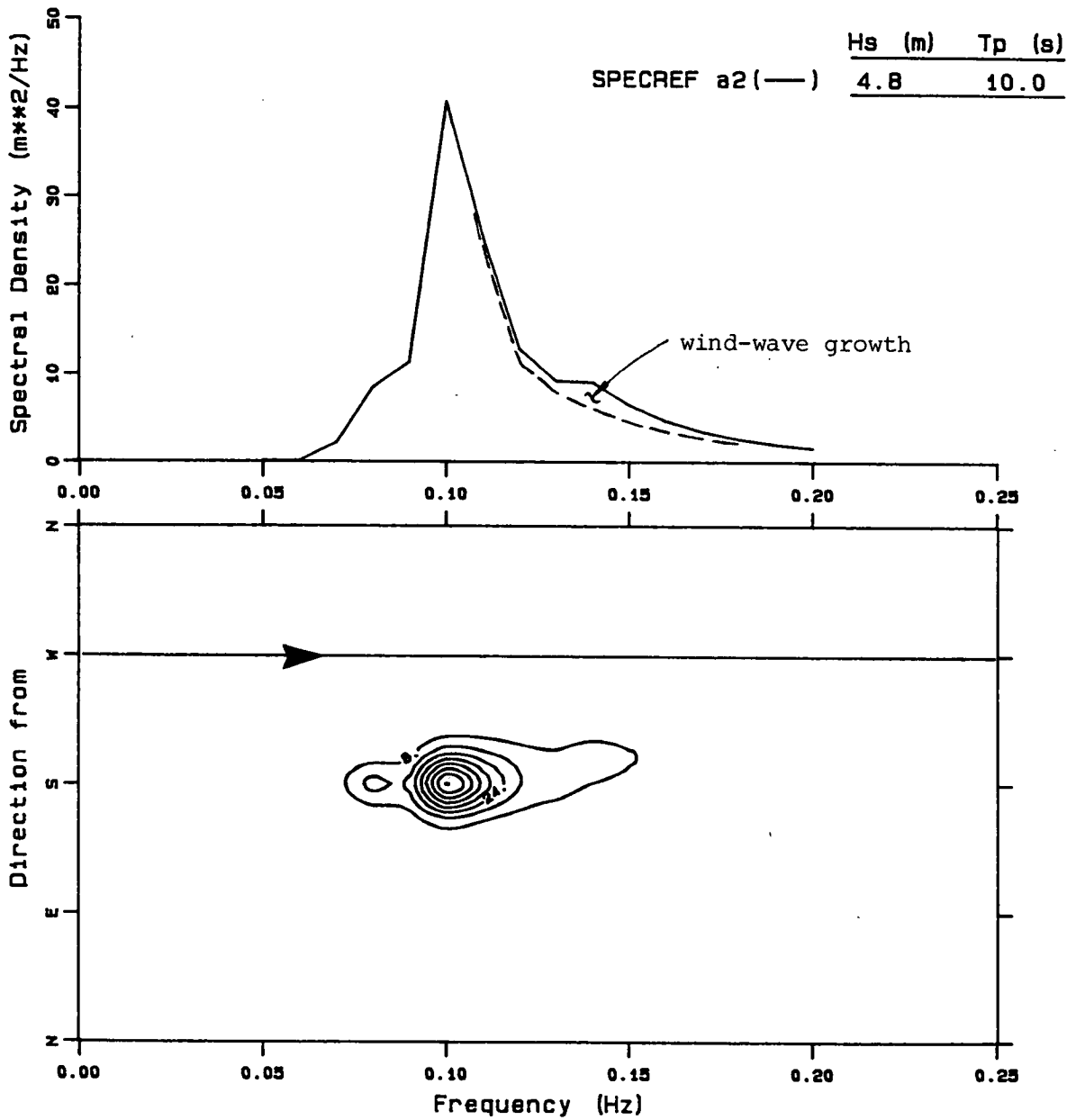
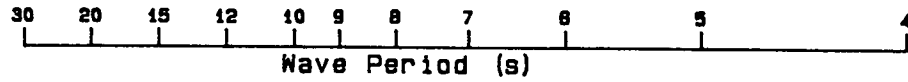
89062300 0  
at grid point (31.00, 26.00)



Peak Direction = 180. degrees True  
Contour Interval = 8.  $m^2/Hz/rad$

Fig. 4.22 Continued.

89062300 0  
at grid point (31.00, 26.00)

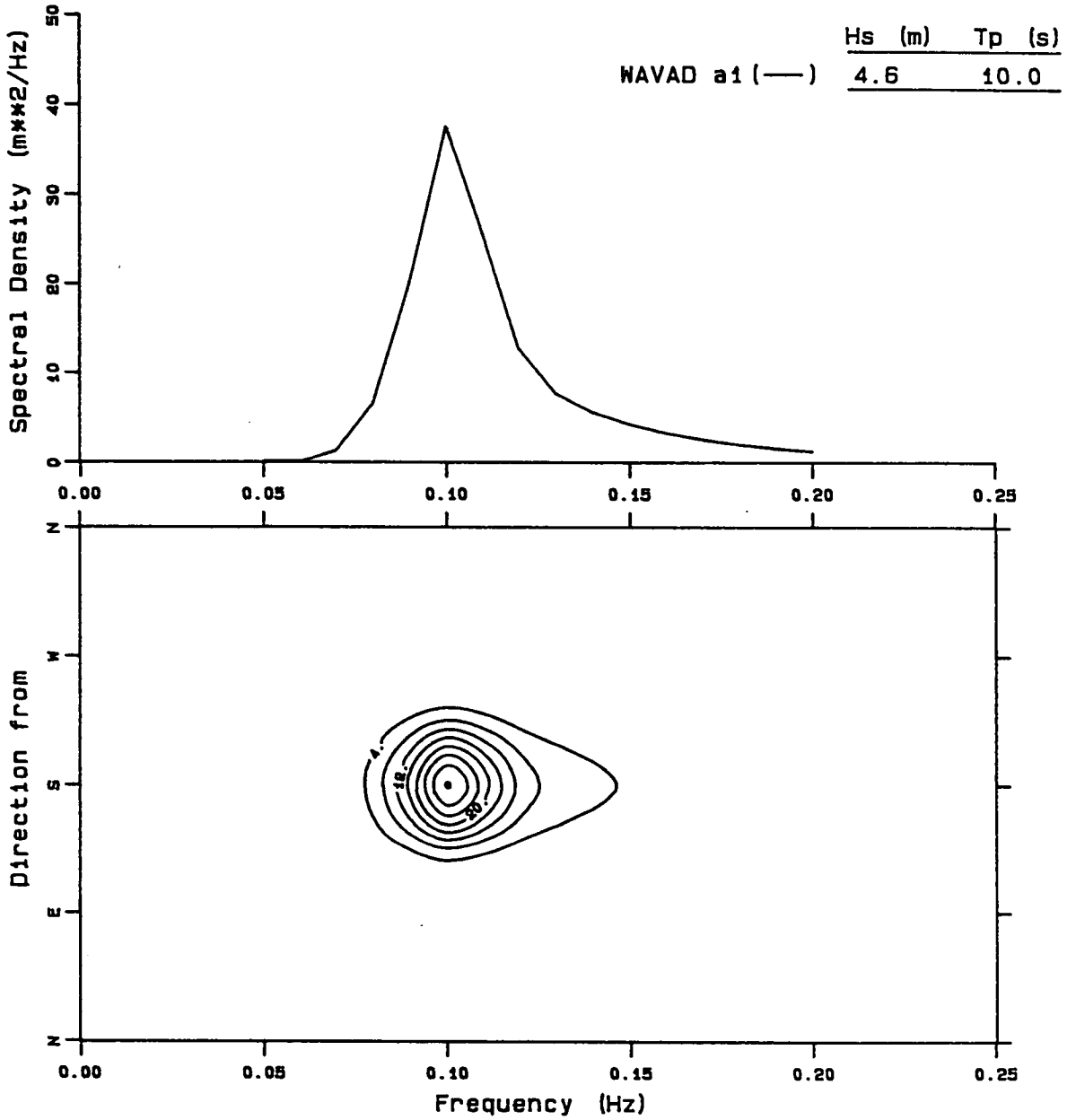
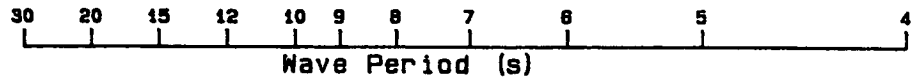


Peak Direction = 180. degrees True  
Contour Interval = 8. m\*\*2/Hz/rad

Fig. 4.22 Continued.

8906181200

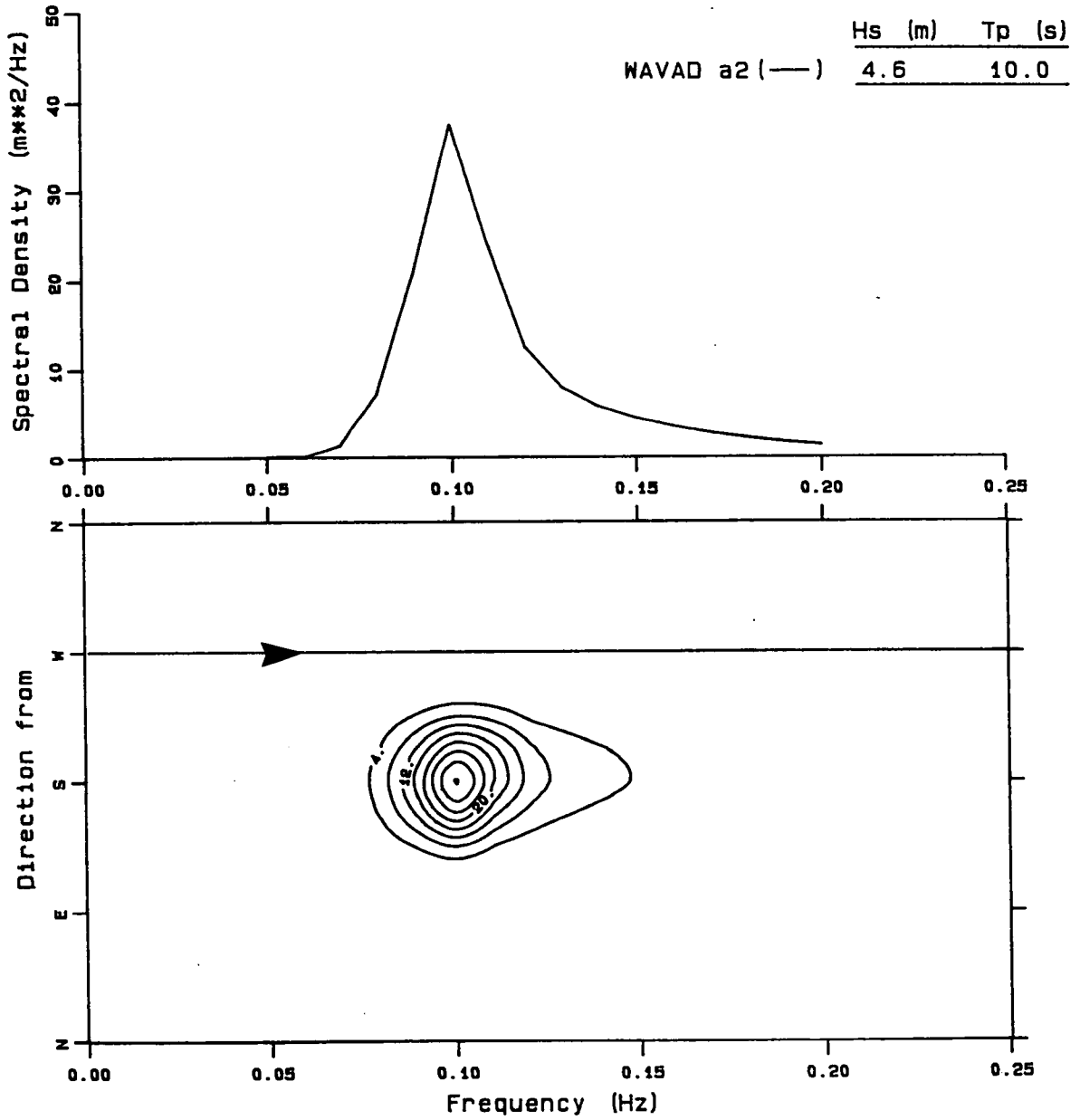
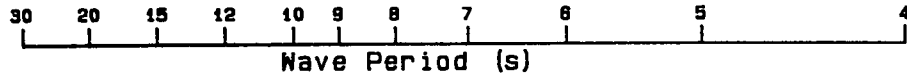
at grid point (31.00, 12.00)



Peak Direction = 180. degrees True  
Contour Interval = 4. m\*\*2/Hz/rad

Fig. 4.23 Spectra computed by WAVAD for various water depths with and without wind (A1 versus A2).

8906181200  
at grid point (31.00, 12.00)



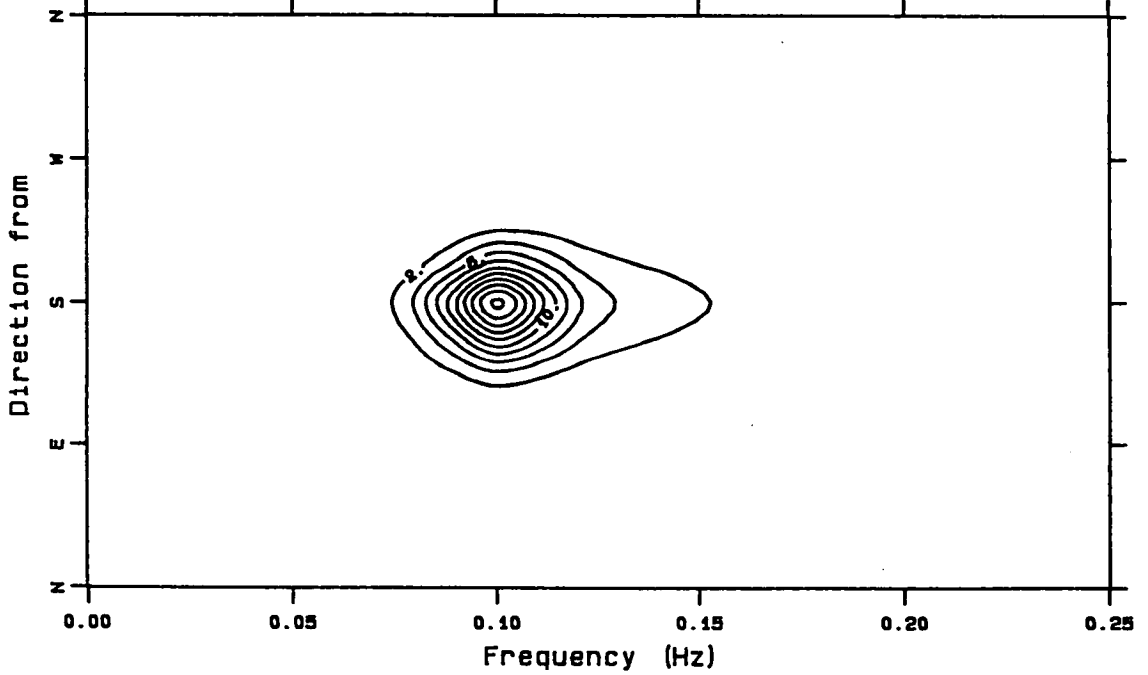
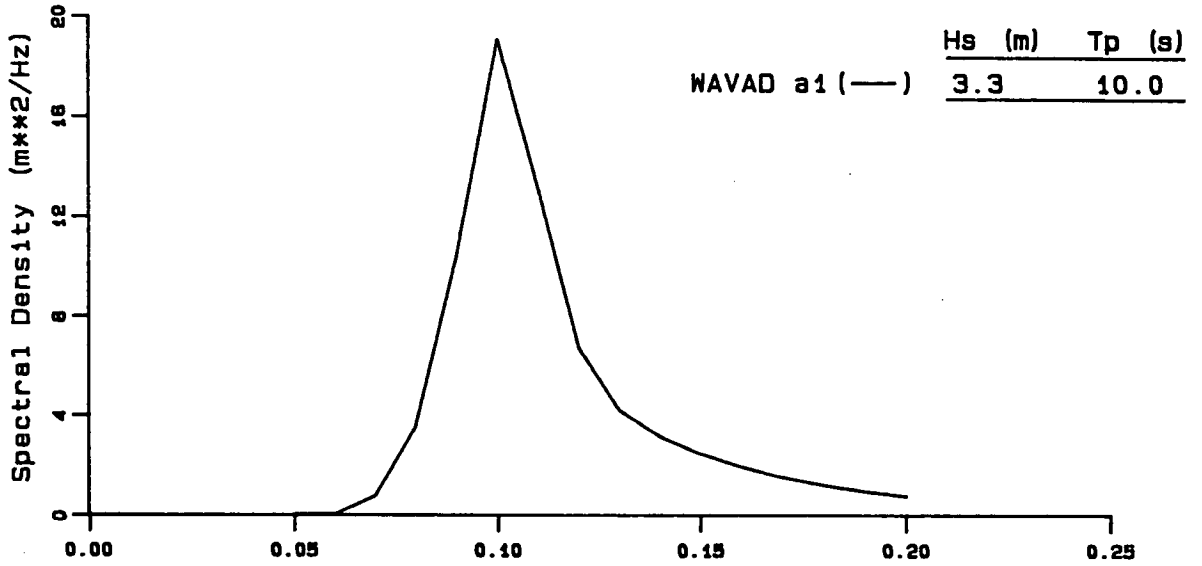
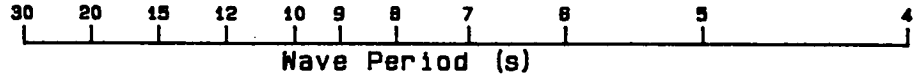
	Hs (m)	Tp (s)
WAVAD a2 (—)	4.6	10.0

Peak Direction = 180. degrees True  
Contour Interval = 4. m\*\*2/Hz/rad

Fig. 4.23 Continued.



8906181200  
at grid point (31.00, 25.00)

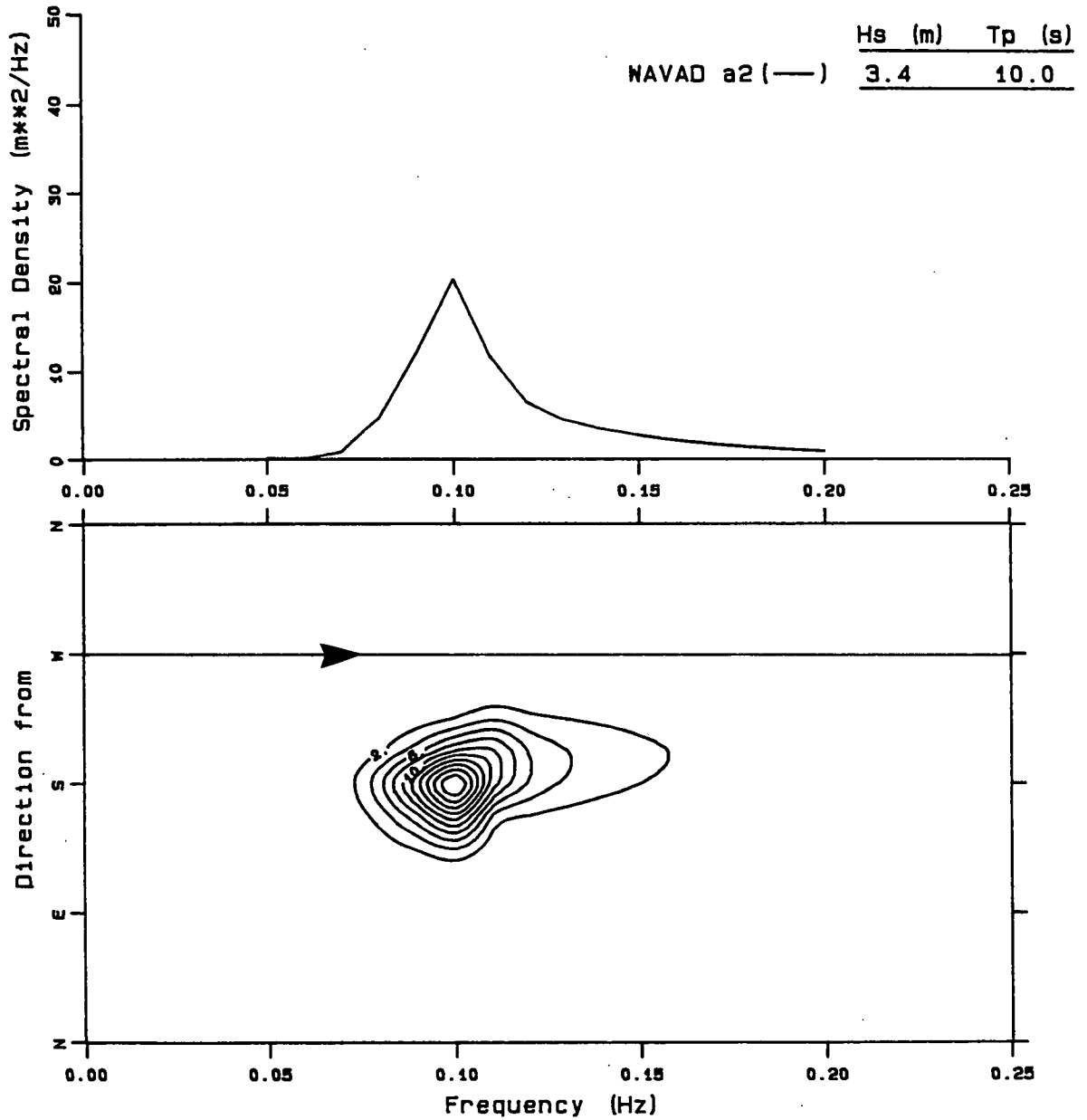
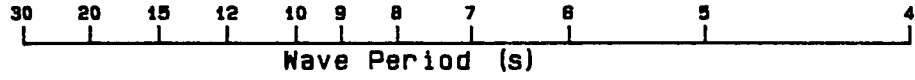


Peak Direction = 180. degrees True  
Contour Interval = 2. m<sup>2</sup>/Hz/rad

Fig. 4.23 Continued.

8906181200

at grid point (31.00, 25.00)

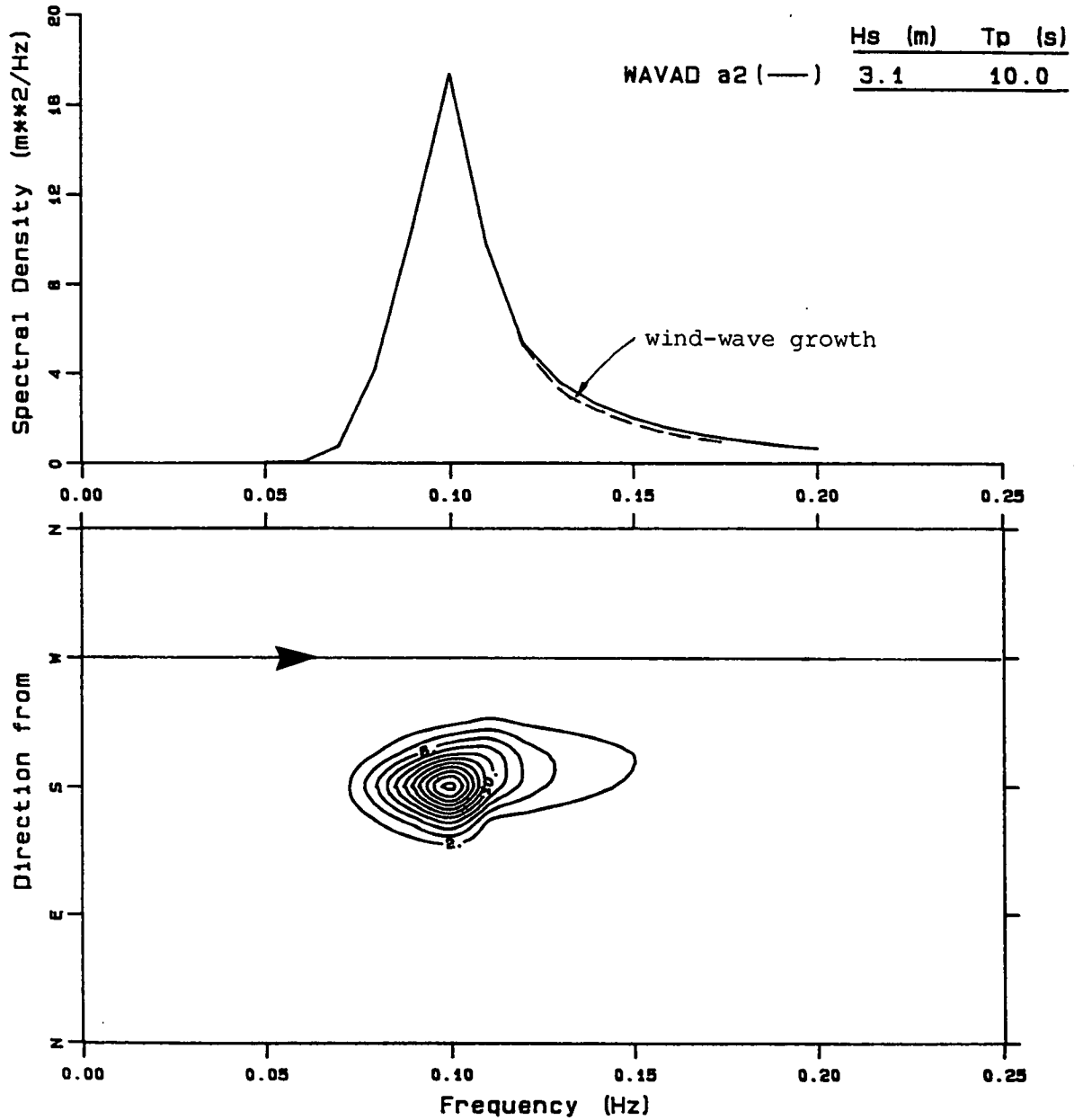
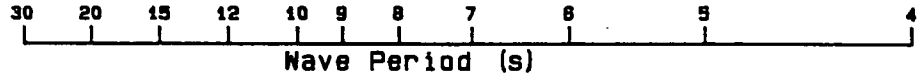


Peak Direction = 180. degrees True  
Contour Interval = 2. m\*\*2/Hz/rad

Fig. 4.23 Continued.

8906181200

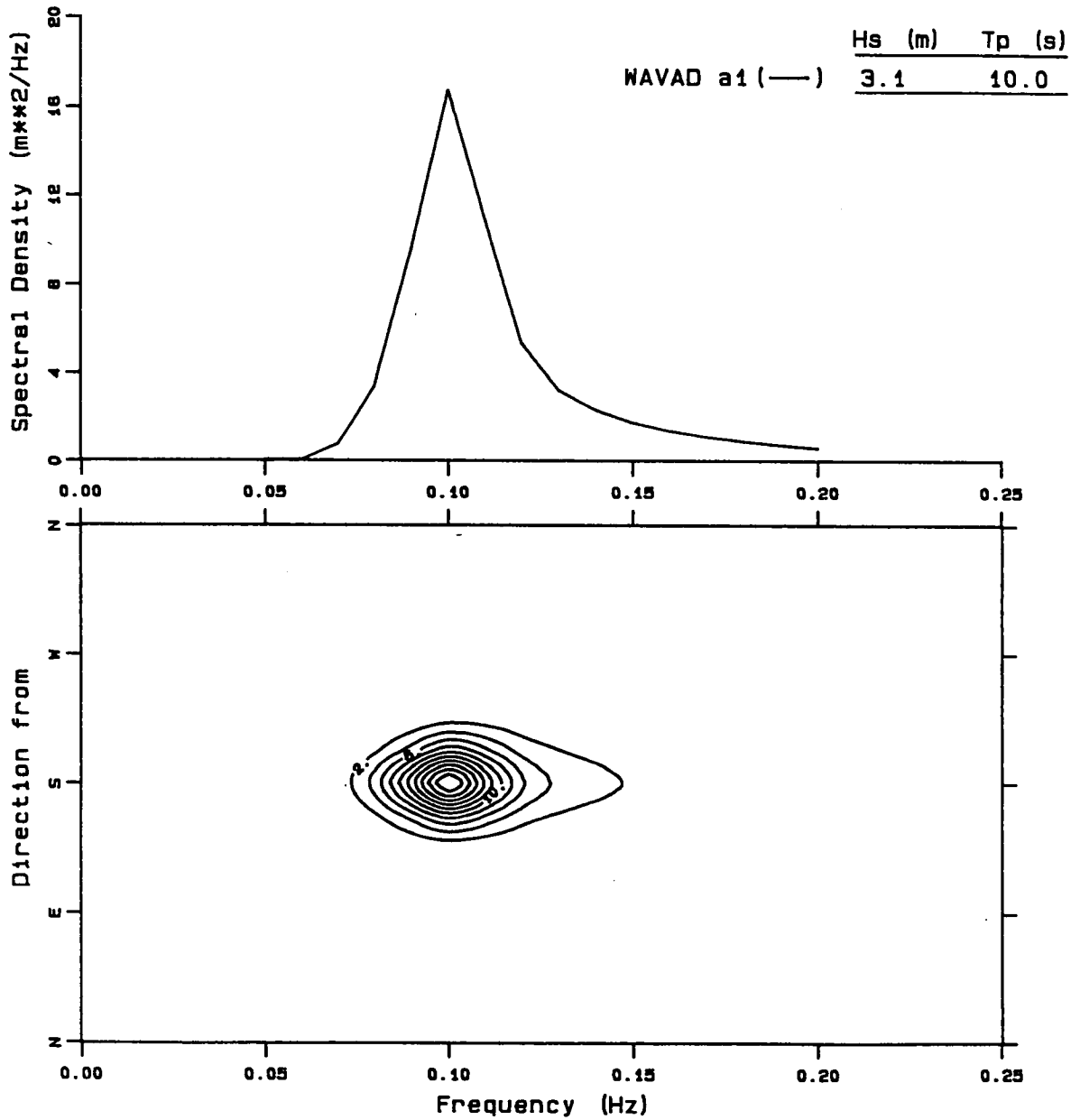
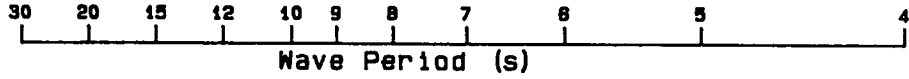
at grid point (31.00, 26.00)



Peak Direction = 180. degrees True  
Contour Interval = 2.  $m^2/Hz/rad$

Fig. 4.23 Continued.

8906181200  
at grid point (31.00, 26.00)



Peak Direction = 180. degrees True  
Contour Interval = 2.  $m^2/Hz/rad$

Fig. 4.23 Continued.

spectra are given in Appendix 6 for reference.

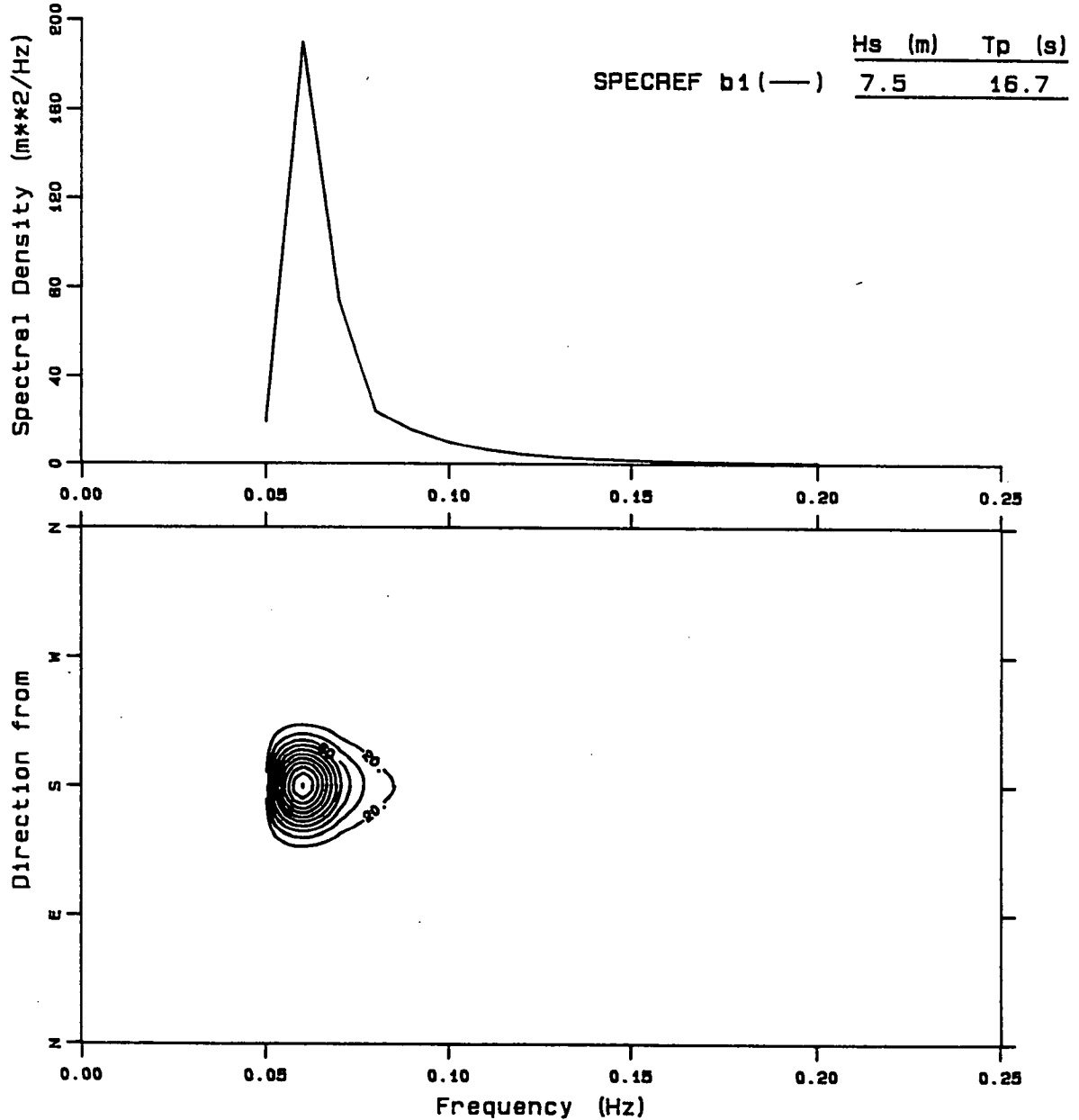
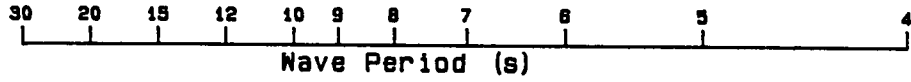
We find that for SPECREF wave growth at frequencies higher than that specified for  $f_p$  of the incident JONSWAP spectrum is evident at all grid points. At a water depth of 100 m (see Fig. 3.5 for a reference map) the wave growth is directly downwind, appearing at frequencies between 0.12 Hz and 0.15 Hz. At a water depth of 70 m (31,12), downwind energy is present, together with energy approximately  $20^\circ$  off the wind direction at intermediate frequencies between those of downwind growth and  $f_p$  of the input spectrum. In 24 m of water (31,25), all wind-wave growth appears from southwesterly directions, concentrated at a frequency of 0.12 Hz as a result of refraction. At this location, and at point (31,26) in 10 m of water, wave rays to the west are refracted into Sable Island. Thus the nearshore bathymetry serves to shelter these locations from waves directly out of the west.

The WAVAD results (Fig. 4.23) differ substantially in that there is little evidence of wind-wave growth over conditions of no wind. At grid point (31,12), for example, there is no downwind growth, in contrast to the result from SPECREF. Downwind growth at these water depths is expected for a wind speed of 20 m/s. At the two shallowest water sites the directional spectrum is modified to a slightly asymmetrical shape with energy at higher frequencies distributed toward the wind direction; however, the effect is not nearly as pronounced as it is in the SPECREF predictions.

Point (31,8) in deep water is compared with (31,25) in 24 m of water for case B in Fig. 4.24 and 4.25. As remarked above, SPECREF exhibits wind-wave growth on the rear face, distinct from the swell energy at lower frequencies. WAVAD results contain much less wave growth than SPECREF, and the energy is distributed over all frequencies at and to the right of  $f_p$ . Thus we see that each model formulation provides a different mechanism to introduce wind-wave energy, consistent with the assumptions stated in Chapter 1. WAVAD's approach means that wind input is coupled to the frequencies greater than or equal to  $f_p$  with the result that its directional distribution is more closely tied to the propagation

8906230000

at grid point (31.00, 8.00)

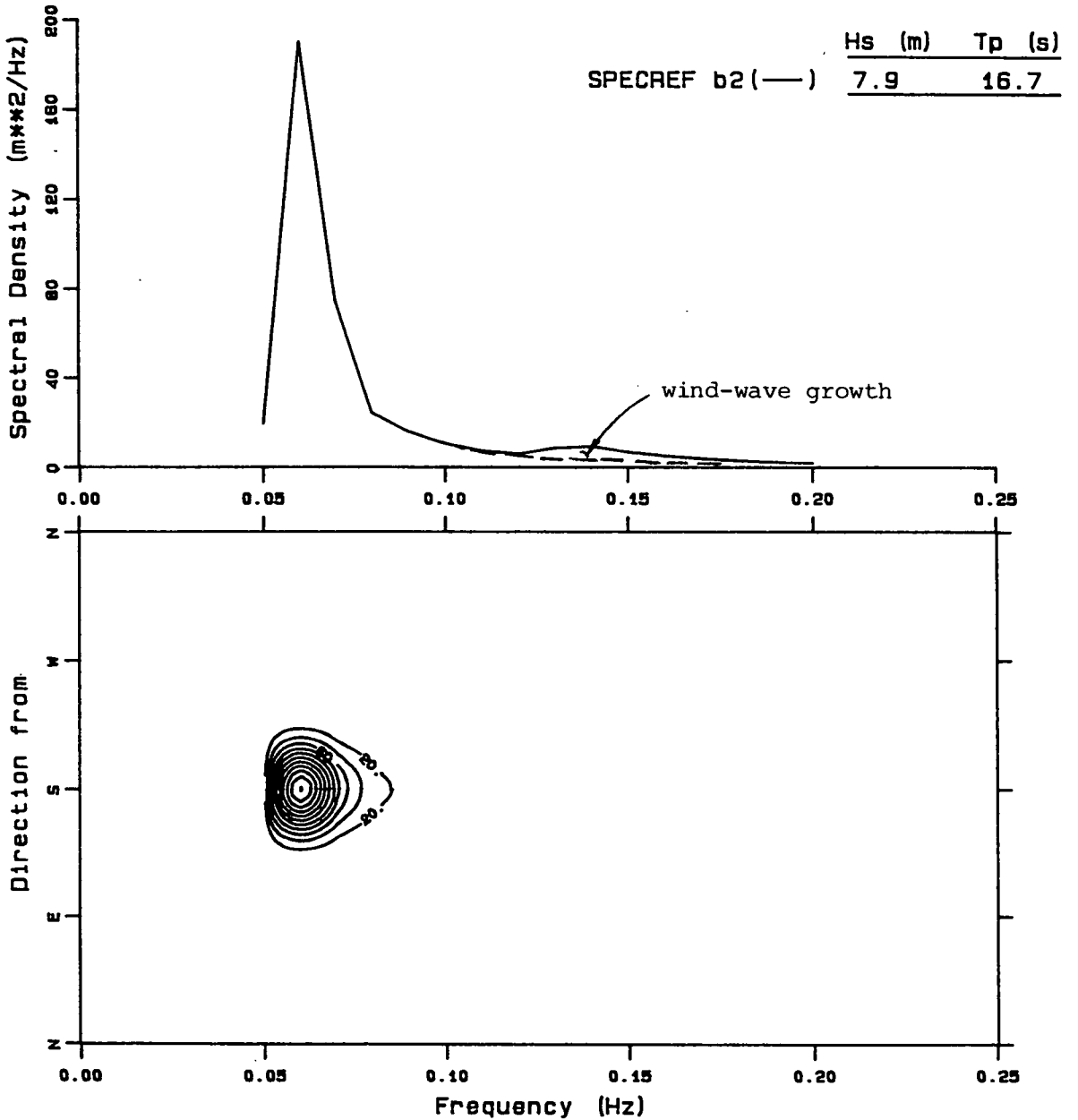
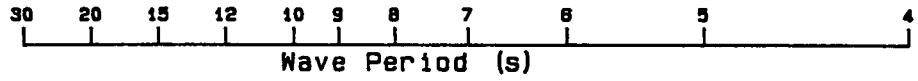


Peak Direction = 180. degrees True  
Contour Interval = 20.  $m^2/Hz/rad$

Fig. 4.24 Spectra computed by SPECREF for various water depths with and without wind (B1 versus B2).

8906230000

at grid point (31.00, 8.00)

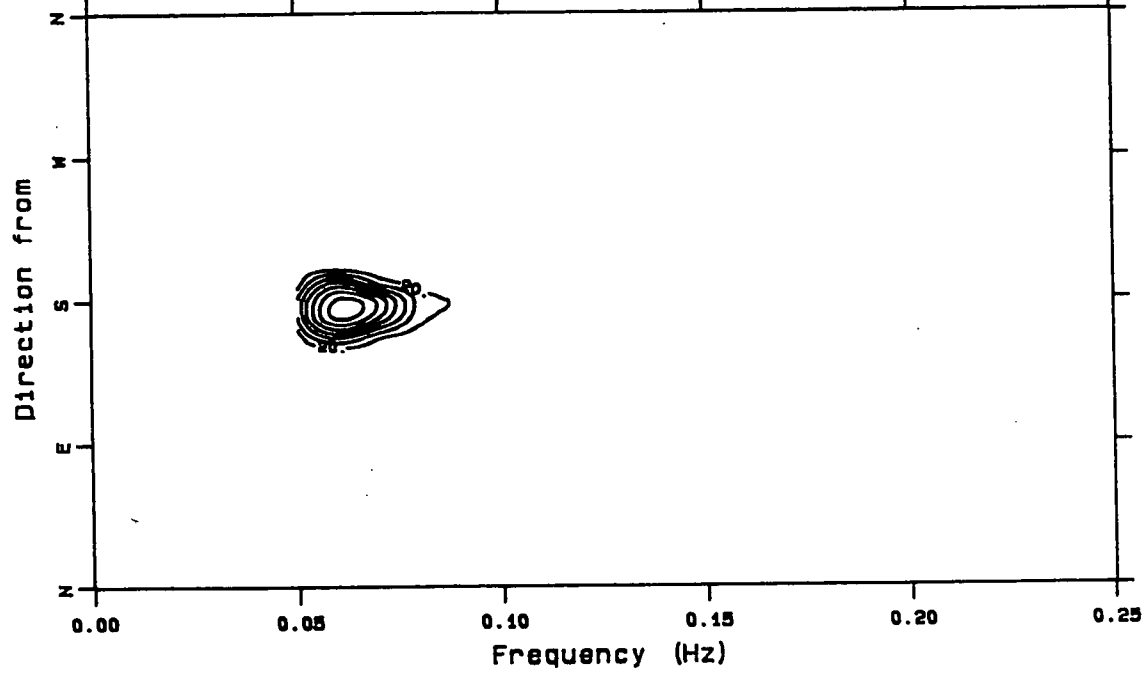
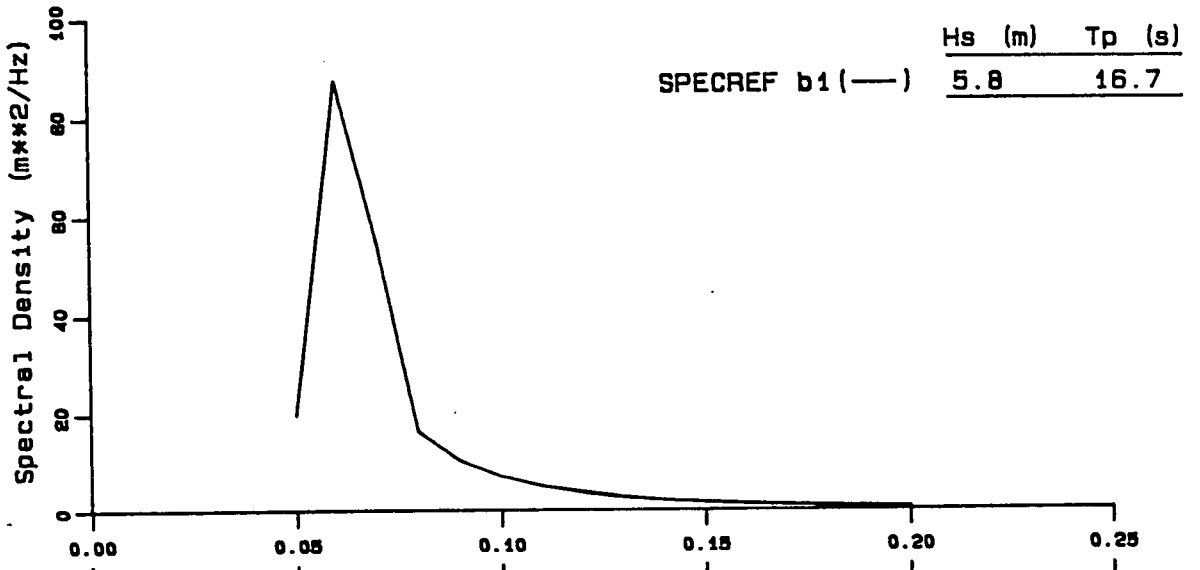
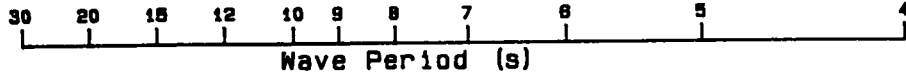


Peak Direction = 180. degrees True  
Contour Interval = 20.  $m^2/Hz/rad$

Fig. 4.24 Continued.

8906230000

at grid point (31.00, 25.00)

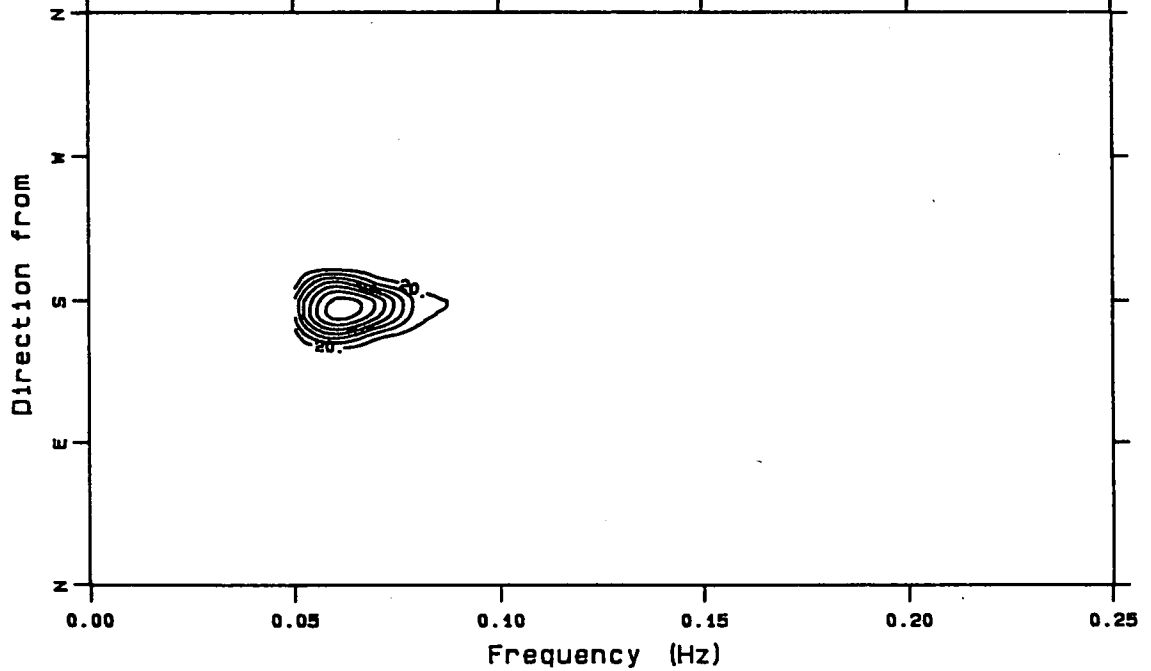
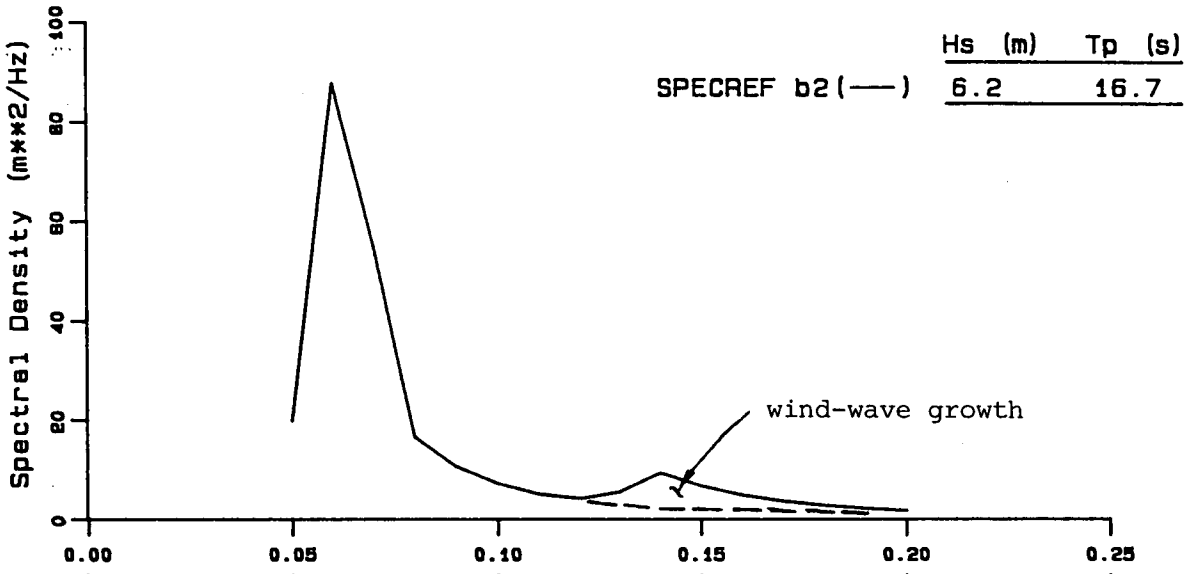
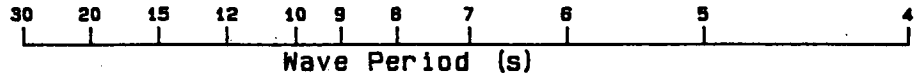


Peak Direction = 180. degrees True  
Contour Interval = 20.  $m^2/Hz/rad$

Fig. 4.24 Continued.



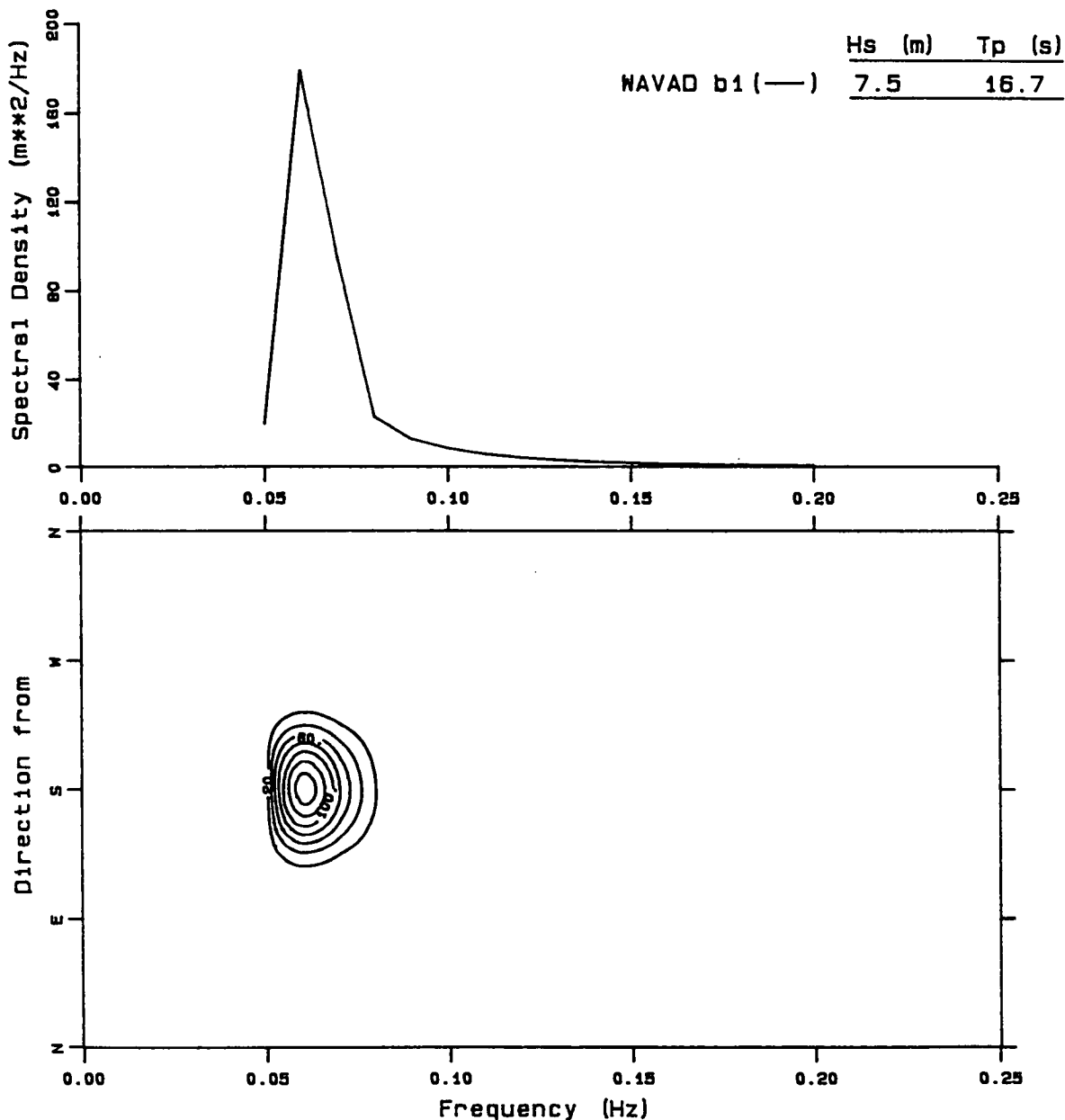
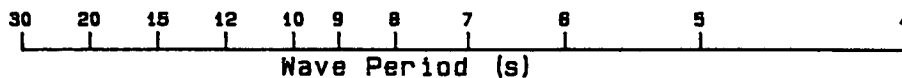
8906230000  
at grid point (31.00, 25.00)



Peak Direction = 180. degrees True  
Contour Interval = 20.  $m^2/Hz/rad$

Fig. 4.24 Continued.

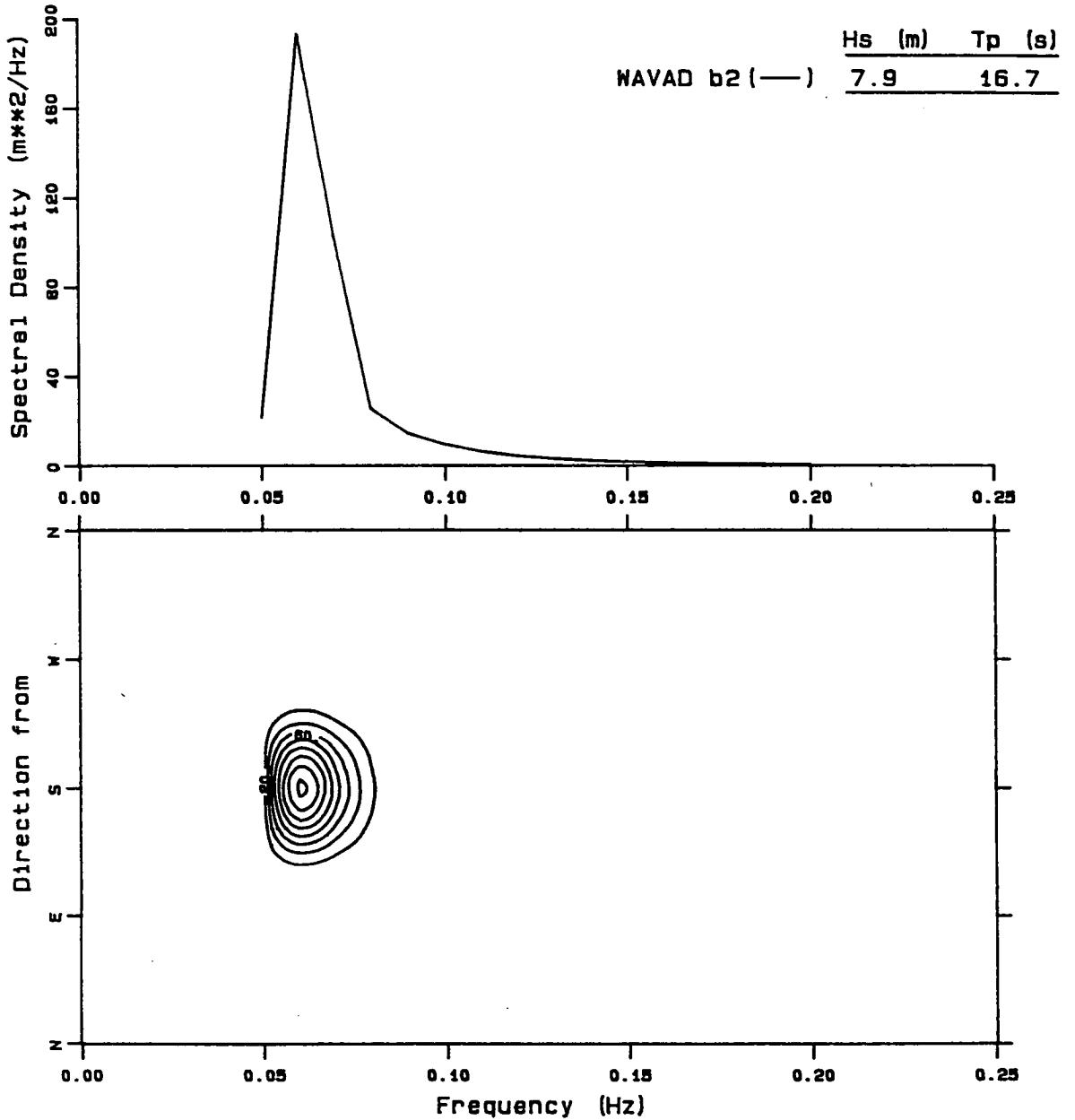
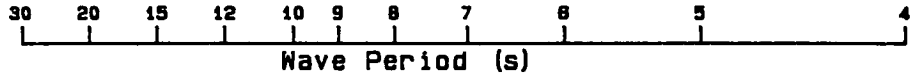
8906181200  
 at grid point (31.00, 8.00)



Peak Direction = 180. degrees True  
 Contour Interval = 20.  $m^2/Hz/rad$

Fig. 4.25 Spectra computed by WAVAD for various water depths with and without wind (B1 versus B2).

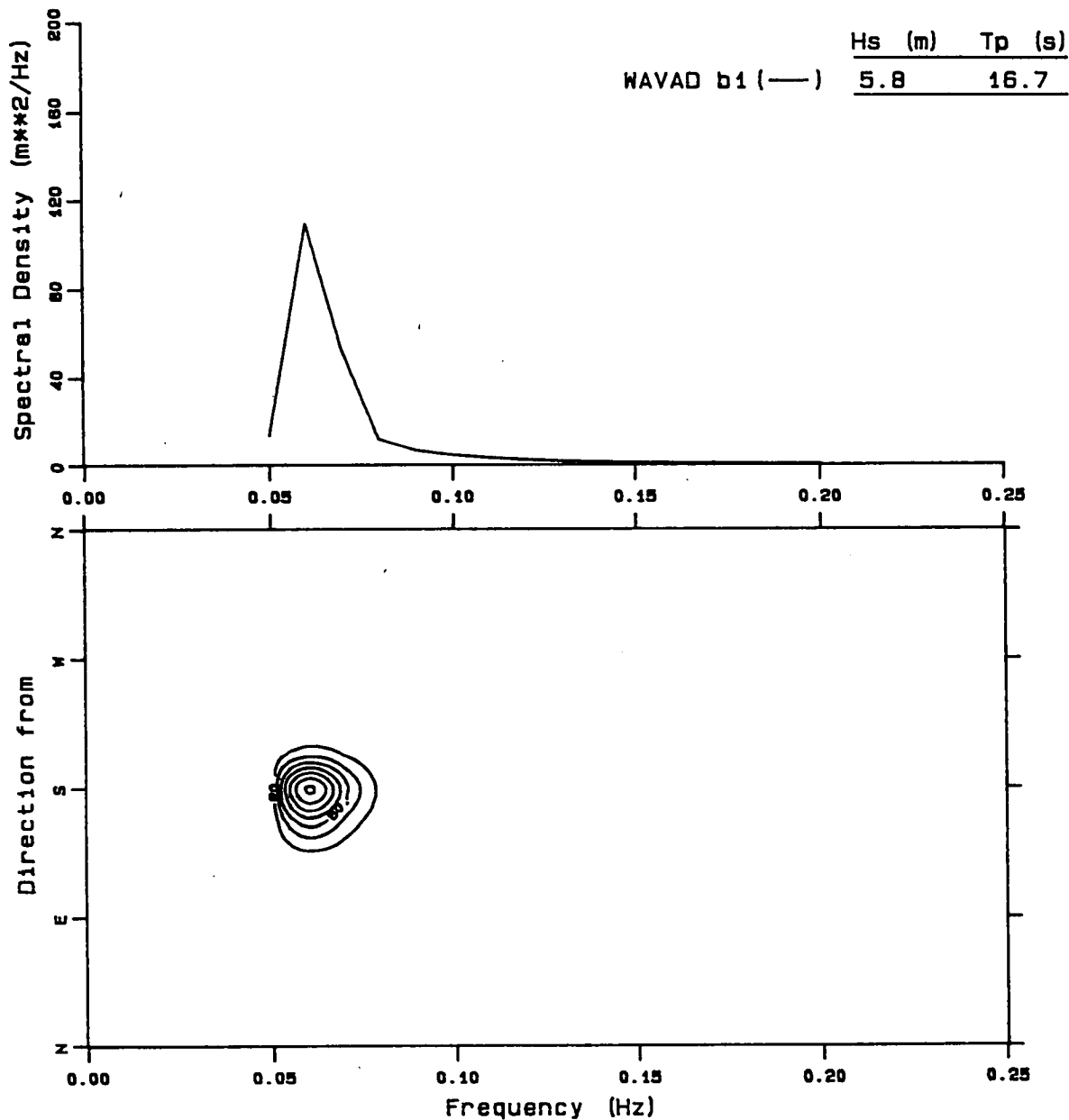
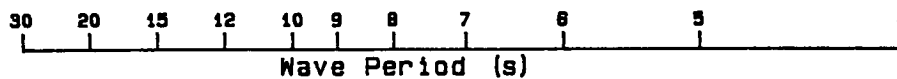
8906181200  
at grid point (31.00, 8.00)



Peak Direction = 180. degrees True  
Contour Interval = 20.  $m^2/Hz/rad$

Fig. 4.25 Continued.

8906181200  
at grid point (31.00, 25.00)

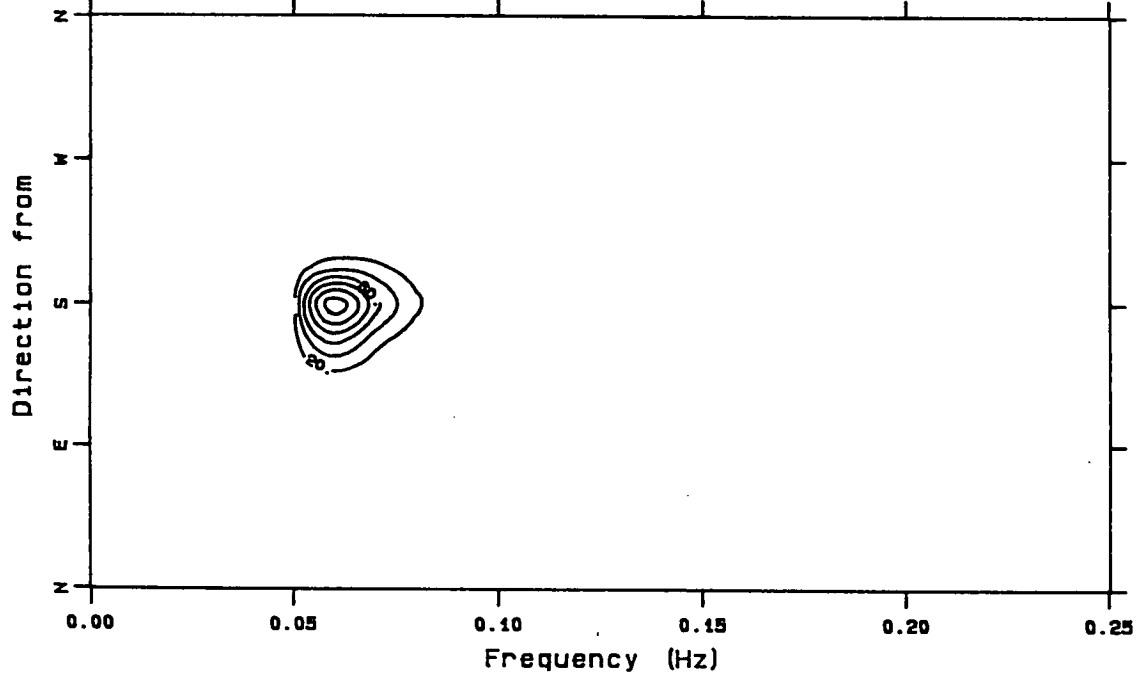
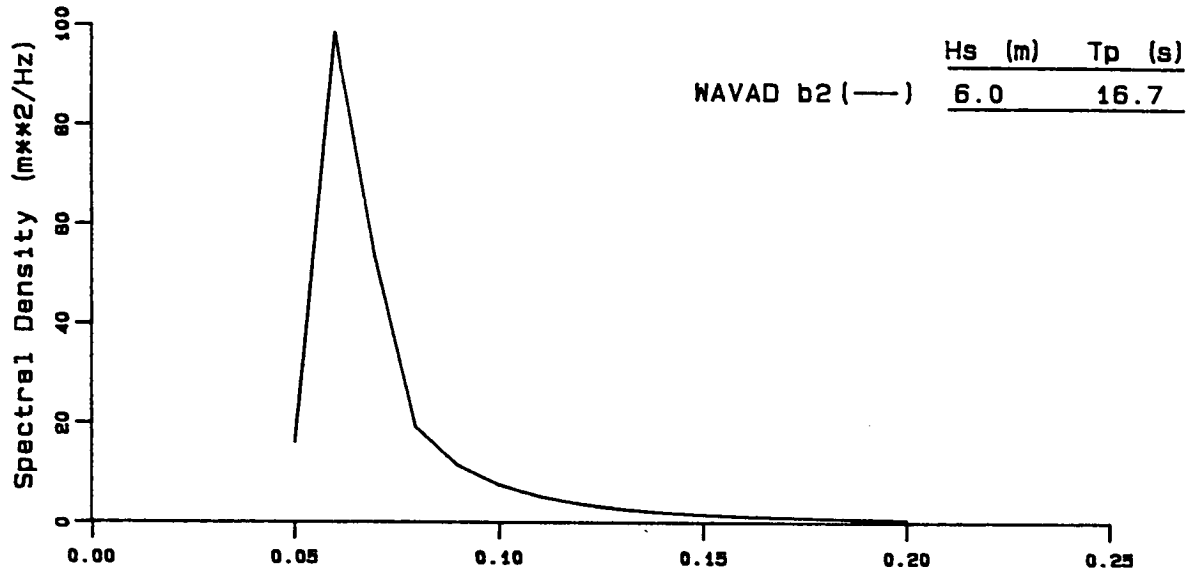
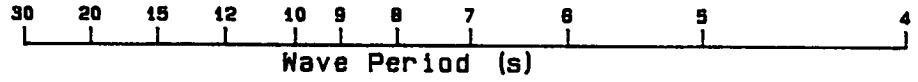


Peak Direction = 180. degrees True  
Contour Interval = 20. m\*\*2/Hz/rad

Fig. 4.25 Continued.

8906181200

at grid point (31.00, 25.00)



Peak Direction = 180. degrees True  
Contour Interval = 20.  $m^2/Hz/rad$

Fig. 4.25 Continued.

direction at these energy frequencies. SPECREF allows for wind energy input to each frequency independently, as a function of the angle between the ray and the wind direction. At high frequencies this method gives wind-wave growth in the downwind direction until refraction alters the propagation direction in shallow water.

The difference in energy for the wind and zero-wind conditions are also evident in Table 4.3 by comparing the  $H_s$  values. These figures show that, for example, in 24 m water depth in both cases A and B that SPECREF produces approximately a 6 to 7% increase in  $H_s$  with the 40 knot westerly wind. WAVAD predicts an increase of about 3%, or just under half that of SPECREF.

These tests show that the differences in formulation for each model, representing a different parameterization of the physical processes, leads to important differences in performance.

## 5.0 CONCLUSIONS AND RECOMMENDATIONS

### 5.1 Spectral Model Performance

#### (a) Expected Accuracies

The accuracy of two spectral wave models, one a decoupled propagation model (SPECREF) and the other a second generation coupled discrete code (WAVAD), has been examined in four storms characterized by strong wind wave growth in shallow water over Sable Island Bank. The starting point was a deep water wave hindcast with WAVAD carried out in a conventional manner using 6-hourly wind fields derived from surface pressure charts and ship observations of wind. These hindcasts provided open sea boundary conditions and the overwater wind for each shallow water calculation.

Time-series comparisons of predicted significant wave height, peak period and wave direction with measured values showed that both models captured the overall storm response in deep water, and correctly predicted energy losses and changes in wave direction into shallow water. One exception was with WAVAD during storm 4 which systematically underestimated measured wave heights and periods. This behaviour contrasted SPECREF which modelled the wave transformation better, producing a more accurate shallow water time-series. This difference between models was investigated further in two idealized tests, which confirmed that the differences in physics as formulated in each model lead to quite different results under some incident wind and wave conditions. It was also clear, however, that errors in the deep water incident wave conditions produced by inaccuracies in the wind fields carried over into the shallow water hindcasts, resulting in large deviations of predicted heights from measured data (up to 20%). These errors occurred at times of rapid wave growth under strong winds that were associated with passage of the storm front (e.g. late on January 5, 1985). Such variations in wind speed are smoothed out in the 6-hourly wind fields derived from surface weather charts.

Error statistics were calculated from each time-series of predicted and measured wave parameters. The results and the conclusions for shallow

water may be summarized as follows:

- (1) SPECREF exhibited an RMS error of 1.1 m in  $H_s$  over the four storms, slightly lower than WAVAD with an RMS error of 1.2 m. In general SPECREF gave a more consistent prediction of the deep-to-shallow water transformation in height (or total energy) than WAVAD. The scatter indices for the two models were 17% (SPECREF) and 18% (WAVAD). These RMS errors and scatter indices are very similar to those published for GSOWM by Clancey et al. (1986) and are typical of operational wave models forced with synoptic wind fields. There is no doubt that better model accuracies would obtain for wind fields carefully constructed to include frontal effects and strong wind zones.
- (2) SPECREF was found to be essentially unbiased for peak period  $T_p$ , with one standard deviation of 0.013 Hz ( $1.3\Delta f$ ). WAVAD, on the other hand, was found to be biased low by about 0.016 Hz ( $1.6\Delta f$ ) with a standard deviation of 0.022 Hz ( $2.2\Delta f$ ).
- (3) SPECREF exhibited a small bias in wave direction (about  $6^\circ$ ) with a standard deviation of about  $16^\circ$ . WAVAD was found to have a bias of approximately  $17^\circ$  with a standard deviation of  $22^\circ$ . However, these error statistics contain the influence of differences between modelled and measured directions at times when the models are known to be inaccurate due to sheltering of northwest waves by Sable Island. During intervals when waves were incident onto Sable Island from the SE and SW quadrants, for which this experiment was designed, directional errors from both models ranged from  $5^\circ$  to  $10^\circ$ . Both models, moreover, correctly predicted the shift in direction from the site in 22 m of water into the shallow 12 m site. Thus it is concluded that the incorporation of refraction into the energy balance is largely correct in both models.
- (4) Predicted and measured spectral shapes were compared qualitatively for both models. SPECREF provided a reasonable model for the shape of the front and rear faces of the spectrum, largely because  $f_p$  was in close agreement with measured peak frequencies and the



saturation law appears to be valid. An exception was found in storm 4 (steady winds and waves) where the low-frequency energy on the forward face was unrealistically high. The cause of this energy distribution for this particular storm is not understood. The decoupled formulation in SPECREF also produces nearly discontinuous jumps in direction at frequencies above  $f_p$  under conditions of turning winds and incident waves. WAVAD spectra exhibited a poorer fit to measured spectra due principally to the tendency to overestimate  $f_p$ , but did not show the jumps in direction with increasing frequency found in the SPECREF spectra. The smoother directional variation with frequency is consistent with the modelled flux of energy between wave frequencies incorporated into WAVAD. Both models exhibit a narrower spread in energy about  $\bar{\theta}$  than measured. (It should be kept in mind that the spread of energy derived here from the measured spectra is based on the a priori cosine power model (Eq. 2.2) which may or may not be correct for the field data.)

- (5) Sensitivity tests have shown that the wind source term is important to the energy balance in the shallow water transformation. On the other hand, bottom friction appears to be of secondary importance. This finding suggests that for the seabed slopes and the sand size range of sediments off Sable Island, dissipation results primarily from whitecapping and wave breaking, at least in depths exceeding about 10 m. Both models incorporate this dissipation through depth dependent saturation laws for  $f > f_p$ . These laws appear sufficient for the cases hindcast in this study.

(b) Strengths and Weaknesses of WAVAD and SPECREF

The principal strength of WAVAD lies in the coupled formulation that provides a model for nonlinear energy fluxes in the spectral balance. This manifests itself as a smooth directional variation over the rear face of the spectrum, giving better qualitative agreement with measured spectra than the decoupled algorithm. The major weakness identified in this study was in the modelling of  $f_p$  during transformation into shallow

water; because it was often overestimated, the detailed energy distribution was not well-modelled and refraction may have been slightly underestimated.

The advantage of the SPECREF formulation lies essentially in its economy to accurately compute  $H_s$ ,  $T_p$  and  $\bar{\theta}$  at one or a few target points in shallow water (WAVAD computes the complete spectrum field at all water grid points and for this reason requires considerably more computer time to run). This economy is achieved in part through the decoupled formulation that allows each frequency to be computed independently of all others, and the program design based on a discrete target point rather than a full field solution. The disadvantage to the decoupled formulation is that directional spectra for rapidly turning winds exhibit unrealistic jumps in direction at higher frequencies. Moreover, it is known that the energy balance within the spectrum is not strictly correct, but is being compensated for, in part, through a saturation law.

## 5.2 Areas of Model Improvement

SPECREF, being a decoupled code, is fully developed with the exception of adding in currents. To incorporate the nonlinear wave-wave interaction fluxes would take the model to the level of WAVAD (second generation) or to a third generation code (e.g. Komen, 1986). The philosophy of such a model would require recoding of SPECREF completely, eliminating its present economy. Nevertheless, although it treats the energy balance more approximately than the models that do attempt to estimate the nonlinear fluxes, we find that SPECREF achieves equivalent or superior accuracy for most of the key spectral properties (total energy, peak frequency, direction and one-dimensional shape). Thus the major area for improvement lies in developing a procedure to smooth the directional variations at higher frequencies.

The main area of improvement in WAVAD concerns the treatment of  $f_p$  as a prognostic variable. In the present shallow water applications,  $f_p$  has been fixed over the domain at each time step using the deep water values of  $f_p$  along the open sea boundaries. Thus it is not truly a prognostic

variable in shallow water since it cannot change in response to redistributions of energy within the spectrum as it transforms. Extension of the theory to allow  $f_p$  to respond appears warranted to achieve better accuracy.

### **5.3 Implications for Oil and Gas Developments**

The principal conclusion from this study is that available modelling techniques are suitable for predicting shallow water wave transformations using hindcasting methods. We have shown that even the simpler, more economical procedure contained in SPECREF may be expected to provide estimates of significant wave heights, peak periods, and directions to within the normal errors associated with heave-pitch-roll buoy measurements (e.g. typically within 10 to 12% for  $H_s$ ). The theoretically more advanced WAVAD model achieves similar accuracy although in the cases studied here, it proved to be slightly less accurate than SPECREF.

We have also found, however, that differences in model formulation produce large variations in model performance. These variations were detected primarily for steady winds and incident wave directions. Consequently, the use of models such as those compared in this study for design wave hindcasts will require further validation with measurements to establish confidence in the results.

It is also apparent that further development of modelling techniques is warranted. Such development is required to reduce prediction errors in certain wind-wave conditions, and to confirm that the parameterization of the physical processes governing shallow water transformation incorporated into the models remains valid across the range of wave and bathymetric conditions encountered in nature.

The accuracy of either model depends critically on the deep water boundary conditions, which in turn depend on how well the wind fields capture the storm features in nature. It is emphasized that the model performance achieved here is representative of a full hindcast based on storm wind fields over a substantial portion of the Atlantic Ocean.

This is the normal approach taken to estimate extreme wave conditions using a set of severe storms. Deep water wave measurements were not used for the incident wave conditions in this study. If they had been, then the wave model results would undoubtedly have been in closer agreement with the shallow water measurements.

Three shallow water transformation processes were important in the energy balance:

- refraction and shoaling (propagation algorithm),
- wind input (energy source term), and
- dissipation through wave breaking (energy sink term).

Significantly, some type of wave-seabed interaction term (bottom friction) was found to be negligible for the sand sized-sediments on Sable Island Bank. This result is consistent with Resio's (1987) theory on the role of nonlinear fluxes in determining the energy balance in finite depth water. It is not clear, however, that this conclusion is universally valid. In fact it seems most likely that it would not hold in areas like the Beaufort Sea where the seabed is composed of soft muds and silts. There the potential for energy loss to the seabed through a poroelastic response certainly exists. This mechanism would make wave transformation modelling much more difficult and would introduce yet one more free parameter into the modelling process.

#### **5.4 Recommendations**

Bottom friction has been shown to be unimportant to wave modelling on Sable Island Bank. This is unlikely to hold in the Beaufort Sea because of the differences in bottom sediments and the very low beach slopes. In August and September 1986 a carefully controlled shallow water directional wave dataset was collected in the Beaufort Sea. Two sites were occupied, in 6 and 10 metres of water, separated by 13,200 m along a transect to the northwest of North Head. Two storms were monitored that generated waves directly down the transect containing the two gauges. Detailed geotechnical and sedimentary data are also available for the area. The experiment and the data are described by Hodgins et

al. (1986).

A study similar to that carried out here is recommended using the new directional wave dataset. The purpose would be to determine if either modelling approach (decoupled propagation or coupled discrete formulations) is seriously in error for the sediments found on the Mackenzie Delta, and to determine what additional processes are necessary in the spectral energy balance. Such a study would give a more complete appraisal of available shallow water wave models, in two dissimilar sedimentological regimes, but each of which is important in terms of offshore hydrocarbon development.

## REFERENCES

- Abernethy, C.L. and G. Gilbert, 1975. Refraction of Wave Spectra. Rep. No. INT 117, Hydraulics Research Station, Wallingford, U.K.
- Amos, C.L. and E.L. King, 1984. Bedforms of the Canadian Eastern Seaboard: A Comparison with Global Occurrences. Marine Geology, 57, 167-208.
- Bouws, E., J. Ephraums, J. Ewing, P. Francis, H. Guenther, P. Janssen, G. Komen, W. Rosenthal, W. de Voogt, 1985. Shallow Water Intercomparison of Wave Models Parts I, II, III, in The Ocean Surface: Wave Breaking, Turbulent Mixing and Radio Probing (Ed. Y. Toba and H. Mitsuyasu). Reidel Publishing Company, Dordrecht, 201-220.
- Cavaleri, L. and P.M. Rizzoli, 1981. Wind Wave Prediction in Shallow Water: Theory and Applications. J. Geophys. Res., 86, 10961-10973.
- Clancy, R.M., J.E. Kaitala, and L.F. Zambresky, 1986. The Fleet Numerical Oceanography Center Global Spectral Ocean Wave Model. Bull. Am. Meteor. Soc., 67(5), 498-512.
- Collins, J.I., 1972. Prediction of Shallow-Water Spectra. J. Geophys. Res., 77, 2693-2707.
- Donelan, M.A., J. Hamilton and W.H. Hui, 1985. Directional Spectra of Wind-Generated Waves. Phil. Trans. R. Soc. Lond. A, 15, 509-562.
- Dorrestein, R., 1960. Simplified Method for Determining Refraction Coefficients for Sea Waves. J. Geophys. Res., 65, 637-642.
- Dreyer, A.A., 1973. Study of Wind-Generated Seawaves in Shallow Sea. Thesis, Inst. Oceanology, Acad. Sci. USSR.
- Forristall, G.Z., 1981. Measurements of a Saturated Range in Ocean Wave Spectra. J. Geophys. Res., 86, 8075-8094.
- Grosskopf, W.G. and C.L. Vincent, 1982. Energy Losses of Waves in Shallow Water. C.E.R.C., Coastal Engng. Tech. Aid No. 82-2.
- Hasselmann, D.E., M. Dunckel and J.A. Ewing, 1980. Directional Wave Spectra Observed During JONSWAP 1973. J. Phys. Oceanogr., 10(8), 1264-1280.
- Hodgins, D.O. and C.T. Niwinski, 1987. Prediction of Directional Wave Spectra at Coastal Locations. Proc. Coastal & Port Engng. in Developing Countries, Vol. II, 2006-2020.
- Hodgins, D.O., G. Drapeau and L.H. King, 1986. Field Measurements of Sediment Transport on the Scotian Shelf, Volume I: The Radio-Isotope Experiment. Environmental Studies Revolving Funds Report No. 041, Ottawa.

- Hodgins, D.O., O.J. Sayao, E.D. Kinsella and P.W. Morgan, 1986. Nearshore Sediment Dynamics - Beaufort Sea. Environmental Studies Revolving Funds Report No. 054, Ottawa.
- Hsiao, S.V. and O.H. Shemdin, 1978. Bottom Dissipation in Finite-Depth Water Waves. Proc. 16th Internat. Conf. on Coastal Engng.
- Janssen, P.A.E.M., G.J. Komen and W.J.P. de Voogt, 1984. An Operational Coupled Hybrid Wave Prediction Model. J. Geophys. Res., 89(C3), 3635-3654.
- Kahma, K.K., 1981. A Study of the Growth of the Wave Spectrum with Fetch. J. Phys. Oceanogr., 11, 1503-1516.
- Karlsson, T., 1969. Refraction of Continuous Ocean Wave Spectra. ASCE J. Waterways, Harbours, Coastal Engng. Div., 95 (WW4), 437-448.
- Kitaigorodskii, S.A., V.P. Krasitskii and M.M. Zaslavskii, 1975. On Phillips' Theory of Equilibrium Range in the Spectra of Wind-Generated Gravity Waves. J. Phys. Oceanogr., 5, 410-420.
- Kitaigorodskii, S.A., 1983. On the Theory of the Equilibrium Range in the Spectrum of Wind-Generated Gravity Waves. J. Phys. Oceanogr., 13(5), 816-827.
- Komen, G.J., 1984. The Wave Modelling (WAM) Project: Proposal for the Development and Operational Implementation of a Third Generation Ocean Wave Model. First draft, unpublished manuscript, De Bilt, The Netherlands.
- Krasitskii, V.P., 1974. Toward a Theory of Transformation of the Spectrum on Refraction of Wind Waves. Izv. Akad. Nauk. SSSR, Atmosph. and Ocean Physics, 10, 72-82.
- LeMehaute, B. and J.D. Wang, 1982. Wave Spectrum Ranges on Sloped Beach. ASCE, J. Waterways, Harbors, Coastal and Ocean Div., 108(WW1), 33-47.
- Long, R.B., 1980. The Statistical Evaluation of Directional Spectrum Estimates Derived from Pitch/Roll Buoy Data. J. Phys. Oceanogr., 10, 944-952.
- Longuet-Higgins, M.S., 1956. The Refraction of Sea Waves in Shallow Water. J. Fluid Mech., 1, 163-176.
- Longuet-Higgins, M.S., 1957. On the Transformation of a Continuous Spectrum by Refraction. Proc. Camb. Phil. Soc., 53, 226-229.
- Longuet-Higgins, M.S., and R.W. Stewart, 1960. Changes in the Form of Short Gravity Waves on Long Waves and Tidal Currents. J. Fluid Mech., 8, 565-583.

- Munk, W.H. and R.S. Arthur, 1952. Wave Intensity Along a Refracted Ray. Natl. Bur. Stand. Circ. No. 521, 95-108.
- Phillips, O.M., 1977. Dynamics of the Upper Ocean. 2nd Ed. Cambridge U. Press, London.
- Resio, D.T., 1982. Wave Prediction in Shallow Water. Proc. 14th Annual Offshore Tech. Conf., OTC 4242, Vol. 2, 147-152.
- Resio, D.T., 1987. Shallow-Water Waves. I: Theory. ASCE J. Waterway, Port, Coastal and Ocean Engineering, 113(3), 264-281.
- Resio, D.T., 1988. Shallow Water Waves. II: Data Comparisons. ASCE J. Waterway, Port, Coastal and Ocean Engineering, 114(1), 50-65.
- Shemdin, O.H., K. Hasselmann, S.V. Hsiao and K. Heterich, 1977. Nonlinear and Linear Bottom Interaction Effects in Shallow Water, in Turbulent Fluxes Through the Sea Surface, Wave Dynamics and Prediction. (Ed. A. Favre and K. Hasselmann). Plenum Press, N.Y., 347-437.
- Shemdin, O.H., S.V. Hsiao, H.E. Carlson, K. Hasselmann and K. Schulze, 1980. Mechanisms of Wave Transformation in Finite-Depth Water. J. Geophys. Res., 85(C9), 5012-5018.
- Shiau, J.C. and H. Wang, 1977. Wave-Energy Transformation Over Irregular Bottom. ASCE J. Waterways, Ports, Coastal and Ocean Div., 103 (WW1), 57-63.
- SWAMP Group, 1985. Ocean Wave Modeling. Plenum, New York.
- Thornton, E.B., 1977. Rederivation of the Saturation Range in the Frequency Spectrum of Wind-Generated Waves. J. Phys. Oceanogr., 7, 137-140.
- Wang, H. and W.-C. Yang, 1981. Wave Spectral Transformation Measurements at Sylt, North Sea. Coastal Engng., 5, 1-34.
- Yanenko, N.N., 1971. The Method of Fractional Steps. Springer.